WAFER-SCALE PROCESSING OF ARRAYS OF NANOPORE DEVICES

A Dissertation
Presented to
The Academic Faculty

by

Amir Ahmadi

In Partial Fulfillment
of the Requirements for the Degree
Doctorate of Philosophy in the
School of Chemical & Biomolecular Engineering

Georgia Institute of Technology
May 2013

WAFER-SCALE PROCESSING OF ARRAYS OF NANOPORE DEVICES

Approved by:

Dr. Sankar Nair, Advisor
School of Chemical & Biomolecular Engineering
Georgia Institute of Technology

Dr. Edward M. Balog
School of Applied Physiology
Georgia Institute of Technology

Dr. Paul A. Kohl
School of Chemical & Biomolecular Engineering
Georgia Institute of Technology

Dr. Peter J. Hesketh
School of Mechanical Engineering
Georgia Institute of Technology

Dr. Clifford L. Henderson
School of Chemical & Biomolecular Engineering
Georgia Institute of Technology

Date Approved: January 9, 2013

ACKNOWLEDGEMENTS

I wish to thank my advisor, Professor Sankar Nair, and my thesis committee members Professors Ed Balog, Cliff Henderson, Peter Hesketh, and Paul Kohl. I want to make special acknowledgements to Devin Brown for his help with electron beam lithography and Gerald Lopez at GenISys for assistance in simulating electron scattering behavior. I would also like to thank Gary Spinner, Joel Pikarsky, and the entire MiRC staff for their hard work maintaining the facilities and helping with process issues. Finally, I would like to thank former Nair group members Dr. Suchitra Konduri, Dr. Yeny Hudiono, Dr. Mohamad Kassaee, and Christopher Russell, for their support and friendship.

TABLE OF CONTENTS

LIST OF TABLES

LIST OF FIGURES

Page

SUMMARY

Nanopore-based single-molecule analysis of biomolecules such as DNA and proteins is a subject of strong scientific and technological interest. In recent years, solid state nanopores have been demonstrated to possess a number of advantages over biological (e.g., ion channel protein) pores due to the relative ease of tuning the pore dimensions, pore geometry, and surface chemistry. However, solid state fabrication methods have been limited in their scalability, automation, and reproducibility.

In this work, a wafer-scale fabrication method is first demonstrated for reproducibly fabricating large arrays of solid-state nanopores. The method couples the high-resolution processes of electron beam lithography (EBL) and atomic layer deposition (ALD). Arrays of nanopores (825 per wafer) are successfully fabricated across a series of 4" wafers, with tunable pore sizes from 50 nm to sub-20 nm. The nanopores are fabricated in silicon nitride films with thicknesses varying from 10 nm to 50 nm. ALD of aluminum oxide is used to tune the nanopore size in the above range. By careful optimization of all the processing steps, a device survival rate of 96% is achieved on a wafer with 50 nm silicon nitride films on 60- 80 μm windows. Furthermore, a significant device survival rate of 88% was obtained for 20 nm silicon nitride films on order 100 μm windows. In order to develop a deeper understanding of nanopore fabrication-structure relationships, a modeling study was conducted to examine the physics of EBL, in particular: to investigate the effects of beam blur, dose, shot pattern, and secondary electrons on internal pore structure. Under the operating conditions used in pore production, the pores were expected to taper to a substantially smaller size than their

apparent size in SEM. This finding was supported by preliminary conductance readings from nanopores.

CHAPTER 1

INTRODUCTION AND BACKGROUND

1.1 Nanopores in Biology and Technology

Nanopores are ubiquitous in biology, in the form of ion channels embedded in cell membranes and nuclear membranes. A biological ion channel is formed from one or more proteins self-assembled into a nanoporous channel-like structure, with a nominal pore size of less than 1 nm and length of ~ 20 nm spanning the lipid membrane. Functional ion channels are often characterized by the presence of a 'gate' (that opens and closes in response to an external chemical or electrical stimulus) as well as a 'selectivity filter' that preferentially allows permeation of particular ions (such as sodium, potassium, calcium, or chloride) while excluding others [1]. Ion channels are involved in diverse biological processes such as the transmission of nerve impulses, metabolic pathway regulation (e.g., insulin release from pancreatic β-cells), and muscle (e.g., cardiac) function. Ion channels are thus an important therapeutic target in the case of diseases like diabetes and cystic fibrosis.

The functional characteristics of biological nanopores (high permeation rates and selectivity) are also highly desirable for replication in synthetic systems. Functional nanopores (e.g., those in nanoporous zeolites [2] or nanotubes [3, 4]) are already important in many technological areas including energy-efficient separations, energy conversion, and chemical or biomolecule sensing. In these applications, it is not required to address individual nanopores, and the collective behavior of the nanoporous material or thin film is of main interest. However, nanopores that function as individually addressable devices have recently assumed importance as a platform for 'next-generation' methods for ultra-rapid performance of basic biotechnological operations

such as DNA/RNA sequencing and protein analysis [5]. These operations form the foundation of genomics and proteomics, which hold the promise of ultimately providing a complete understanding of biological systems from a genetic perspective as well as cures for diseases that are influenced by genetic factors [6]. In particular, "engineered nanopore devices" (ENDs) that can analyze the properties of individual DNA or protein strands, offer a promising route towards applications such as ultra-rapid DNA sequencing. In this chapter we discuss the current knowledge of several aspects of END science and technology. We also provide a perspective regarding future developments that have potential to create technological applications of these devices, and the corresponding scientific and engineering challenges that must be overcome.

1.2 Nanopores from Soft Matter

The first synthetic ENDs were produced from 'soft matter' embodied by channel-forming bacterial proteins reconstituted in synthetic lipid bilayers. The general principle behind ENDs is as follows: the analyte (e.g., DNA) is dissolved in a conductive salt solution and driven through the nanopore with an applied electric field. Sensing is accomplished in several possible ways, the most popular being the measurement of modulations in ionic current through the nanopore during transport (translocation) of the analyte. The duration and degree of these modulations can be correlated with parameters such as the biomolecule length, and (in principle) its sequence. One prevailing example is the protein α-hemolysin (α -HL), which is a naturally occurring compound secreted by the bacterium *Staphylococcus aureus*. When exposed to a synthetically prepared lipid bilayer, each α -HL molecule acts as a monomer in a self assembly process at the surface of the lipid substrate. Seven such monomers fold into a unique quaternary structure that forms a nanoporous transmembrane channel (Figure 1.1). The nanopore opening is ~ 2.6 nm (on the left), leading into a wider vestibule which then narrows to a limiting diameter of 1.5 nm followed by an elongated cylindrical channel embedded in the lipid membrane.

As discussed later, biomolecule translocation has been found to be affected by both the channel and vestibular regions.

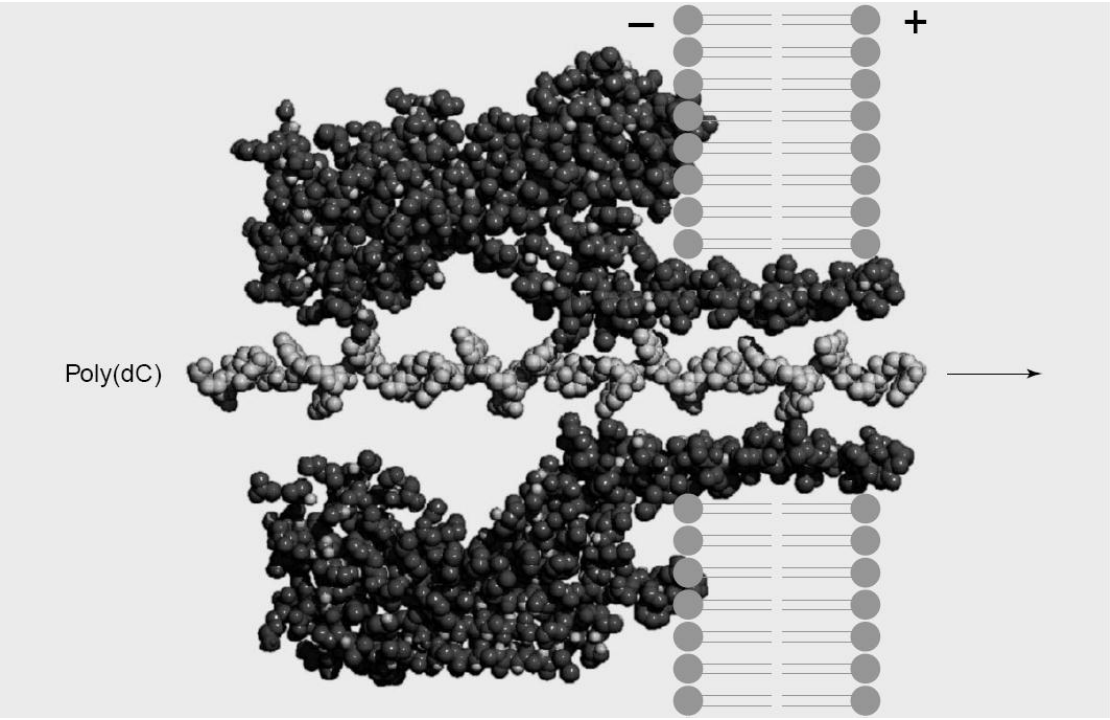

Figure 1.1. Cross-section of assembled heptameric structure of α -HL in a lipid bilayer [7]. *A double-strand of DNA is shown traversing the nanopore.*

The apparatus for a typical α-HL nanopore experiment consists of two compartments filled with aqueous salt solutions separated by a lipid bilayer membrane. Since the lipid bilayer is impermeable at this time, there is no measured ionic current. α-HL is added to one compartment, and formation of the first nanopore can be observed in about 5-30 minutes as evinced by a sudden rise in the measured ionic current. At this point the compartment is flushed with fresh solution to prevent further pore formation, and the analyte may be introduced for sensing measurements. Figure 1.2 illustrates this setup and typical ionic current readings for different DNA species. Sensing applications with α-HL nanopores have been developed for single-molecule detection, identification, and quantification of a wide range of analytes ranging from TNT to divalent metal ions to

single stranded DNA and RNA [8-11]. In the first two cases, selective binding sites for the analytes are created (e.g., by genetic engineering) so that the ionic current modulation is specific only to the desired analyte and long-lived enough to be reliably observed. Measurements using α-HL also demonstrate identification and quantification of unknown analytes as well as the ability to distinguish between related species through duration and amplitude of current blockage.

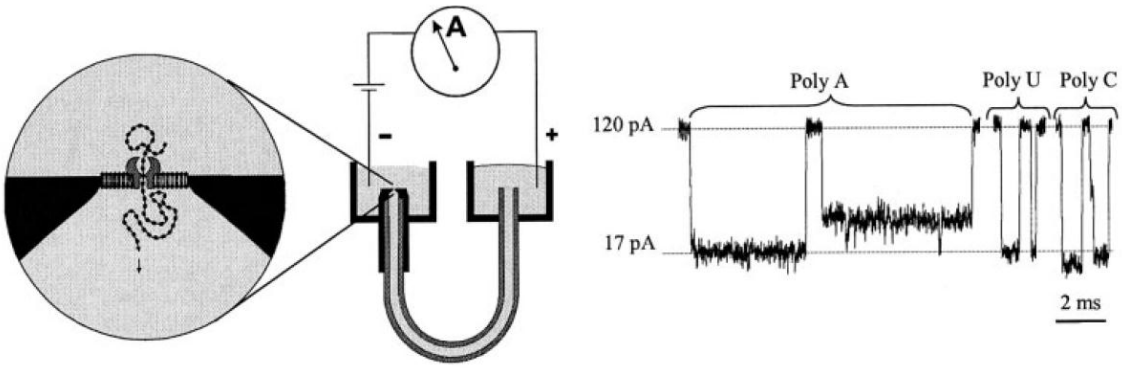

Figure 1.2 Prototype setup for α-HL DNA sensor [12]. *An example measurement of ionic current amplitude and blockage duration for polyA, polyU, polyC 100-mers.*

In the case of DNA sensing, there are two potential ways in which nanopores can be employed. The ultimate (and more difficult) objective is direct sequencing by recognizing and distinguishing individual bases on a single DNA strand. This method requires high enough sensitivity in measuring the ionic current change in response to each base passing through the pore, such that the relative changes in amplitude can be used to separate and identify every base in the sequence. The α-HL nanopore is approximately 25 DNA bases in length. Although there is a limiting constriction in the α-HL nanopore that has a length comparable to a single base, the measurement noise (~ 1 pA) is too high to detect individual bases as they pass through the constriction (with a time scale of ~ 1 μs per base). Hence, the initial focus has been on using the nanopore to determine the length of DNA strands. This would allow coupling of nanopore detectors to

the well established technique of polymerase chain reaction (PCR). Thus, nanopore detectors could replace the current processing of PCR-generated samples by gel or capillary electrophoresis. Accordingly, nanopore detectors will require the capability to distinguish a DNA strand of length N bases from a strand with $N+1$ bases.

Work in the latter direction has taken multiple approaches; important steps include demonstrating the ability to distinguish between DNA molecules of slightly different lengths and/or compositions [12]. In one study using α-HL nanopores, six DNA samples 100 bases in length but with varying compositions were shown to have distinguishable statistical translocation properties, even in cases where the overall compositions of two DNA molecules were identical while the base sequences differed (Figure 1.3). The ionic current data from repeated translocation events is collected and interpreted in the form of a histogram or event diagram. A translocation event is indicated by a drop in current, the duration of which is assumed to be directly proportional to the length of the strand. The varying amplitude of the events may also be useful in identifying specific bases or sets of bases along the strand.

Other experiments have used strategies to slow down the translocation of DNA through the pore, thus allowing data collection from a larger number of ions as each bases passes the pore constriction. This would presumably increase the signal-to-noise ratio to allow DNA strand lengths to be distinguished with higher resolution, or even allow individual bases to be distinguished. For example, DNA ‘hairpins’ are single strands with a small portion of the sequence (at the end of the strand) being composed of two blocks of complementary bases. Thus, the end of the strand curls back on itself to create a ‘hairpin’.

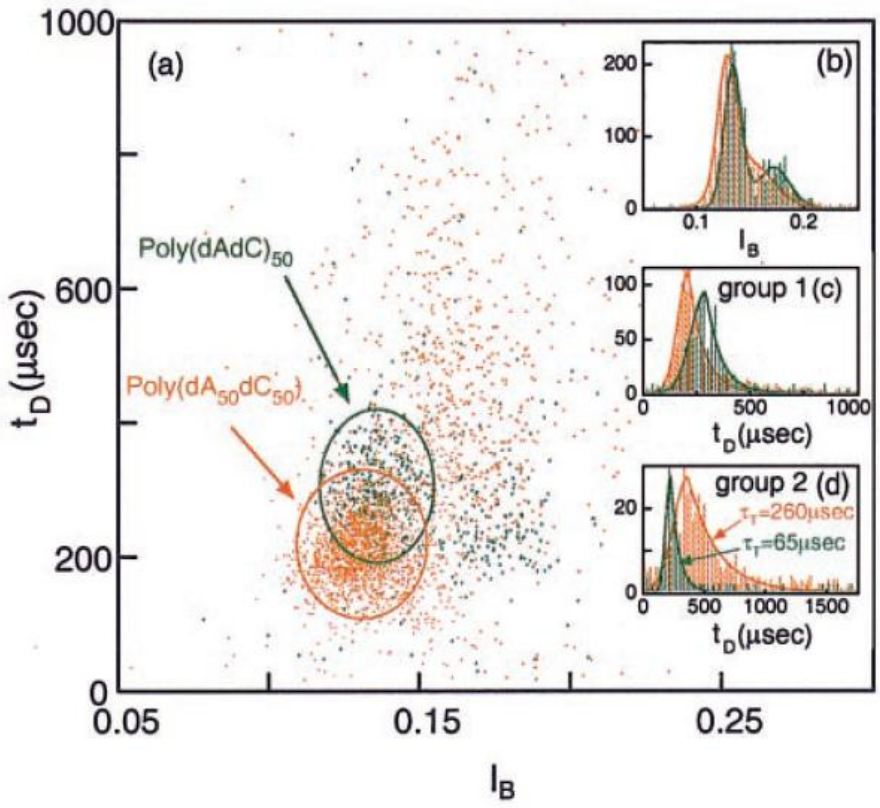

Figure 1.3. Event diagram for translocation events of poly-(dAdC)50 and poly-(dA50dC50) 100-mers in two separate experiments, indicating differentiability on basis of the sequence, despite identical overall composition [13].

The hairpin portion is too large to travel through the constriction, and hence is trapped in the vestibule while the single-stranded portion partially traverses the pore. Considering the time taken by the hairpin portion to dissociate and follow the rest of the strand through the pore, there is an, overall 5- to 10-fold decrease in the translocation rate. Research has shown that with the hairpin approach, the ionic current readouts from strands varying only by a single base in length are distinguishable from each other [14, 15]. Additionally, strands identical in length and composition except for a single base mismatch in the duplex, can also be distinguished.

These advances show promise for α-HL in nanopore sensing applications. However, there are intrinsic disadvantages in working with nanopores made from soft matter [7, 16, 17]. The α-HL nanopore is not very robust and cannot be maintained for extended periods (greater than 1 day). Although advances towards single-base resolution have been made, the limiting signal-to-noise ratio issues (caused by fast translocation and low ionic conductivity) continue to hinder their applications to DNA sequencing. Additionally, computer simulations of DNA transport through the α-HL nanopore have revealed their intrinsic structural limitations. Brownian dynamics simulations of DNA translocation through α-HL pores correctly predicted the presence of multiple peaks and long tails in translocation time distribution curves commonly observed in experiments (e.g., insets in Figure 3). These features are undesirable since it then becomes impossible to distinguish strands differing slightly in length. The simulation studies indicate that the pore geometry, particularly the vestibule (Figure 1.1), is the primary source of the low length-resolution of the nanopore. Due to the large volume available in the vestibule, the translocating strand can adopt a large number of configurations as it passes through the pore, thus resulting in a wide translocation time distribution. This finding was further supported by carrying out simulations of DNA translocation through a smooth cylindrical nanotube of comparable size, in which case a much narrower translocation time distribution was observed [18]. In conclusion, degradability and intrinsic limits on resolution due to complex pore geometry are the main problems in DNA sizing or sequencing with α-HL nanopores. These issues have led to a shift towards fabrication of solid-state inorganic nanopores that allow greater robustness and better control over pore geometry.

1.3 Solid-State Nanopore Devices

Development of solid-state nanopores for DNA sequencing and other applications is an approach rather different from using α-HL nanopores that rely on biological self assembly and genetic engineering. Nanopores formed in solid state materials are subject to completely different design considerations that resemble those found in semiconductor and microelectronic device manufacturing. The first critical design consideration is the pore size, which should ideally be narrow enough to accommodate one strand of DNA at a time and short enough to instantaneously attribute the blockage in ionic current to a single base during translocation. The pore diameter is thus chosen on the order of the diameter of single stranded DNA, in the range of 2-10 nm. The nominal pore length is essentially determined by the thickness of the solid-state thin film (e.g., silicon nitride) through which the nanopore is fabricated. However, the effective pore length may be shorter than the film thickness if the pore has a strongly tapered or conical shape. Thus, the pore length and diameter are ultimately a function of various empirical parameters, such as the material in which the pore is being fabricated (e.g., silicon nitride, silicon dioxide), the diameter of the beam (ionic or electronic) used to create the pore, the intensity of the beam (i.e., the ionic or electronic flux contained within the beam), and the exposure time. Mechanical, chemical, and electrical properties of the thin film material can all be of importance. In general, the materials should be rigid, mechanically robust, impermeable, and tolerant to processing under wide ranges of temperature and pressure. Silicon wafers are the substrates of choice, while silicon dioxide (SiO_2) and/or silicon nitride (Si_3N_4) thin films can be deposited or grown on the substrate and used to produce a nanopore. Silicon is used widely in micro- and nano-fabrication due to its abundance, crystallinity, availability of "planarized" manufacturing processes, and desirable properties as a semiconductor. Silicon nitride is robust and non-reactive whereas silicon oxide is hydrophilic and electrically insulating; both can be deposited to nanometer

precision. However, there is currently no systematic information in the open literature about the effects of these variables on the properties of fabricated solid-state nanopores.

The processing strategy usually starts with fabrication of relatively large holes and reduction of pore size (usually by at least an order of magnitude) in each material removal step, until a nanopore of desired size is formed. In a typical process, the silicon substrate (300-550 μm in thickness) is used to deposit layers of silicon nitride and/or oxide. The silicon is etched from behind (using an appropriate photolithographic mask and an etchant such as potassium hydroxide or tetramethylammonium hydroxide) to expose a square window of size 10-50 μm below the nitride/oxide layers. Next, these layers are attacked from the top using combinations of etchants (such as reactive ion etching for silicon nitride and buffered oxide etch for silicon dioxide) until a free-standing membrane of the desired thickness (< 50 nm) is exposed. Finally, the nanopore is produced in this free-standing membrane. Many of the steps leading up to the formation of the nanopore (such as deposition, photolithography, and wet and dry chemical etching) are well characterized and commonly practiced. However, the nanopore reproducibility, nanopore size control, and stability of the thin membrane are much less understood. The earliest reported solid-state END fabrication method [19, 20] used controlled ion beam milling to generate a nanopore. This process begins with deposition of a 500 nm low-stress silicon nitride film on the front-side of a (100) silicon substrate, followed by patterning of a hole of diameter 500 μm in the backside of the wafer by photolithographic techniques. The silicon is then etched in solution at a 54.7^{o} angle following the (111) crystal planes, until the nitride layer is exposed and free-standing, creating a 25 μm square window. At this point, two approaches can be taken. In the first, a bowl-shaped cavity about 100 nm wide is fashioned in the newly revealed nitride surface using reactive ion etching (RIE) or focused ion beam (FIB) milling. Next, material is removed from the cavity until the remaining thickness of nitride at the center

is 5-10 nm. This surface provides the desired length of the pore, and the pore itself is created by milling the surface with a focused ion beam tool. The second approach uses RIE or FIB to open a large through-hole of size 60 nm which penetrates the silicon nitride. The ion beam is then used to laterally deposit material to the pore, filling it in to the desired size with nanometer precision. This technique of manipulating matter at the nanoscale by bombarding a sample with ions in a controlled manner is introduced as "ion beam sculpting". The basic idea is that each incident ion removes an atom of material at the surface. However, depending on processing conditions of temperature and flux, ion exposure can lead to lateral deposition of material.

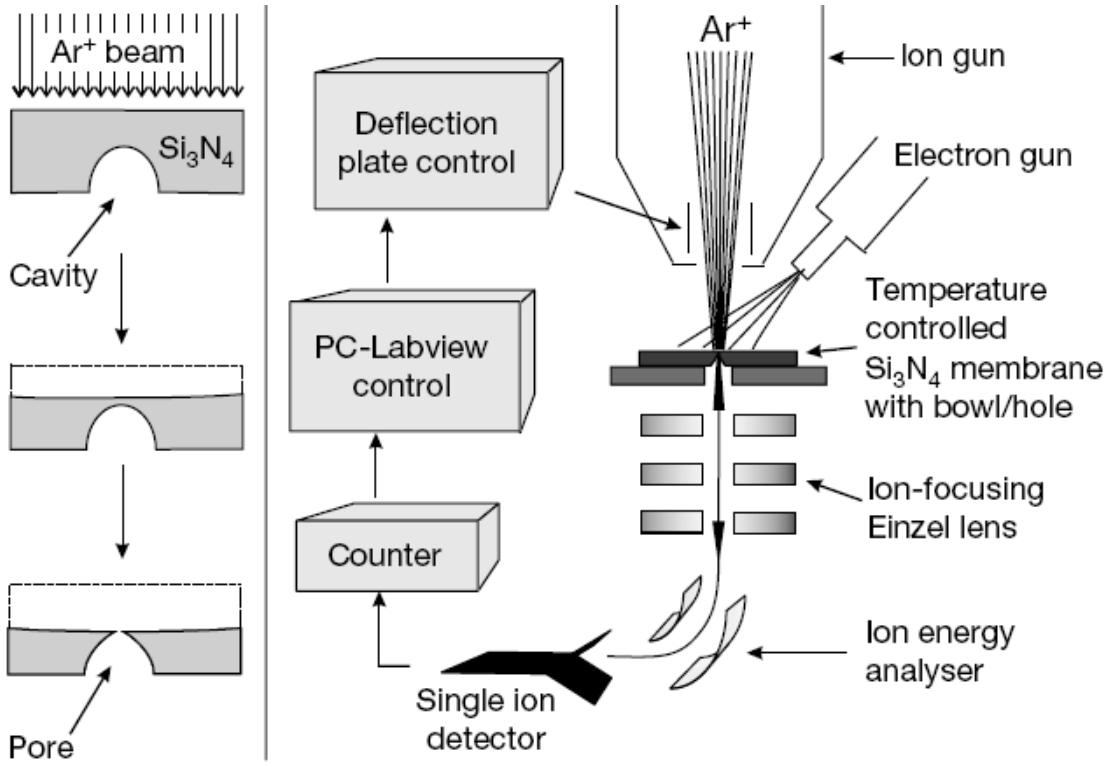

Figure 1.4. Opening up a nanopore in a free-standing silicon nitride membrane using a focused ion beam, and the dual beam setup with detection and feedback mechanism [19].

One reported experimental setup of this mechanism consists of a dual-beam tool which erodes the surface with Ar^+ ions while using a transmission electron microscope (TEM) for imaging of the surface. The apparatus contains a feedback mechanism which monitors the number of ions transmitted through the sample and is used to regulate the milling rate. The beam is focused on the surface and material is sputtered until formation of a nanopore is observed. TEM images combined with the ion rate counter characterize pore formation. Figure 1.4 demonstrates the strategy and apparatus used in ion beam sculpting of a silicon nitride layer by material sputtering. Pore sizes of 3 and 10 nm have been demonstrated in 5-10 nm free-standing silicon nitride using ion beam sculpting.

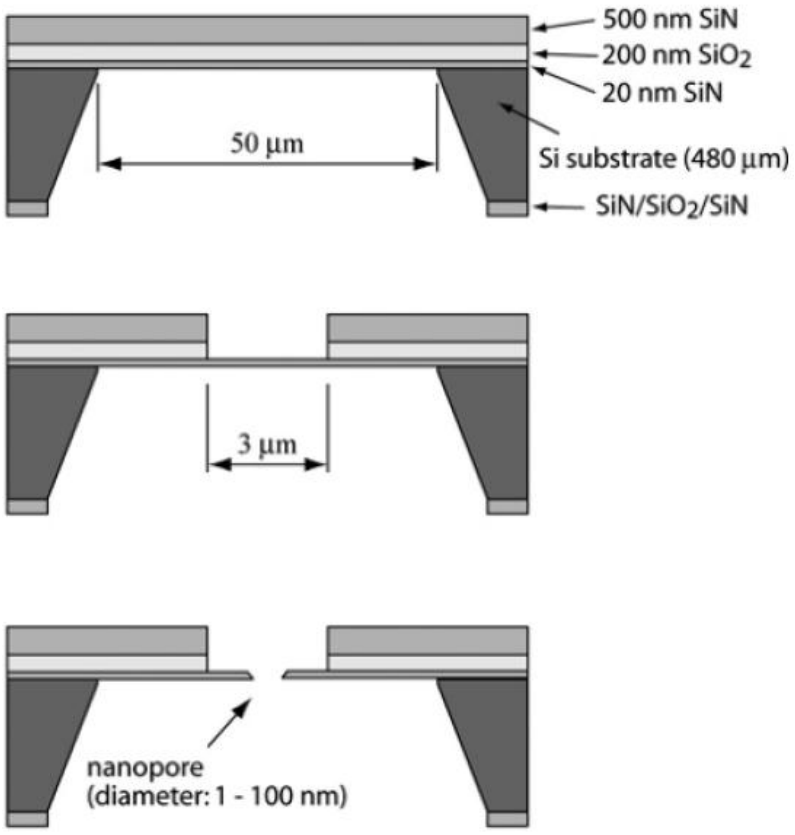

Figure 1.5. Basic fabrication steps, opening a large window in silicon to expose the nitride from the bottom, followed by patterning and etching of the topside, and using high voltage TEM to make the nanopore [21].

Another method used to produce nanopores is the application of a tightly focused, high-voltage (200-300 keV) electron beam (generated in a transmission electron microscope) to a thin free-standing membrane supported on a silicon wafer [21-27]. The film is usually silicon nitride or oxide (20-50 nm thin), deposited and exposed using sequential photolithography and etching steps as described earlier. An example of the fabrication in such a configuration is shown in Figure 1.5. In this case, the purpose of the top layers is to provide mechanical support and reduced capacitance for the free surface. We note that the solid-state fabrication methods discussed here are capable of mass producing nanopores in arrays on a single wafer relatively quickly and cheaply. Once a nanopore has been generated in a free-standing surface by one of these methods, the nanopore can be directly used in sensing applications or undergo further processing for a different application, such as a nanoscale electrode [21]. Several current efforts are underway to use these pores to achieve single base resolution DNA sequencing. In a translocation experiment parallel to the α-HL detector, the pores are immersed in ionic solution joining two chambers. The DNA sample is usually double-stranded (which is too large to traverse the α-HL pore).

Preliminary DNA sensing experiments with solid-state ENDs have verified that translocation is actually taking place. Data is analyzed in event diagrams similar to those obtained with α-HL nanopores. Effects of variation of important factors such as temperature, pH, voltage, and salt concentration on translocation have been studied (note that biological nanopores have much lower tolerance for changes in pH and temperature). For example, experiments in which pore sizes of 3 nm and 10 nm were compared [20] demonstrate that a portion of the DNA traversing the larger pore experienced folding during translocation. As might be expected, the current blockade is approximately doubled since the pore accommodates twice the number of bases at a given time. The time distribution plot of this phenomenon is shown in Figure 1.6. Experiments carried out

at varying pH have demonstrated capabilities of solid-state ENDs to discriminate between single-stranded and double-stranded DNA [24].

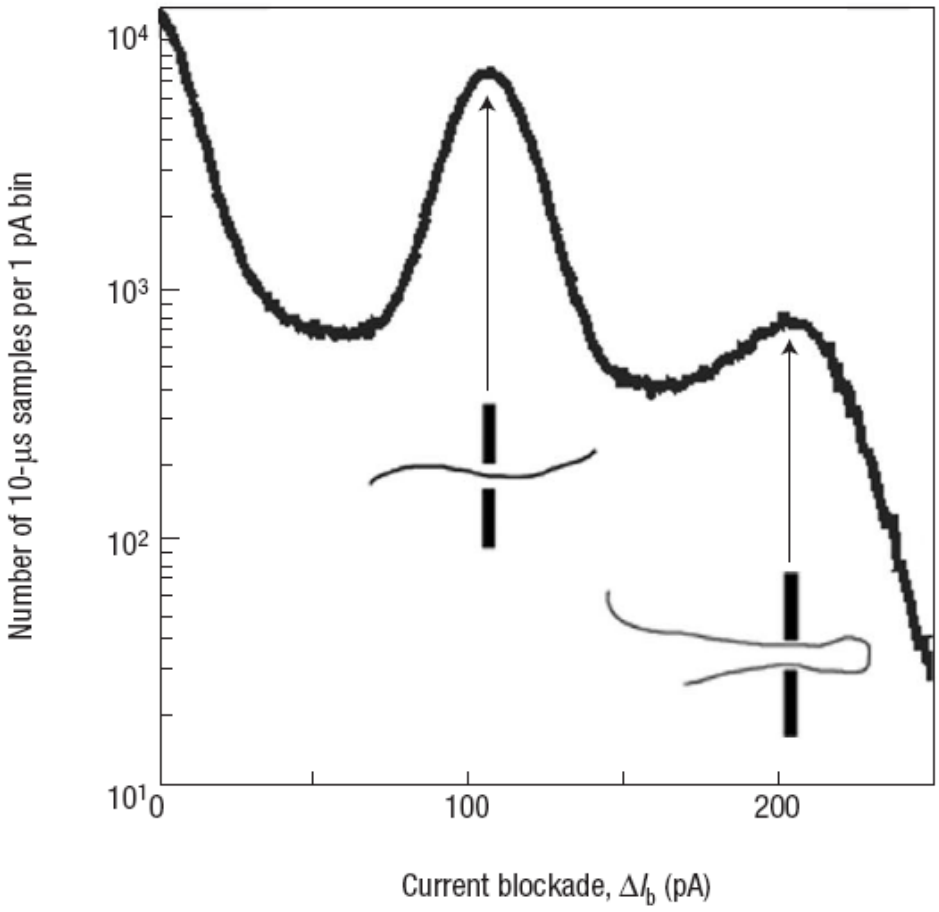

Figure 1.6. Instantaneous time distribution of current blockades in 10 nm pore indicative of simple translocation and folding during translocation [20].

1.4 Dimensions and Morphology of Nanopores

In solid state nanopore fabrication, one of the primary advantages is the ability to design and control pore dimensions. Previous literature offers a limited degree of experimental characterizations of pore geometry following fabrication by TEM or FIB. This thesis examines electron beam lithography (EBL) as a candidate for END processing. It is therefore an important point of interest to characterize the internal pore

geometry produced during the EBL process. In this thesis, a combination of detailed physical modeling of the EBL process, in conjunction with experimental characterizations, is used to understand the morphology of EBL-fabricated nanopores and its dependence on processing conditions.

EBL produces patterns by bombarding the photoresist with electrons. The electrons scatter within the resist and cause chain scission events (if the resist is positive) or crosslinking events (if the resist is negative). The resist is then immersed in a developer solution, causing the more soluble areas of the resist to be removed. There are several approaches to modeling pattern geometry in EBL. In one common methodology, each component of the resist patterning physics is examined individually. The first step is the electron trajectory in the substrate. This is generally modeled by a Monte Carlo method, which traces individual electrons through the substrate as each experiences scattering events based on probability distribution functions. Figure 1.7 shows simulated trajectories of 100 electrons in PMMA on silicon [28].

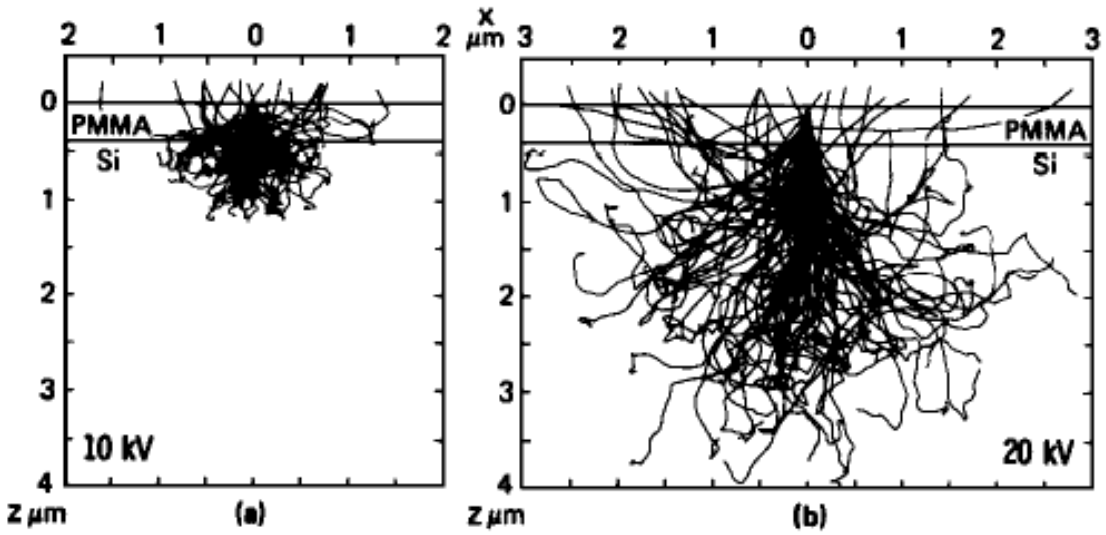

Figure 1.7. Electron scattering behavior in PMMA photoresist on silicon substrate at 10 kV (left) and 20 kV (right) [28].

For a large enough sample size of electrons (10^6 or higher), the simulated electron trajectories can be used to calculate the energy deposited in the resist. The deposited energy depends on processing conditions such as the accelerating voltage, beam current, process blur effects, and dose. Once this energy distribution is determined, the development of the resist can be modeled by semi-empirically determined models for the resist. This is demonstrated for PMMA in Figure 1.8 [29].

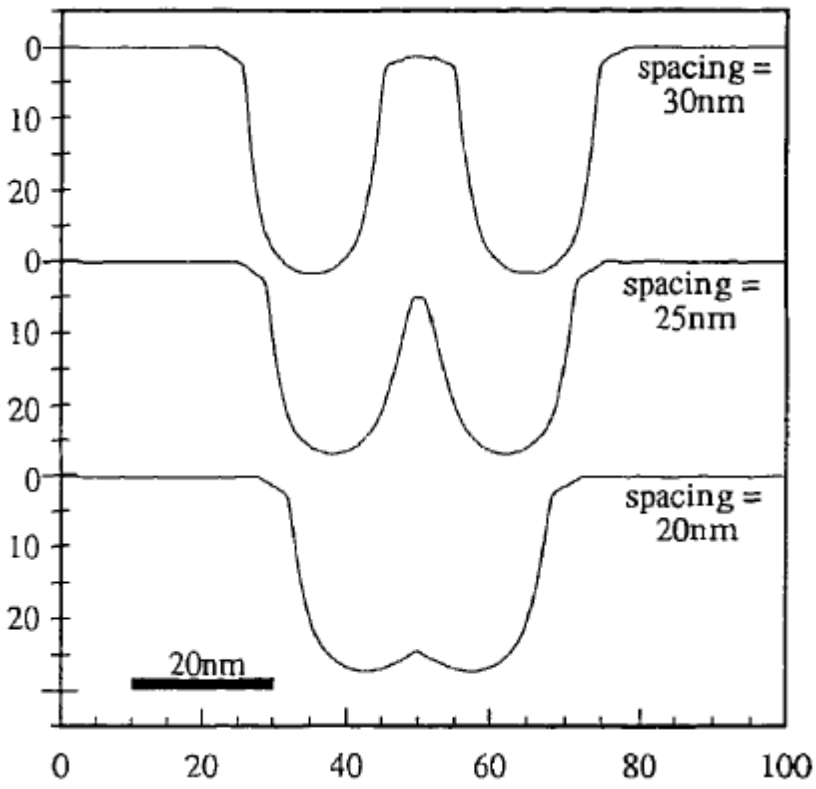

Figure 1.8. Developing lines in PMMA photoresist with 20 nm, 25 nm, and 30 nm spacings.

1.5 Prospects and Challenges in END Science and Technology

The potential advantages of a single-molecule method based upon direct reading of the sequence from unamplified DNA, are increasingly accepted. Conceptually, it is

natural to pursue the development of a technology that directly reads sequence information from individual genome-length DNA, rather than the much more complex sample preparation and analysis methods necessitated by current approaches. The development of such a technology is extremely challenging and is projected to take at least a decade of science and engineering research targeted at device fabrication, detection methods, and the dynamics of biomolecule transport in confined nanopore spaces. It is, however, clear that even without 'single-base' resolution, the development of ENDs is of high importance in biomolecule analysis. For example, the capability of the END to accurately size DNA strands several orders of magnitude faster than electrophoresis offers the possibility of replacing an important component of current DNA sequencing technology. There are also a number of other applications wherein single-nucleotide resolution is not required. For example, ENDs with functionalized sites can be employed to detect extremely small levels of toxic agents such as the anthrax lethal factor (LF) and edema factor (EF) [30], based upon modulation of END properties (such as ionic current) by specific binding events occurring inside (or in the vicinity of) the nanopore. The use of α-hemolysin nanopores with various molecular 'adapters' has been shown to lead to new biomolecule sensors that offer much higher sensitivity, much faster response, single-molecule resolution, and potentially lower cost, than conventional biomolecule sensors based on measuring the collective response from a macroscopic ensemble of sensing/detection sites [5, 31, 32]. Similarly, solid-state nanopores fabricated from materials such as silicon dioxide, could be functionalized [33] with biomolecules of various types and used to analyze proteins [34-36], viruses, and other biomolecular analytes with all the advantages (e.g., speed, sensitivity) offered by ENDs. Furthermore, future ENDs need not be restricted to measurements of ionic current modulation. Other proposed detection methods, such as transverse electron tunneling between metal electrodes on the nanopore walls [37] and fluorescence resonance electron transfer (FRET) measurements [38] between quantum dots embedded in the nanopore walls, may

lead to entirely new capabilities that cannot be achieved by ionic current measurements alone. Concurrently, advances in operation and control methodologies for nanopore operation [39, 40] can allow optimal operation of the END. Figure 1.9 is a schematic of the possible appearance of a future END device.

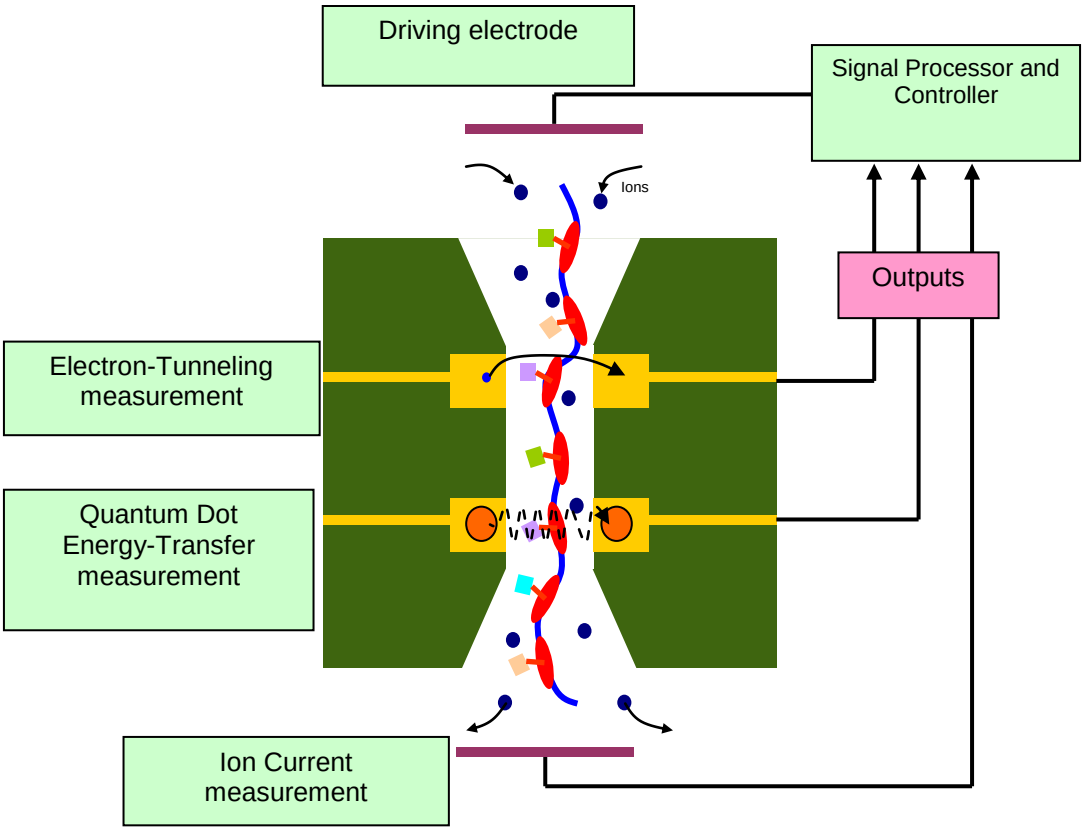

Figure 1.9: Conceptual schematic of a future Engineered Nanopore Device (END).

In order for ENDs to be successfully commercialized for both "short-term" applications (that do not require single-nucleotide resolution) as well as "long-term" applications (such as genome sequencing with single-nucleotide resolution), two important challenges must be overcome that are common to all the variations of ENDs. Firstly, there is currently no strategy for reliable and reproducible fabrication of large

arrays of solid-state nanopores that can be operated in parallel. Previous reports have focused on fabricating prototype single nanopores using ion track etching, ion milling, or electron microscopy [19, 21, 24, 41]. Encouraging results have been obtained, and it is clear that each technique involves a number of experimental parameters (e.g., the nature of the substrate in which the nanopore is being created, the energy and diameter of the ion/electron beam, the exposure time) that strongly influence the quality of the nanopores produced. Future ENDs may be operated in massively parallel arrays to provide bioanalytical information at a small fraction of the time and cost of present-day technology. In the fabrication of large arrays of nanopores, these characteristics cannot be monitored manually, and hence they must be known to a degree of precision similar to that achieved in the fabrication of microelectronic devices. However, there is currently very little systematic knowledge of the relationship of nanopore fabrication parameters to the structure of the resulting nanopores [42]. It is essential to develop a fabrication strategy that is based on the knowledge of 'process-product' relationships of nanomanufacturing tools as pertaining to nanopore fabrication, and then to demonstrate the application of this strategy to create and characterize arrays of high-quality ENDs. This capability can then be interfaced with existing methods of integrated circuit and microfluidic fabrication to build completely integrated systems containing on-chip detection electronics and microfluidic sample handling systems. The second challenge has already been discussed extensively in this work, i.e. the issue of controlling the DNA dynamics and developing methods to achieve single-nucleotide resolution in ENDs. Current directions being pursued in multiple research laboratories create considerable optimism that these challenges will be overcome. It is likely that the commercial appearance of END systems will require close collaborations of scientists and engineers to ultimately deliver robust, high-speed, low-cost bioanalytical platforms that retain all the intrinsic advantages offered by ENDs. Such a development would have a truly

revolutionary impact on innumerable areas in biotechnology and medicine that require the ability to analyze complex biomolecular mixtures.

1.6 Objectives of this Thesis

The main goal of the present work is to address a key question in END science and technology, i.e., the challenge of developing, characterizing, and optimizing a wafer-scalable process for fabricating large numbers (e.g., hundreds) of individual nanopores on a wafer. Based upon our analysis of the previous fabrication methods discussed in the literature, we are in a position to ask the following questions of significance:

1. *What technology or combination of processing steps can reproducibly produce arrays of nanoscale features across a wafer ?* The resolution of an unmodified FIB was explored as well as traditional lithography, EBL, and atomic layer deposition (ALD) to tune pore size. TEM was rejected as an option for wafer scale processing due to the substantial time required for calibration, and the inability to automate and pattern an entire wafer. However, the concept of using an electron beam to pattern the features was retained by the use of EBL for initial definition of the nanopores. However, to produce sub-20-nm nanopores of tunable size, the use of ALD is hypothesized to be necessary.

2. *How versatile is the process for producing a range of feature sizes?* The method presented here was evaluated for its ability to reproducibly yield features ranging in size from 10 nm to 1 micron. As features are decreased in size, the aspect ratio of the pore is increased, making it more difficult to remove all the material and accurately define the pore. Nanopores of order 10 nm are naturally more difficult to fabricate and characterize than larger pores, but larger pores require a greater dose of the electron beam and therefore take more time to pattern. The ability to

pattern a wide variety of feature sizes on a wafer may become useful as wafer scale ENDs are industrially manufactured, because each wafer could be patterned for use in multiple sensing applications such as proteins, DNA, and a broad range of other biomolecules. We also would like to explore the ability to pattern multiple nanopores on a single wafer. This may be useful for applications in determining particle size distributions or more complex separations if the pores are functionalized.

3. *What is the most suitable material and method of deposition for the membrane containing the nanopores?* In the literature, both silicon nitride and silicon dioxide have been used as free standing films. The author explores plasma enhanced chemical vapor deposition (PECVD) and low pressure chemical vapor deposition (LPCVD) deposition as well as quality control characterization. An important challenge was identifying different growth mechanisms intrinsic to early stages of LPCVD reaction and reconciling these with defects revealed experimentally.

4. *What characterization protocols should be established in order to assess device characteristics and quality at each process step?* It is desired to assess, both quantitatively and qualitatively, the dimensions, shape, quality, and stability of the thin film and the nanopore device at each step of processing. Previous characterizations have essentially consisted of a TEM/SEM image of the nanopore at the end of the processing scheme. There is currently no information available regarding the evolution of the nanopore dimensions and shape during wafer-scale processing, nor any statistical data regarding the stability and survivability of the nanopore-containing thin films. This work will provide a clear and quantitative characterization of these issues.

5. *What insights can be obtained from a detailed study of the EBL process and its effect on the internal pore geometry based on the processing parameters?* Due to the novel fabrication approach, there was no detailed information available in the literature (whether computational or experimental) regarding the geometry of ENDs fabricated by EBL. In this work, a Monte Carlo approach is combined with a threshold energy model to determine the internal pore geometry of ENDs under a broad range of operating conditions. An effective processing blur is determined through comparison with experimental data in several cases and the impact of secondary electron emissions and shot pattern is quantified.

To answer the above questions, it is necessary to explore the scope of END fabrication in detail. Each step of the process will be characterized and analyzed, by complementary methods wherever possible. The nanopores investigated are desired to be tunable in size from 50 nm to sub-20 nm, and are desired to be fabricated reproducibly with a high survival rate. In the following chapters, we describe in detail the development and optimization of a wafer-scale process for nanopore array fabrication, including lithographic and thin film deposition processes as relevant to nanopore fabrication, and we characterize the nanopore devices by several techniques.

CHAPTER 2

DEVELOPMENT AND OPTIMIZATION OF WAFER SCALE PROCESS FOR NANOPORE FABRICATION

In developing a process for producing wafer scale arrays of pores, several fabrication methods were investigated. Optimization of multiple steps within each fabrication method was found to be critical for the ultimate result of obtaining a wafer with a high yield of ENDs. Fabrication of the nanopores by FIB was initially attempted, but ultimately replaced by electron beam lithography. Atomic layer deposition was applied to fill in the internal pore walls to achieve smaller sizes after their original production.

All handling and processing of devices was performed in a clean room (CR) environment. The substrates used were 400 μm or 520 μm thick double side polished <100> oriented silicon wafers. The wafers were immersed in a dilute hydrofluoric acid solution to remove any native silicon dioxide immediately prior to processing. A set of important parameters was rigorously monitored throughout each process to evaluate the reproducibility and quality of films and pores produced. These parameters include: the thickness and uniformity of the film containing the nanopore; the size distribution, geometry, and SEM imaging of the nanopores; the appearance of the front and backside surfaces, i.e., particles, scratches, and other defects. Several wafers and individual devices underwent different degrees of processing to demonstrate reproducibility and to show the range of pore sizes and film thicknesses that could be achieved.

2.1 Backside Wet Etch of Silicon

In order to expose the free standing film on the wafer, the silicon needed to be back etched entirely through the wafer. To do this, two commonly used options were considered: a wet etch in a bulk solution, and a 2 step sequential plasma assisted dry etch known as the Bosch process. A wet etch was chosen over a dry etch due to the limitation of the Bosch process in achieving the aspect ratios required to etch through a wafer at smaller feature sizes, in addition to the lower etch rates using typical parameters [43]. A wet etch is also more cost effective in scale up and commonly used in industry for similar applications.

From this point, two wet etch methods were considered to expose the silicon nitride film: tetramethyl ammonium hydroxide (TMAH) and potassium hydroxide (KOH). The objective of the subsequent studies was to identify and develop process parameters to *maximize the percentage of free standing films that survived the wet etch.* Several parameters were considered in designing the experiments. The most natural parameters that were controlled were concentration and temperature. However, moderating these values alone was found to be insufficient.

The wafer was immersed in a bulk etch solution while encased in a holder which protected the backside. It was expected that micropyramids may form in the silicon during either etch [44], but this effect was only encountered during TMAH etch. The formation of micropyramids by TMAH is shown in Figure 2.1.

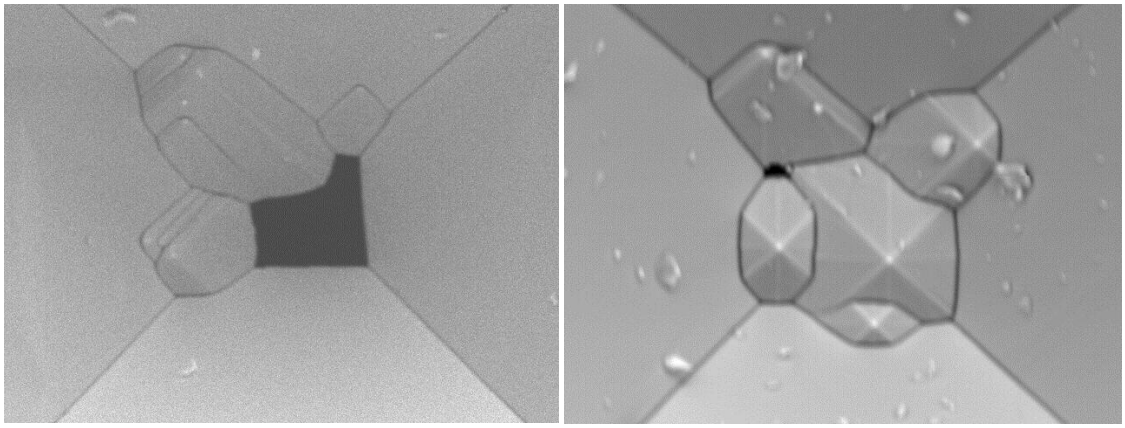

Figure 2.1. Micropyramids of silicon produced during 25% TMAH etch.

The literature theorized that these pyramids resulted from manufacturing defects in the wafer coupled with incomplete dissolution of the intermediary hydrated oxide formed on the silicon surface during the etch, and further, that these effects could be controlled by changes in concentration, temperature, agitation, duration, and/or addition of a surfactant [45, 46].

The formation of the pyramids was problematic because it caused nonuniformity in the etch rate across the wafer as well as random nonuniform etching regions on each END, which compromised reproducibility. In order to address this effect, the theorized mechanism of reaction was more closely examined. The overall reaction described in the literature [47] is

$$Si + 2OH^- + 2H_2O \rightarrow SiO_2(OH)_2^{2-} + 2H_2$$

The hydrogen gas byproduct of this reaction was observed to form large millimeter sized bubbles on the surface of the wafer during the etch. These bubbles existed on each END across the wafer and would remain at each etch site for several seconds before being released. This effect was described in the literature and formation and release of these

bubbles was hypothesized to be a visual indicator of pseudomasking and pyramid formation.

It was found that removing a sample from the solution and subsequently placing it back in solution for approximately 1 minute drastically reduced or removed the micropyramids from a large number of the surfaces. This supports the hypothesis in the literature that the formation of hydrogen bubbles creates a pseudomask on the surface and results in the tip of what becomes a pyramid. By briefly removing the wafer from the solution and washing it, the hydrogen bubbles would be freed, and a short etch would remove the offending features rapidly before the creation of many new pyramids. A surface etched by TMAH with no micropyramids is shown in Figure 2.2.

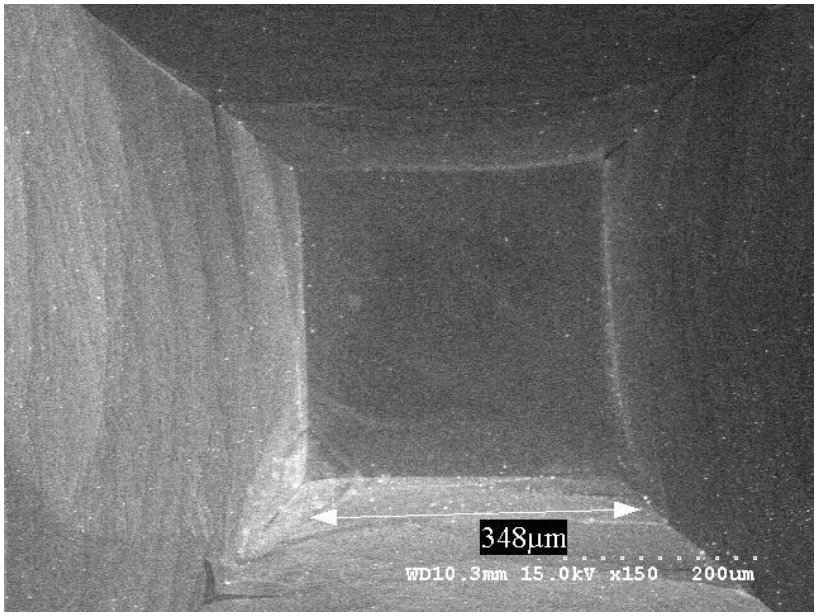

Figure 2.2. A trench etched in TMAH free of micropyramids.

From this Figure, there was a clear element of surface roughening produced on the sidewalls of the silicon during the TMAH etch. The roughening may be related to pyramid formation in its origin, that is, hydrogen bubbles which cause local variances in

etch rate across the surface. Surface roughness of the trenches was not further investigated because it was not an impediment to the functionality of the ENDs.

During the course of the TMAH experiments, the formation of pyramids was never fully eliminated and < 1% free standing films survived the process. Thus, the use of KOH was investigated to perform the backside wet etch. Lower concentrations (15-20%) did not yield any surviving thin silicon nitride membranes (20-50 nm). 45% KOH initially did not yield any surviving devices either. It was found that the solution needed to be saturated with isopropanol (IPA) in order to yield the highest rate of surviving devices. It is hypothesized that the alcohol reduced the surface tension on the membrane during the etch. The reduced stress on the film resulted in improved survival rates.

Upon completion of the etch, it was found that the method of separation of the wafer from its carrier was critical to device survival. It was found that the best results were obtained when the wafer was removed while still immersed in solution. This was because of the surface forces of the liquid between the film and the carrier. Hence, once the etching was completed, the wafer holder with wafer was submersed in a solution of water and the wafer was removed from the holder with a gentle sliding motion while it was submerged. The wafer was then slid upwards and removed from solution. A schematic of this procedure is shown in Figure 2.3.

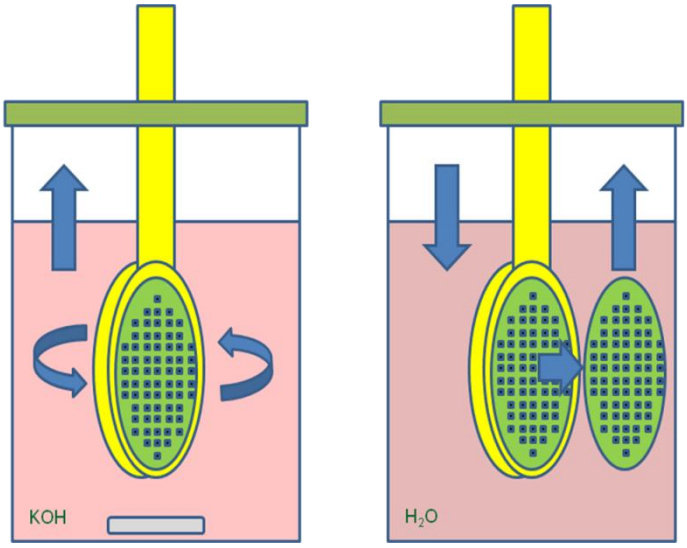

Figure 2.3. Procedure for separation of wafer from carrier after KOH etch

2.2 Optimization of Wafer Scale Fabrication Method

In developing the process, several methods were considered to achieve the goal of exposing an ultrathin free-standing membrane containing a nanopore. In the first fabrication method, the backside wet etch was performed at the beginning of the process. This allowed the pore to be produced at the end of the process by different methods on the same wafer. The composition of the free standing film was a 6 μm thick silicon oxide film deposited by plasma enhanced chemical vapor deposition (PECVD). Silicon oxide was chosen because of its hydrophilicity, which was hypothesized to allow the conducting solution to more readily wet the internal pore wall. PECVD was used for the deposition because it allowed integration of electrodes onto the device in a previous step. The film thickness deposited was so large initially to preserve the film during the backside wet etch of the silicon.

The mask used for the backside wet etch contained different size features ranging in size from 575 μm to 775 μm to give different aspect ratios of the final free standing surface. This was to empirically determine the mechanical resilience of the free standing film to the processing conditions in the subsequent steps. The backside mask material for the wet etch was a 6.5 micron thick layer of silicon oxide deposited by PECVD. The photoresist used was Futurrex NR-5 8000 spun at 1000 rpm for 40 s, cured at 150 C on a hot plate, then exposed at 365 nm at 5 mW/cm^2 for 38.5 s. The wafer was then cured at 100 C on a hot plate for 1 minute and developed in Futurrex RD-6 solution for approximately 1 minute. Contact profilometry was used to ensure full development. The backside etch of the silicon was then performed in a wafer holder in solution with TMAH or KOH. The details of the backside wet etch were discussed in the previous section. Next, FIB was applied to the free standing film from the backside in two steps. The first step created a large bowl shaped cavity of radius approximately 5 μm. The next step produced a smaller cavity within the larger one, which was then milled until a through hole was produced in the film. This is demonstrated in Figure 2.4.

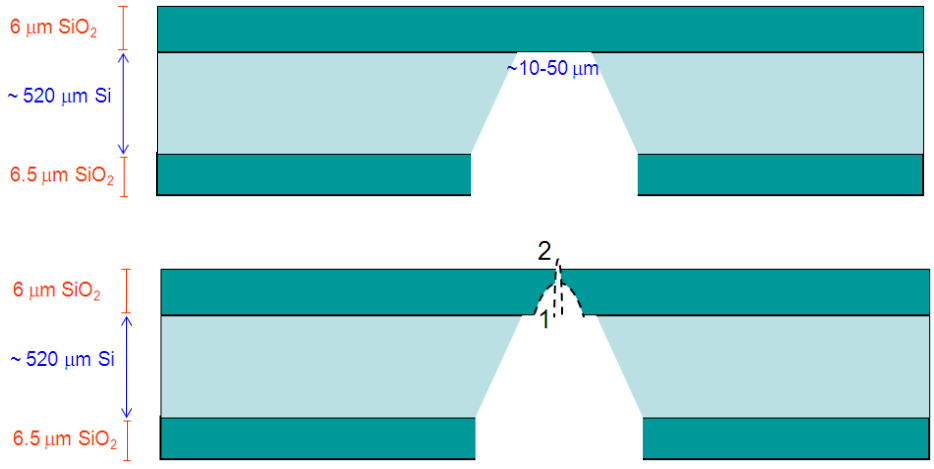

Figure 2.4. END Fabrication using PECVD silicon oxide and FIB

The second fabrication method used FIB to expose the free standing surface from the back side and then the front side, followed by EBL or TEM to produce the pore in the

film. First, the wafer was deposited with 6 microns PECVD silicon oxide on the front side and consecutive layers of 50 nm silicon oxide, 20 nm silicon nitride, 200 nm silicon oxide, and 500 nm silicon nitride. Then, the large backside features were etched into the silicon oxide by lithography. The silicon in the features was etched through the wafer to expose the films on top. The method is shown in Figure 2.5.

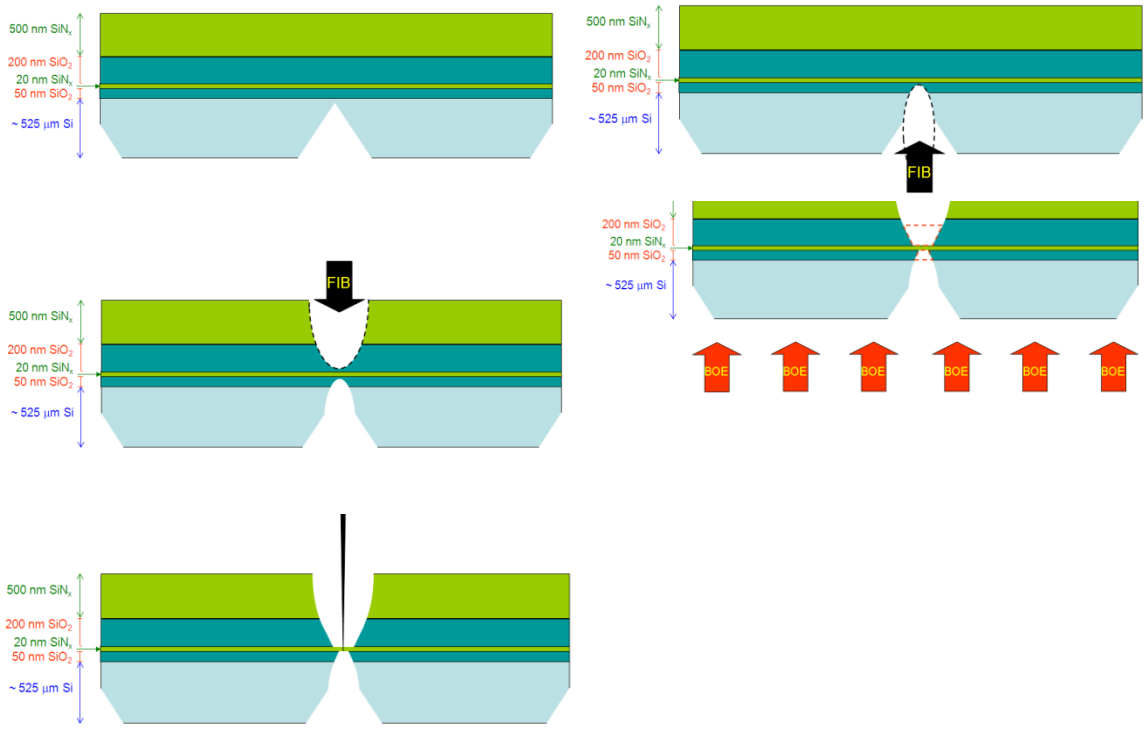

Figure 2.5. END fabrication method using FIB and BOE to expose the free standing surface, and EBL or TEM to produce a nanopore.

The issue with these fabrication methods was the limitation of the FIB to produce the desired aspect ratio in the milling steps, as well as the resolution of features attainable. The next method developed used lithography steps to eliminate the use of FIB and also eliminated one of the topside layers. First, 20 nm PECVD silicon nitride was deposited on the top side, followed by 200 nm PECVD silicon oxide and 500 nm PECVD silicon nitride. Next, the wafer was backside etched to expose the films, and consecutive

lithography steps could be used to expose the ultrathin silicon nitride layer. This is shown in Figure 2.6.

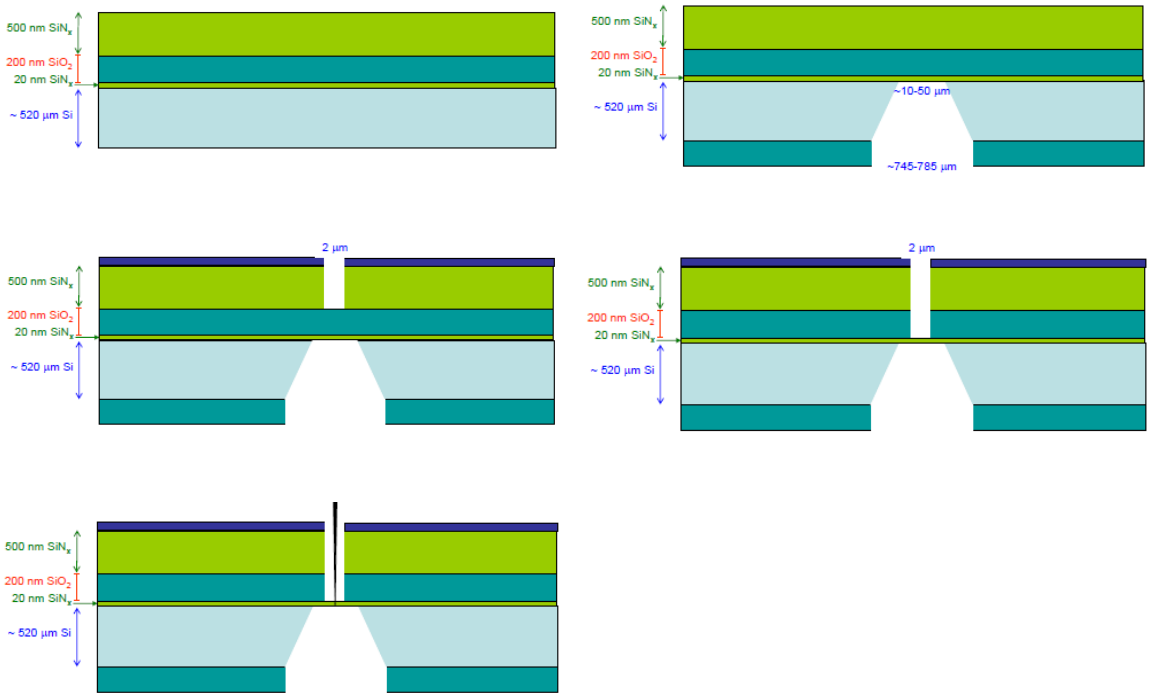

Figure 2.6. END Fabrication method using lithography steps and backside wet etch to expose the free standing surface, and EBL to produce a nanopore.

This method was considered but not fully implemented partially due to the patterning of the pore by EBL at the last step. This method is much better suited to TEM because the film must be free standing for electrons to transmit through. For EBL to be performed after the film is back etched creates several issues. First, for the coating of the resist, the wafer must be mounted on another wafer (to avoid the pressure of vacuum), and even with this precaution it would not be clear if the films would survive a traditional spin coat. EBL would require an alignment to the films, and each step would require a great deal of caution in handling.

2.3 Pore Production Using Focused Ion Beams

Pores were initially produced using a focused ion beam (FIB). The objective was to produce and characterize a range of pore sizes from 1 micron to the smallest pore sizes possible. Pore sizes of order 100 nm were expected to be achieved, based on the specifications of the instruments.

The primary advantage of FIB was the ability to characterize and adjust the pore size in real time. Two different instruments were used: the FEI Nova Nanolab 200 and the FEI Quanta 200 3D. The FEI Nova was found to produce smaller pores with greater control. Figure 2.7 shows pores produced by FIB. The smallest pore diameter achieved was 124 nm.

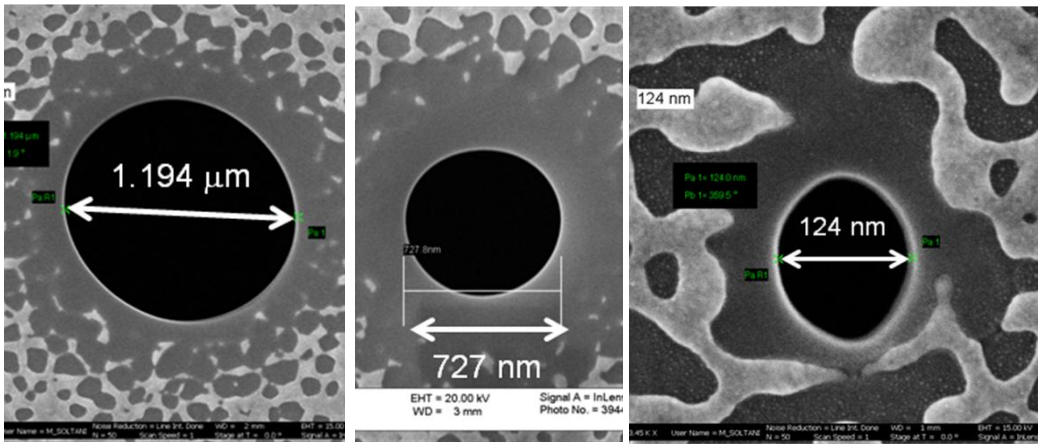

Figure 2.7 From left to right: Pore sizes of 1.2 micron, 0.7 micron, and 0.1 micron produced in 100 nm silicon nitride using FIB.

There were several issues that arose while producing pores with FIB. The aspect ratio achievable as well as the size and resolution of the features achievable was limited. The geometry of the smallest pores produced were somewhat misshapen and not well controlled. Re-deposition of material, an intrinsic result of the milling process, also

introduced a new parameter that may have affected pore geometry and was not easily characterized. For these reasons, FIB was determined to not provide an optimum means for the reproducibility, control, or nano-scale desired for wafer scale ENDs. A recent publication confirms this finding, that the resolution of a typical FIB is limited to approximately 100 nm [48].

2.4 Optimized Fabrication Method

The final fabrication method arrived at combined the simplicity of a single topside

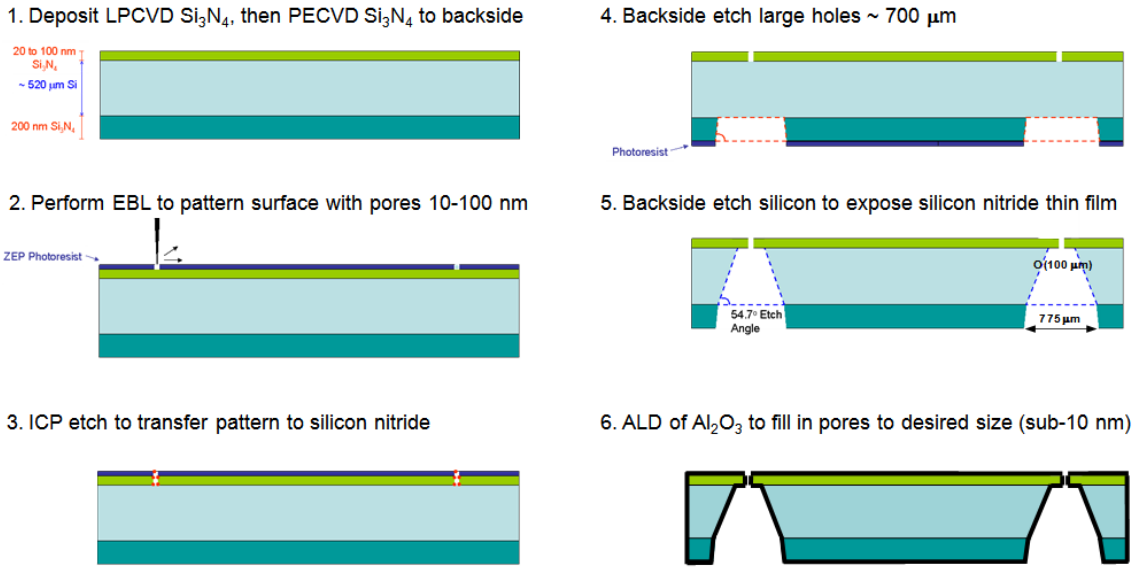

Figure 2.8 Major process steps in tunable fabrication of arrays of nanopores on a wafer.

film with the mechanical strength of LPCVD deposited silicon nitride. The pores were produced prior to the backside wet etch, which allowed them to be characterized very early on in the process. Figure 2.8 illustrates the major fabrication steps in the process. Silicon nitride (Si_3N_4) films in the 10-50 nm thickness range were deposited on a wafer using low pressure chemical vapor deposition (LPCVD) at 800^{o}C. The precursors were ammonia and dichlorosilane. Film thickness was measured at 9-13 points by ellipsometry. Next, electron beam lithography (EBL) was performed using Zeon ZEP-

520 positive resist. The pattern consisted of a 29×29 square array of nanopores spaced 2.47 mm apart, with alignment markings near the edges. There was a total of 825 devices patterned on each wafer. Larger features were patterned around 25 of the pores across the wafer, allowing these pores to be easily located in SEM analysis. A schematic of this is show in Figure 2.9.

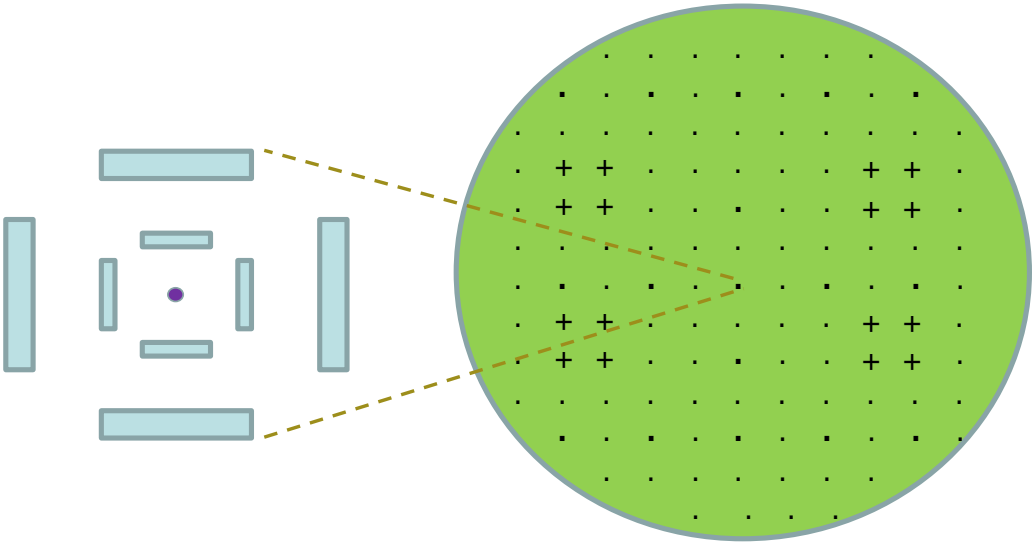

Figure 2.9. Schematic of a wafer patterned in EBL

These pores were imaged by SEM to give the size distribution and geometry. The wafer was then etched in an inductively coupled plasma (ICP) to transfer the pattern from the resist to the Si_3N_4. The precursors used were tetrafluoromethane and oxygen. Any remaining resist was removed, and the wafer underwent ellipsometry and SEM imaging to confirm pattern transfer.

Next, backside alignment was performed to pattern an equal size array of 775 μm pores on the backside. The photoresist used was Futurrex NR5-8000. The recipe was as follows: The resist was spun on the wafer at 1000 rpm (500 rpm/s) for 40 seconds, baked

on a hotplate at 150^{o} C for 1 minute, and exposed using the EVG 620 Mask Aligner at 365 nm for 38.5 seconds (at 5 mW/cm^{2}). The resist was developed using Futurrex RD-6 developer for 60 seconds or longer. Development was confirmed by measuring resist profile using the Tencor Contact Profilometer at low loads.

A second backside alignment step was performed to etch a grid in between the devices for easy separation at the end of the process. The photoresist used was Megaposit SPR-220.The process was as follows:

To obtain a high device survivability, the wafers were wet-etched while being held in a backside protecting wafer holder manufactured by AMMT Inc, in a 45% KOH solution saturated with isopropanol (IPA) at 80-85^{o}C to expose the free-standing films and open the other end of the pores. Optical microscopy was used to determine survival rate, followed by SEM for final pore size distribution and to confirm proper alignment. Finally, atomic layer deposition (ALD) of Al_2O_3 was performed to 'fill in' the open pores to a smaller size. The precursors used were tri-methyl aluminum and water vapor with respective pulse times of 15 ms and 5 ms, and at a temperature of 255^{o}C. SEM images were taken between 107 cycles at a time.

2.5 Conclusions and Recommendations

Several methods were investigated and characterized in detail to determine their intrinsic limitations. It was determined that EBL held a fundamental advantage over FIB in resolution and reproducibility. Although with the current technology, resolution and arguably control may be greater in TEM, the advantage of several orders of magnitude higher throughput is of greater value to commercializing ENDs.

Several challenges were encountered specific to processing. Native wafer oxidation prior to thin film growth may have caused a thin layer of silicon oxynitride to form on the surface. Other contamination prior to resist deposition would cause nonuniform resist profiles. To stream line processing, these and other issues were addressed by developing a 'clean room checklist' protocol. These recommendations were found to reduce the risks of a sample being compromised in the cleanroom facility and were found to be critical to ultimately achieving successful fabrication.

Prior to any processing, the wafers were subjected to a dilute solution of hydrofluoric acid (HF) or buffered oxide etch (BOE) to remove any native silicon oxide that may have been present on the surface. Prior to growth of LPCVD silicon nitride, the history of use of the tube was evaluated. If the chamber was recently used to deposit another material, a 'dry run' was performed with no wafers to coat the surface and reduce cross contamination. Contamination was found to be one source of defective films. The rubber seal was found to disintegrate often due to the high temperature of the process and needed to be replaced often. If a leak occurred during processing, the quality of the film was often compromised as well.

Prior to EBL, the wafer was cleaned by spraying with acetone, methanol, and isopropanol respectively to remove organic contaminants. A nitrogen gun was used to clear the surface of dust particles. Before spin coating a wafer, the spinner was cleaned with acetone and the vacuum checked. A test wafer was put through a spin cycle to test the machine. Process parameters in every pre-programmed recipe were double checked prior to running. The calibration curve of each spinner was checked often. The etch selectivity of the ICP was checked monthly. The gas flows and power during processing were monitored during the process.

Contact profilometry was used to calibrate the etch rate during the backside wet etch. To confirm that the devices were etched to completion following the wet etch, the wafer was held up to the light. If the silicon nitride films were in fact free standing or if the films were broken, light could be visually observed to shine through them. The samples were dried in a convection oven and never nitrogen sprayed following the backside wet etch.

Optimization of the wet etch was an empirically derived method in which etchant solution, concentration, temperature, agitation, use of alcohol, and handling were all parameters that were investigated, but once a high survival rate was achieved, further modifications were not made to the process. It is unclear, for example, if a TMAH etch with IPA would give a comparable result. This may be a noteworthy undertaking as TMAH is a cheaper alternative, less toxic, and more compatible with CMOS processing. The highest survival rate of free standing films on a wafer following these optimizations was 96%.

During process optimization, the size limits of FIB were explored to produce nanoscale pores but the resolution limit was found to be just over 100 nm. This was too large and not very reproducible in subsequent experiments. The geometry of pores experienced distortions at smaller sizes (close to 100 nm). Other fabrication methods eliminated use of FIB and replaced it with EBL. The order of the steps was also modified to accommodate EBL very early on and prior to the backside wet etch. The final result reduced the number of lithographic steps and provided a feasible template for characterization, i.e to deposit the membrane, characterize it, perform EBL, measure the pore size distribution, perform the backside alignment and wet etch, and finally measure the final pore size distribution and surviving film statistics.

CHAPTER 3

ELECTRON BEAM LITHOGRAPHY OF NANOPORES

In recent decades, electron beam lithography (EBL) has become a well characterized technology for producing arrays of nanoscale features on a wafer. The method has the benefit of patterning using the infinitesimal size of electrons at high energy. Although this is a shared benefit with TEM, EBL has several advantages over TEM. First, it is fully wafer scalable and programmable via software, allowing full automation of the write process. Second, the sample does not need to be backside etched for transparency prior to patterning. Finally, the EBL can pattern multiple features at very precise locations relative to one another across an entire wafer. These features are not limited in size or shape. Micro-scale features can be printed for calibration, alignment, and mapping of the wafer and different size nanopores can be printed for different size biomolecule sensing.

There are also intrinsic challenges associated with EBL techniques. First, an EBL system is costly to install and maintain. Second, the nature of the process is that the film is not patterned directly, but instead a polymeric material is coated on the surface and this material is patterned. Subsequently the pattern is transferred to the membrane underneath by an etch step. Therefore, *to obtain the highest quality pores it was necessary to characterize and optimize both the initial patterning of the electron beam resist, as well as the pores once they were etched to the silicon nitride film.* Another challenge in implementing EBL to produce nanopores is that the resolution obtainable is nearly an order of magnitude coarser than afforded by highly focused TEM beams. This is due to the forward scattering of electrons in the resist which causes an effective broadening of the exposure area. This issue was addressed by using atomic layer deposition to fill in the

pores following EBL. This is discussed in detail in Chapter 5. The objectives here are to demonstrate reproducible arrays of pores of different sizes in the nanometer range; to analyze pore size dependency on dose, film thickness, resist thickness, and position on the wafer; and to optimize these parameters to demonstrate the smallest nanopore possible.

3.1 Nanopore Size Reduction in ZEP

Zeon ZEP-520A was the electron beam resist chosen for EBL because of its high resolution and high etch resistance. Details of the ZEP chemistry will be discussed in the next chapter, wherein the specific reactions during electron beam exposure are discussed as well. Reports in the literature indicated line widths of 10 nm were achieved [49]. It is common to examine line widths as a measure of resolution in lithography including EBL. In the case of ENDs, the features are circular pores and lack one dimension compared to a line. This causes them to be patterned and etched differently. The patterning of a line with electrons causes every point along that line to receive an additional dose due to backscattered electrons from the beam's previous positions. A pore does not experience this compounding effect if dosed by a single shot of the beam. Furthermore, the material in a pore that is etched by a plasma has one less dimension to move in to escape once it is removed from the bulk material compared to a line. This causes a slower etch rate for pores compared to lines. Thus, it was necessary to produce a pattern of pores dosed with different energies across each wafer to gain insight into the dosing, etch depth and profile of pores using ZEP.

The first step to this end was to develop a calibration curve for the size of features relative to the resist thickness, film thickness, and dose. The pores were patterned using two methods of dosing. In the first, a single shot of the beam was applied at very high doses. In the second, multiple shots of the beam were applied at significantly lower

doses. Comparable pore sizes were achieved with both methods. A single silicon wafer underwent three trials in which every parameter was kept constant except for the electron dose. The pores were patterned by a single shot of the beam at a current of 2 nA. The resist used was ZEP diluted 2:1 in anisole (ZEP2:1) and coated at 3000 rpm to give a thickness of about 100 nm. In each trial, the array of pores was split into three regions, each of which received a different dose. Fifteen pores were viewed in SEM after patterning (five per dose) to obtain the size distribution. At the end of each trial, the wafer was immersed in a stripping solution for 15 minutes, and washed with acetone, methanol, and isopropanol before being patterned again. The effects of electron dose on pore size are given in Figure 3. As clearly demonstrated by the Figure, one can precisely pattern the initial pore size in the 10-50 nm range by varying the electron dose. The low statistical fluctuation in the patterned pore dimensions (indicated by the error bars in Figure 3.1) validates the use of EBL as an excellent first step for nanopore array fabrication.

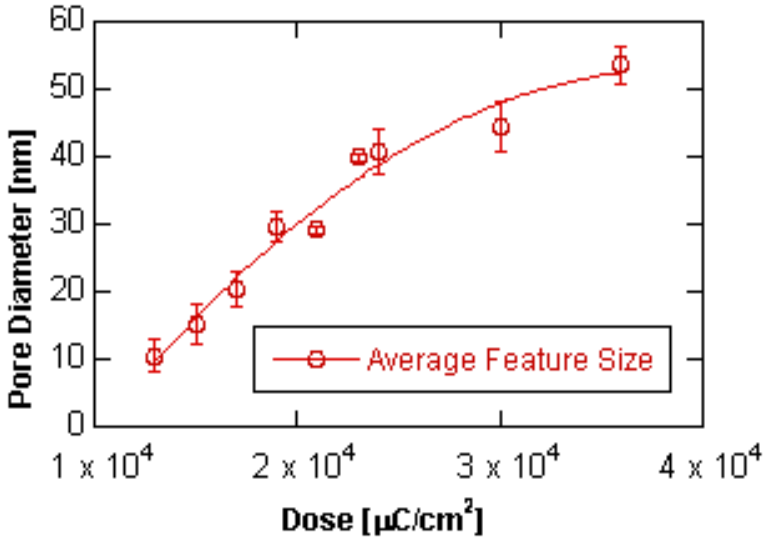

Figure 3.1 Average pore size as a function of dose in 100 nm ZEP 2:1 after development. The curves are only a guide to the eye.

The smallest nanopore produced was 8 nm in diameter. The pores observed in SEM demonstrated high contrast with well defined edges and circular geometry, even as the pore size was reduced to 10 nm and smaller. Several of these pores are shown in Figure 3.2. Nanopore size was measured manually using measurement bars in SmartTiff. The bars were placed tangent to the edges of the black circles.

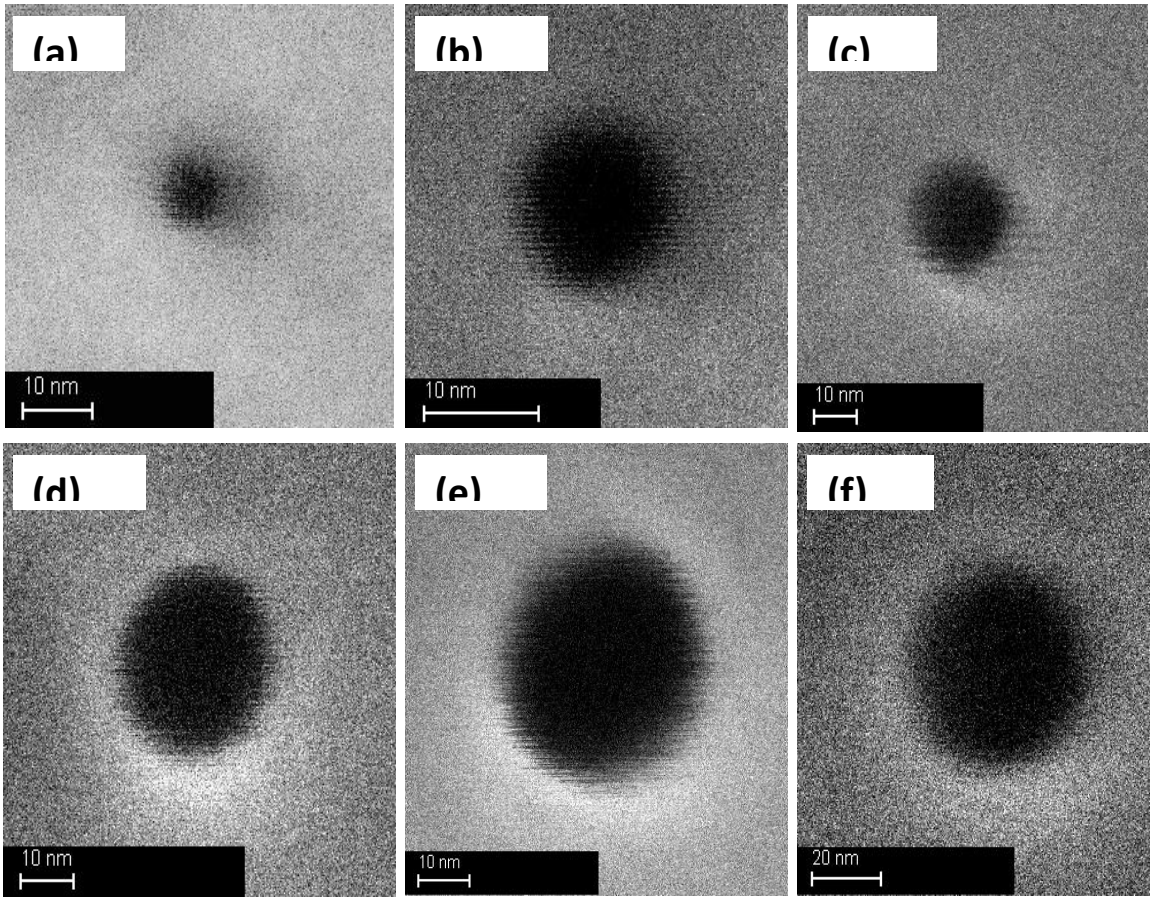

Figure 3.2 High-resolution SEM images of nanopores of varying sizes patterned in 100 nm thick ZEP2:1 resist films at different doses. From (a)-(f): pore sizes of 8, 10, 20, 30, 40, and 50 nm (see Figure 3 for corresponding electron doses).

3.2 Pattern Transfer of Nanopores to Silicon Nitride

In the next set of experiments, four wafers underwent EBL and pattern transfer to the silicon nitride, followed by resist removal. The process parameters examined include film and resist thickness, dose, shot pitch, and the pore pattern. The pore pattern was a 50 nm circle divided into multiple shots with a shot pitch of 5 nm. Because the pattern was divided into multiple shots, the dose required for each shot was much lower than the pores patterned by a single shot. The first wafer was coated with 22 ± 5 nm silicon nitride, then coated with 130 nm ZEP2:1, and patterned with a constant dose of 500 $\mu C/cm^2$ across the entire array of pores. Nineteen pores were imaged across the wafer after resist development and after pattern transfer to the silicon nitride. The pore size distribution was found to be a function of the radial distance from the center of the wafer as shown in Figure 5. This is a controllable phenomenon, which results from the variations in resist thickness during spin coating. It is suggested that the plot in Figure 3.3 qualitatively reflects the thickness profile of the spin-coated resist. The degree of variation is significant, and therefore the eventual manufacturing process for nanopores arrays should incorporate a radially-varying dose profile in the patterning step , or tuning the spin-coating process to give a more uniform ZEP film. The pore size was also found to shrink by an average of 7% after pattern transfer. This is due to the slight tapering of trenches etched by the ICP.

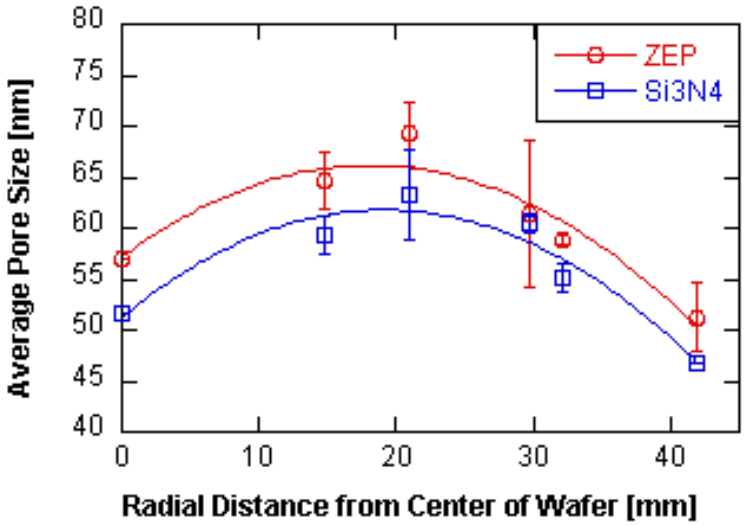

Figure 3.3 Patterned nanopore size as a function of radial distance on the wafer before and after pattern transfer. The curves are only a guide to the eye.

Next, two wafers underwent identical processes to demonstrate reproducibility. Both wafers were coated with 12 ± 4 nm silicon nitride, then coated with 120 nm ZEP2:1, and patterned with 30 nm circles in three dosing regions. The size distributions are given in Figure 3.4. The pore sizes produced on each wafer are very similar and follow the same trends as a function of electron dose. The somewhat larger standard deviations are most likely due to the dependence of dose on position (see Figure 3.3). For example, the electron dose of 900 μm/cm^2 was delivered to pores that covered the largest span of radii on the wafer, and therefore would be expected to have the greatest variance in size, and thus the highest standard deviation. These effects appear to average out to give a mostly unbiased electron dose dependence of the patterned pore size.

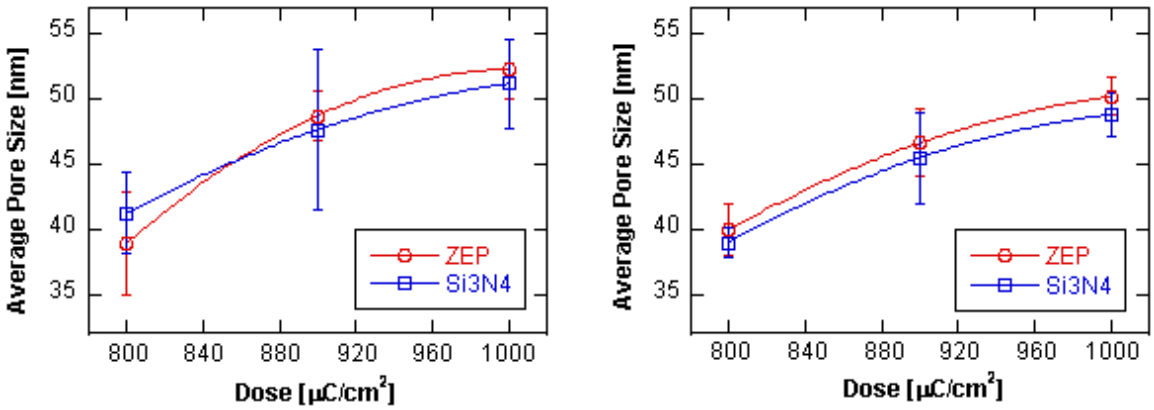

Figure 3.4 Pore size as a function of dose for two wafers after identical processing. The curves are only a guide to the eye.

The fourth wafer was deposited with 19 ± 3 nm silicon nitride and coated with 100 nm ZEP2:1. The pores were patterned using a single shot in three dosing regions. This result is shown in Figure 3.5. Again, a highly reproducible and tunable pore size was obtained upon variation of the electron dose.

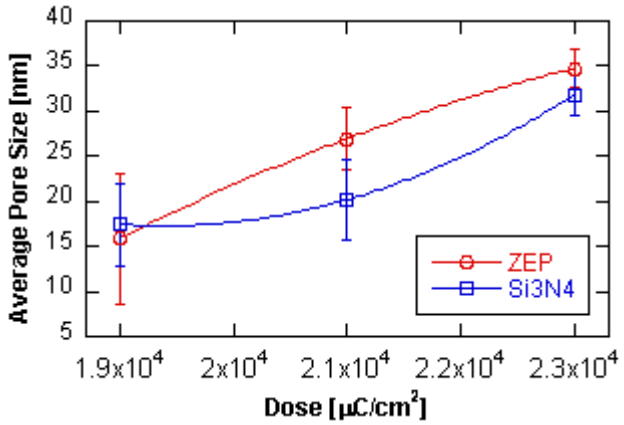

Figure 3.5 Pore size as a function of dose before and after pattern transfer for single shot dosing. The curves are only a guide to the eye.

The smallest pore size produced in silicon nitride was about 15 nm. SEM images of the different size pores are shown in Figure 3.6. The pores have high contrast under the imaging electron beam, and demonstrate good transfer of the circular geometry. It was

found that EBL patterning using a single shot yields the smallest pores with the best geometrical characteristics.

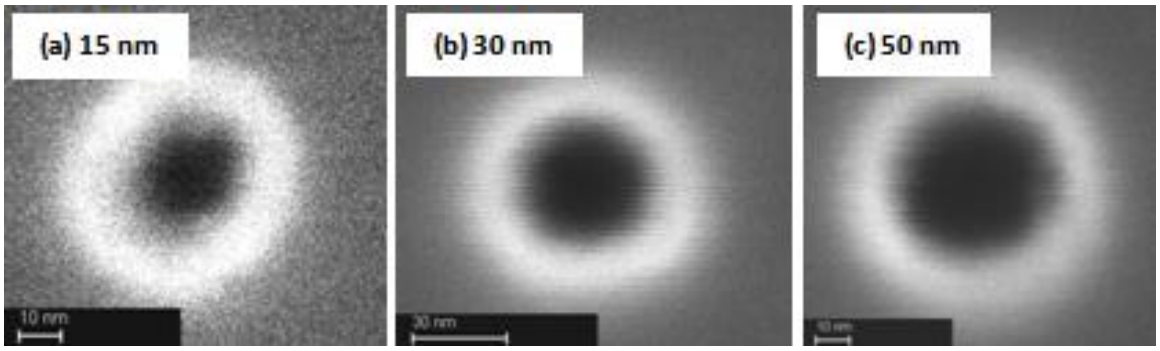

Figure 3.6 Nanopores of various diameters in silicon nitride, (a) and (b) in 16 nm film, and (c) in 7 nm film.

3.3 AFM Topography of Nanopores

Tapping mode atomic force microscopy was performed on a wafer containing 50-70 nm pores in a 16 ± 1 nm silicon nitride film. The AFM probe was composed of silicon, and had a tip curvature of ~8 nm with a tip cone angle of 30^{o}. The 1-D profile of a typical pore is shown in Figure 3.7. The depth reached by the tip indicates that not only has the pore been etched to the underlying silicon wafer, but also that it was over-etched to a significant depth in the silicon itself. This indicates that the etchant molecules are still able to effectively remove material in these nanoscale trenches, and therefore there is room to produce even smaller pores. The measurement bars are placed at a depth of 16 nm, where they are measured to be 66 nm apart for the example shown in Figure 3.7. This strongly supports the SEM data. The tapered shape of the profile is an artifact mirroring the shape and size of the tip of the AFM probe. Still, the smallest lateral

distance measured is 6.5 nm, suggesting that the actual profile comes to an even sharper peak in the sub-5 nm range.

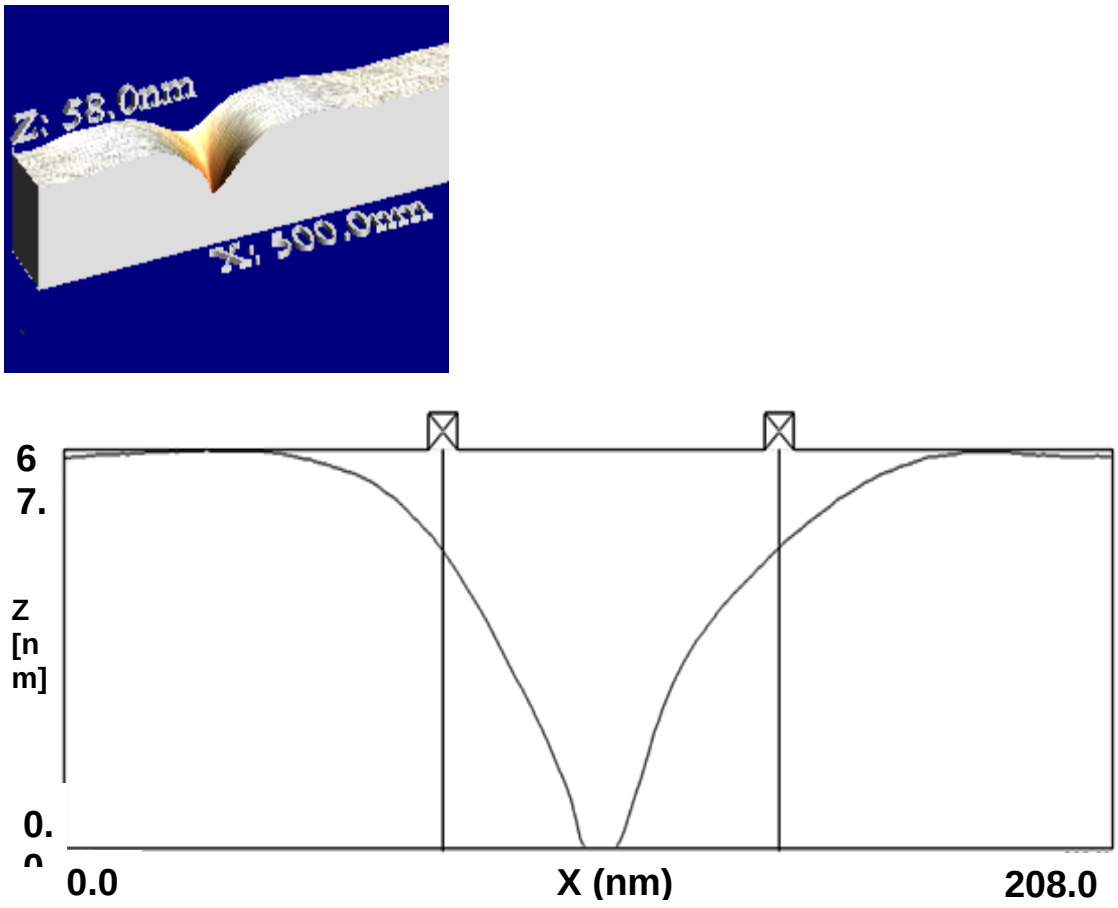

Figure 3.7. AFM depth profile (left), and the profile cross-section (right), of a 50-60 nm pore in 16 nm thin silicon nitride film.

3.4 END Pores

The pores discussed above were surrounded by other features and therefore these pores do not fully represent the devices to be used in END experiments. In this section, results are discussed from measurements on the isolated pores on the wafer, which are referred to as 'END pores'. These pores were much more difficult to locate than pores

with surround features. Therefore, on most wafers, a relatively small number of END pores (5-10) were characterized. However, a single wafer was processed with larger pores of nearly 100 nm in size in order to effectively locate and characterize several END pores which received three different doses. Several of these pores were imaged by SEM prior to and following the backside wet etch, and also compared to the pores with surrounding features. The size distribution of these pores is the most accurate description of all the pores on the wafer and is demonstrated in Figure 3.8.

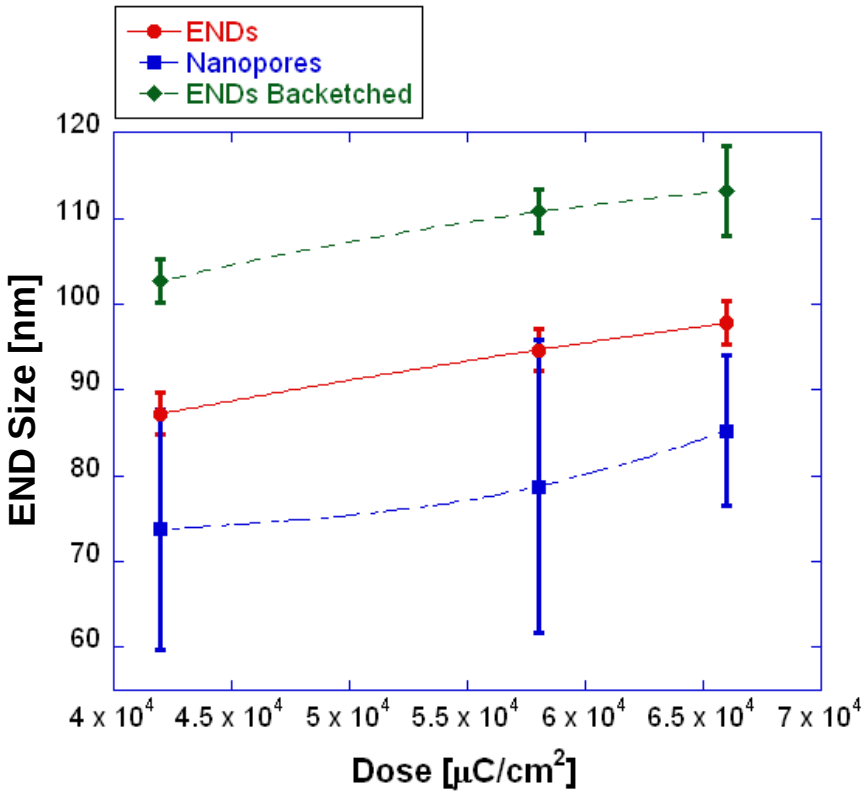

Figure 3.8. Pore size as a function of dose for 18 or more devices across a wafer in a 20 nm silicon nitride film. 'Nanopores' indicate pores surrounded by other features and 'ENDs' indicate isolated pores prior to the backside wet etch. The curves are a guide to the eye.

There are some interesting phenomena observed in Figure 3.8. First, the isolated pores have a much lower standard deviation than the pores with features surrounding them. This may be related to the extremely high dose applied in a single shot of the beam. Essentially, the dose of the entire pore is derived from proximity effect dosing from the single shot, and this is compounded with the proximity effect dosing of the surrounding features. Both sources follow complex Gaussian-based diffusion profiles of electrons which intersect to give regions of augmented or reduced exposure. The extent of this effect at this high dose may have caused this wide range of pore sizes. This type of behavior was not experienced for pores 50 nm or smaller.

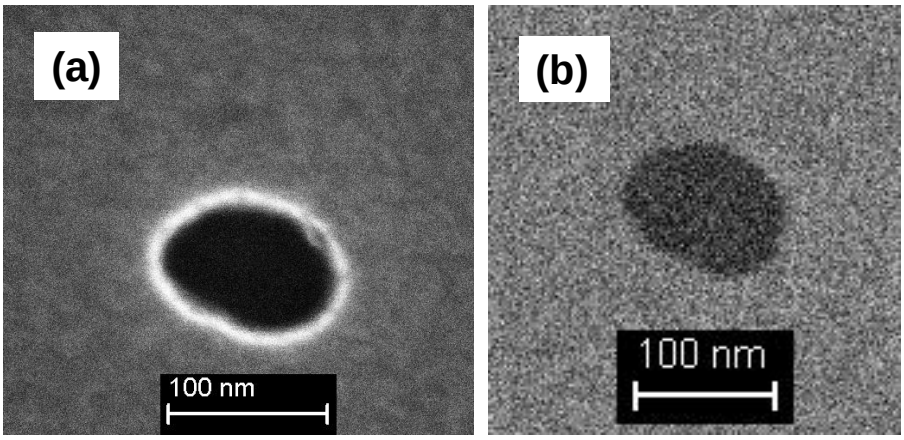

Figure 3.9. (a) An END pore in 20 nm silicon nitride on silicon and (b) An END pore in 20 nm silicon nitride following KOH backside wet etch.

Another important observation is the apparent enlargement of the ENDs following backside wet etch. The reason for the apparent change in size may be revealed in the SEM data. Figure 3.9 shows (a) a nanopore prior to, and (b) a nanopore after, the backside wet etch (not the same pore). A bright ring is observed around the nanopores prior to the backetch. Tetrafluoromethane, which is used to etch the silicon nitride, can also deposit on the sidewalls by forming CF* radicals in the plasma. This effect has been documented for etching of silicon [50, 51]. Passivation and redeposition of etched

material is more likely to occur when flux near the etch surface is constricted. In this case, we were at an aspect ratio greater than 1 (160 nm of ZEP to 100 nm pore) and etching a zero dimensional feature. If a polymeric passivation layer was formed on the sidewall of the pore, then it would have dissolved in the KOH solution, explaining the apparent expansion of the pore as well as the disappearance of the bright ring surrounding the pore.

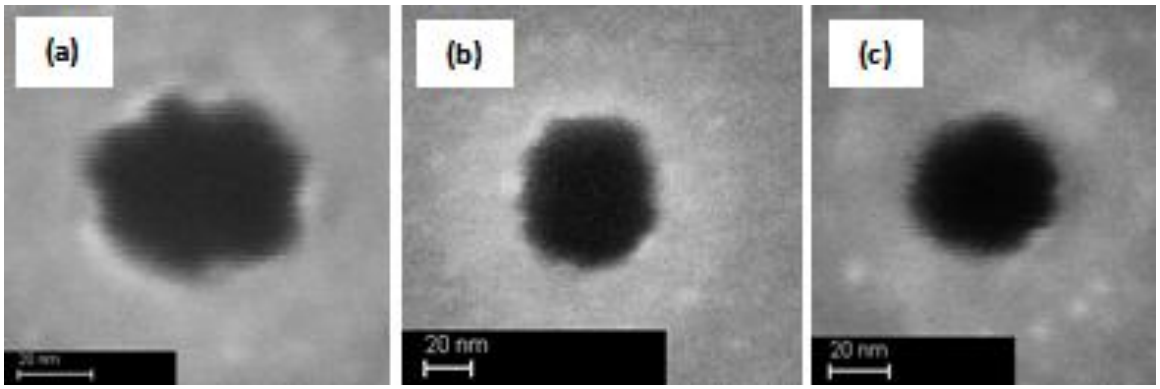

Figure 3.10. Three isolated pores unmarked by calibration features showing the types of imperfections that can occur during processing. (a)-(b): jagged pores created by unoptimized doses in 7 nm and 16 nm silicon nitride; and (c) good-quality circular pore created by optimized dose in 7 nm silicon nitride.

Although a large number of isolated pores were not located on every wafer, approximately 5-10 pores were located and characterized by SEM on several wafers with smaller pores. Three of these END pores are shown in Figure 3.10. There appear to be two kinds of occasional imperfections (Figure 3.10a-b) that occur in these isolated features. The first is a wave-like roughness at the edges of the pore. The second is an apparent elongation of the circular shape in the lateral direction, resulting in an elliptical pore. These effects are due to non-ideal dosing of the resist during EBL. They did not generally occur in pores surrounded by calibration features because of a proximity effect

(these pores receive an added dose that is symmetrical about the pore, resulting in a more circular geometry). To minimize such defects, the dose should be optimized for a given resist thickness. Figure 3.10c shows the result from a properly dosed isolated 50 nm pore.

3.5 Conclusions

EBL has demonstrated wafer scale production of pores in the nanometer range with high reproducibility, and the ability to pattern arrays of features of different sizes. It surpassed the resolution of FIB by an order of magnitude, and exhibited a greater degree of control. A single shot of the beam was identified to yield pores in the sub-10 nm range which approaches the applications of DNA analysis. As film thickness is reduced smaller resolutions are even possible. For thinner films of silicon nitride, larger pores were patterned at the same dose, which qualitatively indicated a more pronounced backscattering effect in silicon with respect to silicon nitride. Therefore, dose optimizations were required for each film thickness.

END pores were generally consistent with statistical data from the pores surrounded by other features. It was found that at lower doses, the feature quality benefitted from proximity effect of the surrounding features, but at higher doses the proximity effect combined with single shot dosing at high energy caused a sporadic pore size distribution. Pore size distribution of several ENDs across a wafer reinforced the claim of high yield and reproducibility.

ZEP imaging in SEM caused some physical deformation and reaction which transferred to the silicon nitride following etching. Therefore, once dose calibration was performed on one wafer, the subsequent wafers were generally not exposed to SEM until after the pattern transfer to the silicon nitride. This effect is probably due to swelling of

the ZEP in SEM [52]. Another challenge was that passivation was believed to occur during the ICP etch step, causing the pores to enlarge following the backside wet etch. This was supported by SEM data.

Characterization was achieved by a combination of SEM and AFM, which are both methods that can be applied to an entire wafer. This demonstrates how TEM can be ultimately removed from the characterization, as it is not conducive to imaging wafers. Pores were etched completely through the film, and tapering resulting from ICP etch was observed in the internal pore structure by AFM. However, because this profile is only accurate near the mouth of the pore given the tip size used, for larger aspect ratios of film thickness to pore size it would certainly be useful to perform TEM as an identifier of the smallest internal pore diameter. Another alternative would be an AFM scan with a carbon nanotube tip which can achieve the truly nanoscale resolution necessary to profile ENDs.

The empirical characterizations of EBL described here provide a baseline set of parameters to reproduce arrays of pores reported for the substrates described. Ultimately, these are observations drawn from experiment and therefore are limited in scope. The mechanisms behind the optimization of dose and feature size/geometry are qualitatively inferred but the data cannot be extrapolated to a different combination of substrate and applied dose. Relationships between dose and pore geometry are reported for a specified resist thickness, substrate, and dosing pattern. Consequently, it would be of great merit to develop a complimentary theoretical model which can predict pore size/geometry based on any configuration of these parameters. Such a model could be used as an optimization engine for future tuning of END fabrication.

There also remain questions as to the source of the apparent bowl shaped pore geometry of pores in ZEP from SEM, the effect of different substrates, and the apparent

limit of 10 nm in reproducible feature size. To address these issues, it is necessary to analyze the fundamental underlying mechanisms of EBL. In the next chapter, the electron scattering in the substrate and resulting energy distributions are carefully examined in the context of these points.

CHAPTER 4

MODELING ELECTRON BEAM LITHOGRAPHY OF NANOPORES

In Chapter 3, EBL was studied experimentally with the intent of producing and characterizing nanopores with diameters less than 100 nm in a reproducible manner. The study revealed strong correlations between dose and pore geometry as well as qualitative insights into the fabrication process. Nonetheless, there are a number of issues that cannot be addressed only through experimentation. For example, the smallest pores obtained with good reproducibility were of size 10 nm (Figures 3.1, 3.2). It is unclear whether this apparent lower bound is a fundamental physical restraint or the result of an empirical limitation. In addition, all the pores observed in SEM appeared to have a tapering internal structure, the exact morphology of which could not be imaged accurately. The source of this observed effect possibly lies in the electron scattering behavior. On the other hand, the pore morphology is of critical importance to the eventual function of ENDs. Another interesting observation was that pores produced in ZEP on silicon nitride appeared measurably smaller than pores in ZEP on silicon at the same dose (Figures 3.1, 3.5). These pores were produced under identical conditions of development and etching, which may indicate that the source of the discrepancy arises from different electron scattering behavior in silicon and silicon nitride.

The objective of this chapter is to address such questions in the context of a physical model of the EBL process. In particular, the approach taken consists of the following steps. First, the electron energy distributions in the substrate are calculated. These distributions are then used to simulate the pore geometry for a broad range of process parameters, including the dose, shot pattern, beam blur, and substrate. This capability allows evaluation and explanation of the experimental results obtained in Chapter 3, and makes possible a predictive “design” capability for END fabrication. We

also use our model to study the effects and importance of secondary electron emission, which may also play a role in determine the nanopore morphology.

4.1 Electron Scattering Model Assumptions

Prior to studying electron scattering behavior, it is important to note some key considerations as determined from literature and through the experiments described in Chapter 3. First, the primary difference between exposing single and multiple shots is that single-shot dosing relies to a greater extent on backscattered electrons whereas multiple shot dosing relies more on forward scattered electrons to produce the same nominal pore size [53]. This concept is illustrated in Figure 4.1. In addition, since forward scattering characteristically occurs at smaller angles than backscattering, the geometry of a single shot pore is hypothesized to "taper" to a lesser degree than a pore patterned with multiple shots.

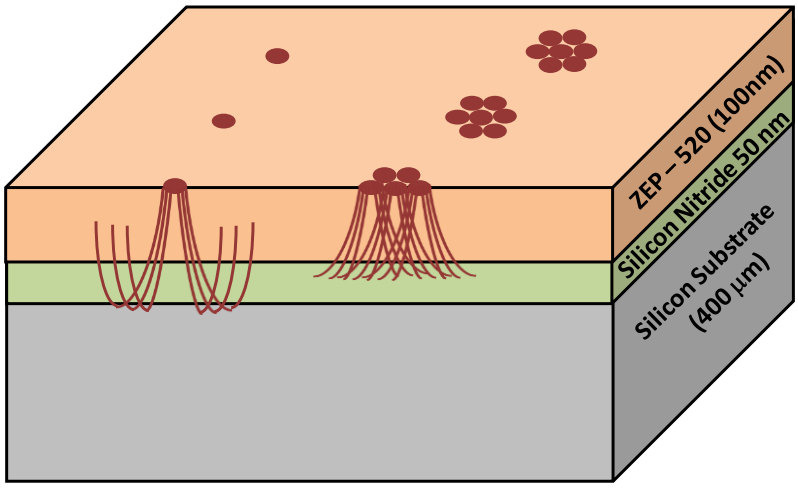

Figure 4.1. Schematic of electron scattering profile in higher energy single shot (left) vs lower energy multiple shots (right).

Another important consideration is the role of the "proximity effect". The distance between adjacent devices is 2.47 mm, well outside the range of the proximity effect.

However, when experimentally determining pore size distributions by statistical SEM measurements from a collection of pores, the pores were usually surrounded by rectangular features about 500 nm away on all four sides, which were used as an aid locating the pores on the substrate. These pores could experience some proximity effects; however, our SEM images demonstrate that they were very close in size (at the pore mouth) to isolated pores. Therefore, we assume that proximity effects are negligible, and we use the above size distributions to determine the EBL operating conditions in the simulations. Furthermore, we will only simulate isolated pores (actual ENDs), which are spaced with a high enough pitch (2.47 mm) to safely disregard any proximity effects [54].

The symmetry intrinsic to ENDs allows certain simplifying assumptions especially in the case of the single shot model. For example, the energy distribution of a single shot (in cylindrical coordinates) clearly depends on radial distance r and depth z in the film, but can be modeled independently of the sweep angle θ due to the angular symmetry. This is a very reasonable assumption which drastically reduces simulation time. From the experiments we find that pores as small as 8 nm were achieved in ZEP, which is smaller than most resolvable line widths that have been reported in literature [55]. This may stem from the fact that lines inherently consist of multiple shots and as well as a contribution of nearby shots from adjacent lines. The proximity effects are significant and limiting, but this is not a restriction for the present case wherein pores, and not lines, are being produced.

ZEP is well known to behave differently under different development conditions, specifically marked by changes in resist sensitivity [56, 57]. In designing the simulations, I assign the dose sensitivity in part by comparison to experimental data reported in Chapter 3. Because the development conditions were identical for every wafer, this factor

is then eliminated as a variable. In summary, the following assumptions were made in simulating the internal pore geometry:

1. The electron energy distribution and subsequent pore geometry is angularly symmetric.

2. The pore geometry depends primarily on the energy deposition profile in the resist due to electron scattering in the film.
3. The proximity effect is negligible due to the high pitch between ENDs. Only the internal geometry of isolated pores are of interest.

4. The etch rate in ICP is uniform and only occurs in the z direction.

5. Experimental pores surrounded by boxes were comparable in size to isolated pores, allowing a reasonable basis for comparing simulated to experimental pore size distributions.

4.2 Physics of Electron Scattering Model

In modeling electron scattering behavior, it is assumed that the atoms in the substrate are distributed randomly and with uniform density. The composition of the medium is determined by the stoichiometry. It follows that the molecular weight of the material can be determined by

$$A_m = \sum n_i A_i \tag{4.1}$$

where A_i is the atomic weight of the *i*th element and n_i are the stoichiometric indices. The number of molecules per unit volume can then determined by

$$\mathcal{N} = N_A \frac{\rho}{A_m} \tag{4.2}$$

where N_A is Avogadro's number and ρ is the mass density. As an incident electron approaches the substrate with energy E, it will undergo a series of interactions, each of which causes an energy loss W and a change in direction. The change in direction is specified by the polar scattering angle θ and the azimuthal angle ϕ. The type of interaction, energy loss, and flight path per event are determined probabilistically by the molecular differential cross section (DCS). Figure 4.2 below depicts an electron striking an area $d\sigma$ scattered through an angle θ into a solid angle $d\Omega$.

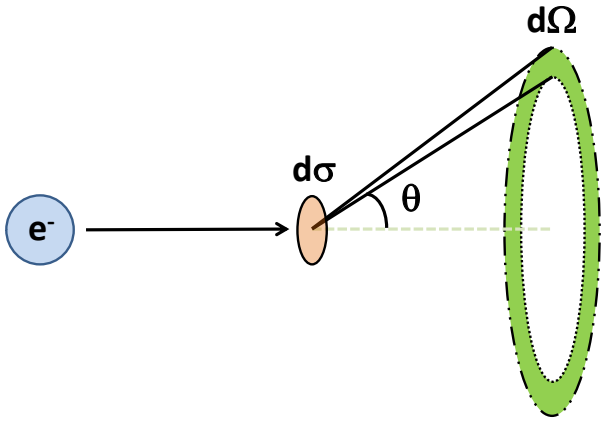

Figure 4.2. Differential cross section of an electron scattering event.

In general, there are two classes of interactions between the electrons and the substrate in during EBL. The first is an elastic scattering event, in which an electron is deflected by a substrate atom but no reaction occurs. This may result when the electron is attracted to a nucleus or repelled by an electron cloud. The path of the electron is slightly modified but there is virtually no energy loss. The second type of electron-substrate interaction is inelastic scattering. In this case, the electron causes an ionization or other reaction within an atom of the target material. Secondary electrons, Auger electrons, X-rays, or phonons may be ejected as a result of the collision. The incident electron is deflected and energy is

lost depending on the type of interaction. Figure 4.3 illustrates elastic and inelastic collisions.

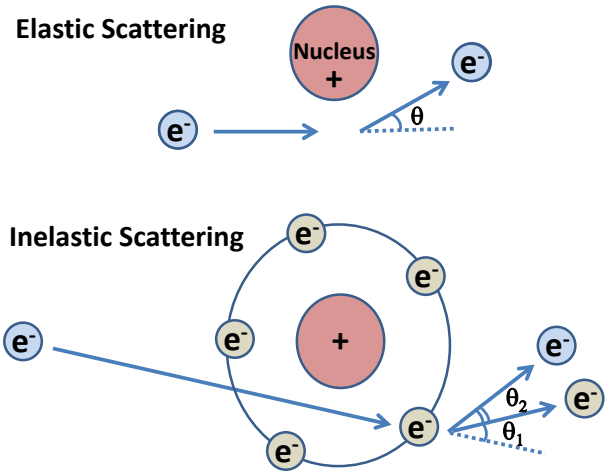

Figure 4.3. Elastic and inelastic electron scattering events in a substrate atom.

A Monte Carlo simulation method was utilized to model the electron scattering. This technique is used to model processes that have a statistical distribution of outcomes. It requires data genesis for a large number of events, wherein each of these events is empirically observed to be unique and seemingly random. When this condition applies, the Monte Carlo method simplifies the complexity of very short-time-scale interactions *via* a probabilistic approach. In electron scattering, one can then use the probabilities of elastic and inelastic collisions combined with random sampling methods to generate each electron trajectory in a statistically valid manner. A statistically significant number of trajectories is computed and normalized to give the energy density per electron.

The Monte Carlo simulation packages Penelope (OECD-NEA) and Sceleton X (GenISys) were used to calculate the PSFs for the electron energy distribution in the films for each case examined. Penelope utilizes more rigorous algorithms which account for secondary electron emissions while Sceleton X does not. Thus, Penelope was used for all data except in the studies of secondary electron effects.

All of the expressions described for Penelope's simulation algorithm were obtained from the Nuclear Energy Agency (NEA) [58]. The elastic and inelastic scattering events, denoted as A and B respectively, were characterized by their differential cross sections defined as

$$\frac{d^2\sigma_A}{dWd\Omega}(E;W,\theta) \tag{4.3}$$

$$\frac{d^2\sigma_B}{dWd\Omega}(E;W,\theta) \tag{4.4}$$

respectively. The expressions are independent of ϕ because the scattering can be assumed to occur symmetrically in the axial direction about the angle of incidence. The total cross sections are then

$$\sigma_{A,B}(E) = \int_0^E dW \int_0^\pi 2\pi sin\theta d\theta \frac{d^2\sigma_{A,B}}{dWd\Omega}(E;W,\theta) \tag{4.5}$$

The probability distribution functions (PDFs) of the energy loss W and polar scattering angle θ are

$$p_{A,B}(E;W,\theta) = \frac{2\pi sin\theta}{\sigma_{A,B}(E)} \frac{d^2\sigma_{A,B}}{dWd\Omega}(E;W,\theta) \tag{4.6}$$

Due to symmetry, the PDF of the azimuthal scattering angle is

$$p(\phi) = \frac{1}{2\pi} \tag{4.7}$$

The total interaction cross section is the sum of the discrete interactions:

$$\sigma_T(E) = \sigma_A(E) + \sigma_B(E) \tag{4.8}$$

The probability distributions of the interactions A and B are respectively

$$p_A = \frac{\sigma_A}{\sigma_T} \tag{4.9}$$

$$p_B = \frac{\sigma_B}{\sigma_T} \tag{4.10}$$

Next, the total mean free path between interactions is inferred from the total cross section and the number of scattering centers.

$$\lambda_T = (\mathcal{N}\sigma_T)^{-1} \tag{4.11}$$

The probability distribution of the free flight displacement is defined as

$$p(s) = \lambda_T^{-1} exp\left(-\frac{s}{\lambda_T}\right) \tag{4.12}$$

Therefore, *s* is generated using the sampling relationship

$$s = -\lambda_T ln\xi \tag{4.13}$$

where ξ is a random number between 0 and 1. After similarly sampling the values of *W*, θ, and ϕ from the probability distribution function in (4.6), the energy is reduced as:

$$E_{n+1} = E_n - W \tag{4.14}$$

The original direction of the electron in the form (u,v,w) is

$$d_n = (sin\vartheta cos\varphi, sin\vartheta sin\varphi, cos\vartheta) \tag{4.15}$$

The components of the new direction following the scattering event is then determined by

$$u' = ucos\theta + \frac{sin\theta}{\sqrt{1-w^2}}[uwcos\phi - vsin\phi] \tag{4.16}$$

$$v' = vcos\theta + \frac{sin\theta}{\sqrt{1-w^2}}[vwcos\phi + usin\phi] \tag{4.17}$$

$$w' = wcos\theta - \sqrt{1-w^2}sin\theta cos\phi \tag{4.18}$$

In soft scattering events (small angle scattering), the angular deflection is produced from the distribution

$$F_a(s;u) = aU_{0,b}(\mu) + (1-a)U_{b,1}(\mu) \tag{4.19}$$

where μ is defined as

$$\mu \equiv \frac{1-cos\theta}{2} \tag{4.20}$$

and the normalized uniform distribution U is

$$U_{u,v}(x) = \begin{cases} {}^{1}/_{(v-u)} & if\ u \le x \le v \\ 0 & otherwise \end{cases} \tag{4.21}$$

The parameters a and b are

$$a = 1 - 2\langle\mu\rangle^{(s)} + b \tag{4.22}$$

$$b = \frac{2\langle\mu\rangle^{(s)} - 3\langle\mu^2\rangle^{(s)}}{1-2\langle\mu\rangle^{(s)}} \tag{4.23}$$

where the mean first and second scattering moments are respectively

$$\langle\mu\rangle^{(s)} = \frac{1}{2}\left[1 - exp\left(-{}^{s}\Big/_{\lambda_{el,1}^{(s)}}\right)\right] \tag{4.24}$$

$$\langle\mu^2\rangle^{(s)} = \langle\mu\rangle^{(s)} - \frac{1}{6}\left[1 - exp\left(-{}^{s}\Big/_{\lambda_{el,2}^{(s)}}\right)\right] \tag{4.25}$$

In hard scattering events, first the type of event is sampled by the probability distribution functions

$$p_{el} = \lambda\mathcal{N}\sigma_{el}^{(h)} \tag{4.26}$$

$$p_{in} = \lambda\mathcal{N}\sigma_{in}^{(h)} \tag{4.27}$$

$$p_{br} = \lambda\mathcal{N}\sigma_{br}^{(h)} \tag{4.28}$$

for the cases of an elastic, inelastic, or Bremsstrahlung event respectively.

The differential cross section for elastic scattering is derived from a modified Wentzel model using an independent atom approximation:

$$\frac{d\sigma_{el}}{d\Omega} = \sum_{i,j} \frac{sin\left({}^{qa_{ij}}/_{\hbar}\right)}{{}^{qa_{ij}}/_{\hbar}} \left[f_i(\theta) f_j^*(\theta) + g_i(\theta) g_j^*(\theta)\right] \tag{4.29}$$

where a_{ij} is the distance between atoms i and j, q is the momentum transfer given by

$$q = 2\hbar k sin\left(\frac{\theta}{2}\right) \tag{4.30}$$

f_i and g_i are the direct and spin-flip scattering amplitudes for the atom i, respectively:

$$f(\theta) = \frac{1}{2ik} \sum_{l=0}^{\infty} \{(l+1)[exp(2i\delta_{l+}) - 1] + l[exp(2i\delta_{l-}) - 1]\} P_l(cos\theta) \tag{4.31}$$

$$g(\theta) = \frac{1}{2ik} \sum_{l=0}^{\infty} \{exp(2i\delta_{l-}) - exp(2i\delta_{l+})\} P_l^1(cos\theta) \tag{4.32}$$

where $P_l(cos\theta)$ are Legendre polynomials, d_{l+} and d_{l-} are the phase shifts, and k is the wave number of the projectile given as

$$k \equiv \frac{p}{\hbar} = \frac{1}{\hbar c} [E(E + 2m_e c^2)]^{1/2} \tag{4.33}$$

The differential cross section for inelastic scattering is derived from a generalized oscillator strength (GOS) model and is divided into distant longitudinal, distant transverse, and close interactions as follows.

$$\frac{d^2\sigma_{in}}{dWdQ} = \frac{d^2\sigma_{dis,l}}{dWdQ} + \frac{d^2\sigma_{dis,t}}{dWdQ} + \frac{d^2\sigma_{clo}}{dWdQ} \tag{4.34}$$

The distant longitudinal DCS is given as

$$\frac{d^2\sigma_{dis,l}}{dWdQ} = \frac{2\pi\epsilon^4}{m_e v^2} \sum_k f_k \frac{1}{W} \frac{2m_e c^2}{Q(Q+2m_e c^2)} \delta(W - W_k) \Theta(W_k - Q) \tag{4.35}$$

The distant transverse DCS is given as

$$\frac{d^2\sigma_{dis,t}}{dWdQ} = \frac{2\pi\ \epsilon^4}{m_e v^2} \sum_k f_k \frac{1}{W} \left\{ln\left(\frac{1}{1-\beta^2}\right) - \beta^2 - \delta_F\right\} \delta(W - W_k) \Theta(W_k - Q_-) \delta(Q - Q_-)$$

(4.36)

where Q_- is the minimum recoil energy for the energy transfer W and δ_F is the Fermi density effect correction on the stopping power given as

$$\delta_F \equiv \frac{1}{Z}\int_0^\infty \frac{df(Q=0,W)}{dW} ln\left(1+\frac{L^2}{W^2}\right) dW - \frac{L^2}{\Omega_p^2}(1-\beta^2) \tag{4.37}$$

where L is a real-valued function of β^2 defined as the positive root of the equation

$$\mathcal{F}(L) \equiv \frac{1}{Z}\Omega_p^2 \int_0^\infty \frac{1}{W^2+L^2}\frac{df(Q=0,W)}{dW} dW = 1-\beta^2 \tag{4.38}$$

The DCS for close collisions is given by

$$\frac{d^2\sigma_{clo}}{dWdQ} = \frac{2\pi\epsilon^4}{m_e v^2}\sum_k f_k \frac{1}{W^2}\left(1+\frac{\beta^2(E-W)W-EW}{E(W+2m_e c^2)}\right)\delta(W-Q)\Theta(W-W_k) \tag{4.39}$$

The DCS for Bremsstrahlung emission is

$$\frac{d\sigma_{br}^{(BH)}}{dW} = r_e^2 \alpha Z(Z+\eta)\frac{1}{W}\left[\epsilon^2\varphi_1(b) + \frac{4}{3}(1-\epsilon)\varphi_2(b)\right] \tag{4.40}$$

where α is the fine-structure constant, r_e is the classical electron radius. ϵ and b are respectively defined as

$$\epsilon = \frac{W}{E+m_e c^2} = \frac{W}{\gamma m_e c^2} \tag{4.41}$$

$$b = \frac{Rm_e c}{h}\frac{1}{2\gamma}\frac{\epsilon}{1-\epsilon} \tag{4.42}$$

Finally,

$$\varphi_1(b) = 4ln\left({Rm_e c}/{\hbar}\right) + 2 - 2ln(1+b^2) - 4b\cdot arctan(b^{-1}) \tag{4.43}$$

and

$$\varphi_2(b) = 4ln\left({Rm_e c}/{\hbar}\right) + \frac{7}{3} - 2ln(1+b^2) - 6b \cdot arctan(b^{-1}) \tag{4.44}$$
$$-b^2[4 - 4b \cdot arctan(b^{-1}) - 3ln(1+b^{-2})]$$

Secondary electrons from inner shells are emitted with energy

$$E_s = W - U_i \tag{4.45}$$

Secondary electrons from outer shells are emitted with energy

$$E_s = W \tag{4.46}$$

The electrons are emitted in the direction of the momentum transfer during the collision. The polar emission angle is

$$cos^2\theta_s = \frac{{W^2}/{\beta^2}}{Q(Q+2m_e c^2)}\left(1 + \frac{Q(Q+2m_e c^2) - W^2}{2W(E+m_e c^2)}\right)^2 \tag{4.47}$$

The azimuthal emission angle is

$$\emptyset_s = \pi + \emptyset \tag{4.48}$$

In Sceleton X, elastic collisions can be described by the screened Rutherford equation [59] given by

$$\frac{d\sigma}{d\mathrm{W}} = \frac{e^4 Z(Z+1)}{m^2 v^4 (1 - cos\theta + 2\alpha)^2} \tag{4.49}$$

wherein σ is the cross section of the interaction, *W* is the electron energy loss, *Z* is the atomic number of the scattering atom, *E* is the energy of the incident electron, θ is the scattering angle, and α is the screening factor given as:

$$\alpha = \frac{1}{4}\left(4.67E^{-1/2}Z^{1/3}\right)^2 \tag{4.50}$$

Inelastic scattering can be modeled as a Bethe Energy Loss using the "continuously slowing down" approximation [60]:

$$\frac{dE}{ds} = -7.75 \times 10^4 \frac{\rho}{EA} ln\left(1.166 \frac{E}{J}\right) keV cm^{-1} \quad (4.51)$$

where s is the distance traveled by the electron along its trajectory, ρ is the density of the substrate, A is atomic number, and J is the mean ionization potential of the substrate atoms. The only required physical parameters of the film are the stoichiometry and mass density.

The substrate is ZEP-520A, a polymer chain with a single bonded carbon backbone and molecular weight of about 55000 g/mol. The repeat unit is shown in Figure 4.4.

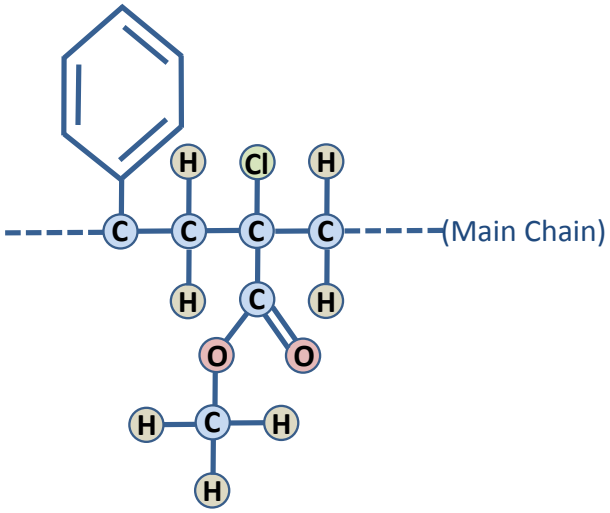

Figure 4.4. Repeat unit of ZEP-520 photoresist obtained from Zeon Corporation.

The chemistry of ZEP is comparable to PMMA, a complementary EBL photoresist which has been studied in greater detail than ZEP [61]. The only chemical difference is that ZEP includes a phenyl group which may increase etch durability and a chlorine atom which may facilitate chain scission [61]. When the polymer chain is

fragmented, the shorter pieces become soluble in the developer. Chain scission of ZEP during EBL is depicted in Figure 4.5.

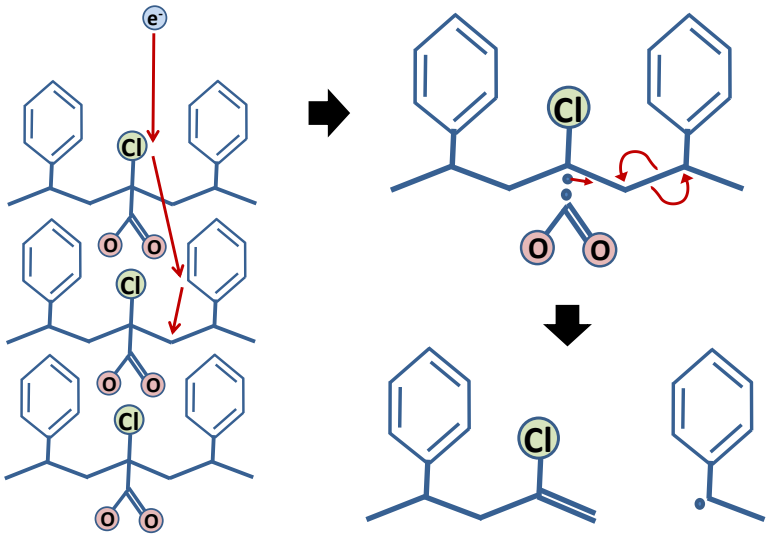

Figure 4.5. A potential pathway for ZEP chain scission during EBL.

Chain fragmentation is usually modeled in the literature based on the energy distribution in the film [29, 62-66]. The latter function is called the point spread function (PSF). The main C-C chain is broken by primary, secondary, and backscattered electrons. Elastic scattering of electrons causes an effectively broader exposure area described probabilistically by equation (4.52) [61].

$$P(z,\rho)\rho d\rho = \frac{3\mathrm{l}}{z^3} exp\left(-\frac{3\mathrm{l}\rho^2}{2z^3}\right)\rho d\rho \tag{4.52}$$

where z is depth, ρ is the lateral coordinate, and λ is the mean free path. Inelastic collisions are responsible for chain scission and secondary electron emission which propagates the process until the incident energy is dissipated. These reactions are modeled by the point spread function of the deposited energy [61] given in equation (4.53).

$$F(z,\rho) = \int_0^\infty f\big(|\rho - \rho_1|, E(z,\rho_1)\big) P(z,\rho_1)\rho_1 d\rho_1 \tag{4.53}$$

4.3 Simulating Single Shot Pore Geometry in ZEP on Silicon

In all of the simulations detailing internal pore structure, the PSFs were calculated in Penelope using the cutoff energy of 0.0000E+00 eV for hard inelastic collisions and 1.0000E+01 eV for hard Bremsstrahlung emissions. Effectively, these cutoff energies are set to count all electrons until their energy has completely decayed. It is important to note that the PSF is the simulated energy distribution for a point source of electrons. The beam in an EBL system is not a point source, but has an effective diameter which can be derived from the measured beam intensity of the tool. The configuration with which the beam strikes the surface is mathematically accounted for by the convolution of the PSF and the beam image function [64].

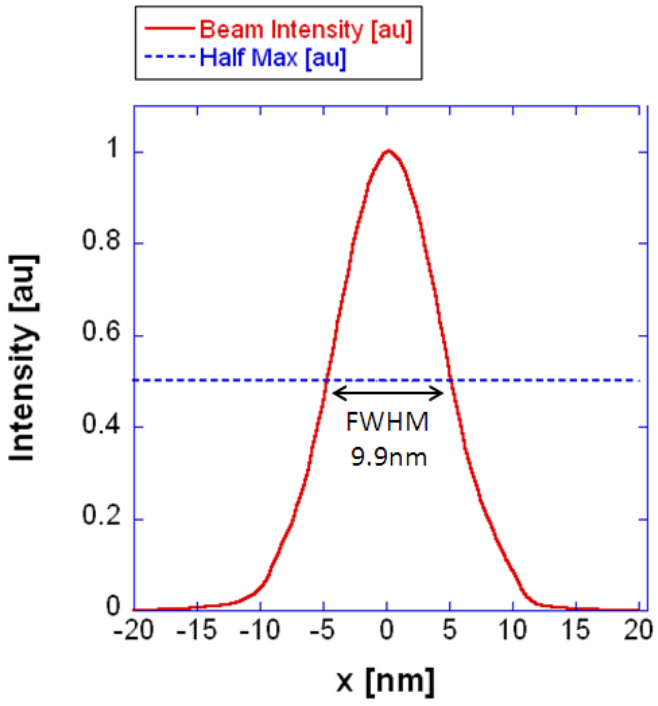

Figure 4.6. Beam image of EBL tool used in experiments. FWHM = Full width half max.

The beam image of the EBL used in the experiments is shown in Figure 4.6. The beam image is nearly radially symmetric and strongly resembles a Gaussian function with a full width at half maximum (FWHM) of 9.9 nm. The beam image is thus modeled as a Gaussian function and, and the FWHM is considered as a characteristic parameter which will subsequently be referred to as 'beam blur'. This Gaussian approximation to the beam image was convolved with the PSFs to produce the energy distributions in the film, using the convolution program Layout Beamer (GenISys).

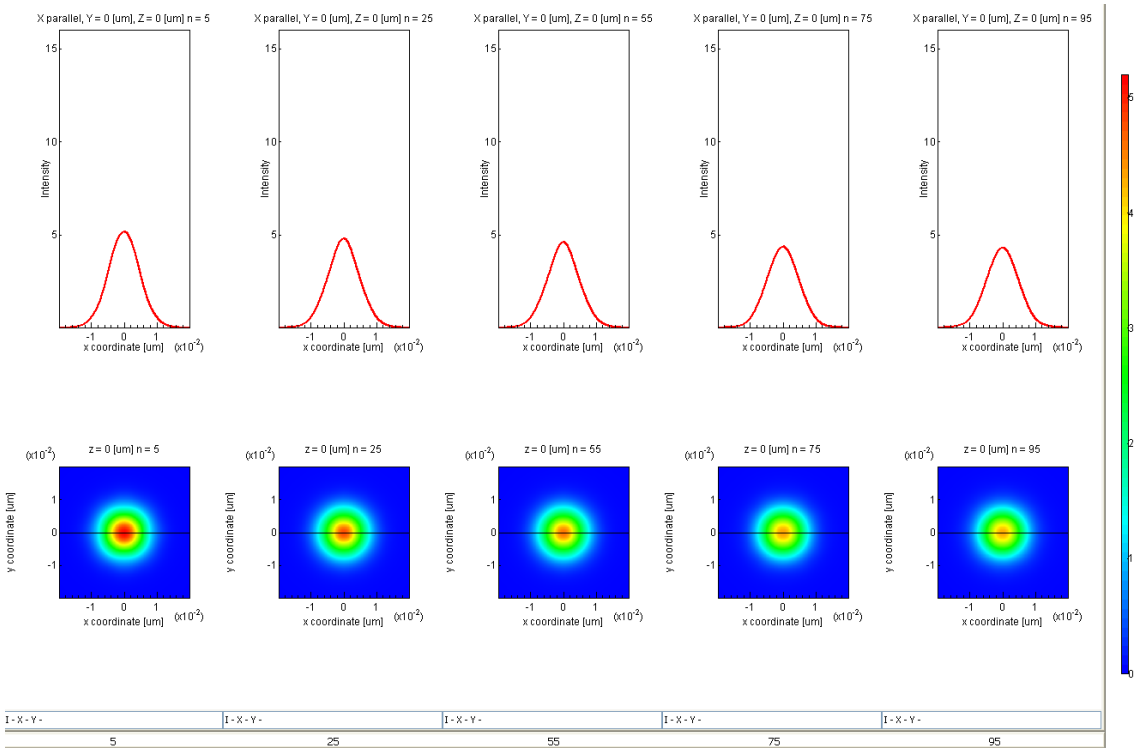

Figure 4.7. Energy distribution in 100 nm ZEP on silicon at depth of 5 nm, 25 nm, 55 nm, 75 nm, and 95 nm in the film from left to right, respectively. The dose received was 13000 $\mu C/cm^2$.

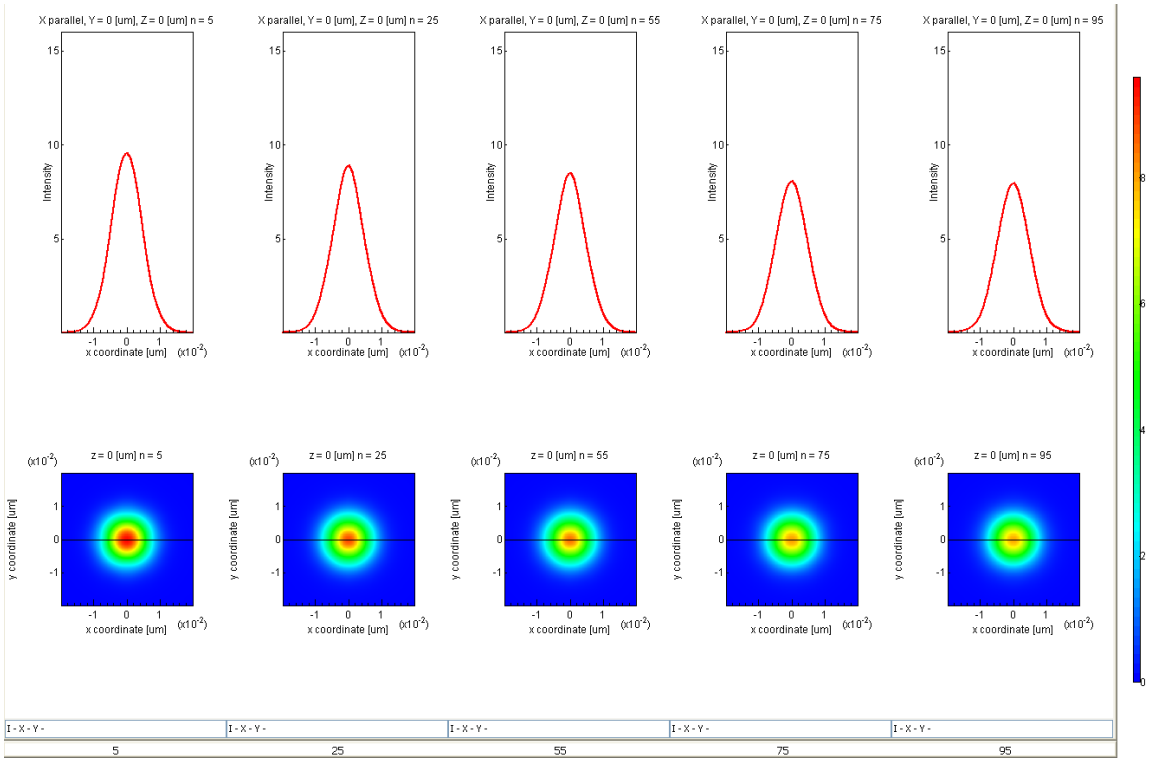

Figure 4.8. Energy distribution in 100 nm ZEP on silicon at depth of 5 nm, 25 nm, 55 nm, 75 nm, and 95 nm in the film from left to right, respectively. The dose received was 24000 $\mu C/cm^2$.

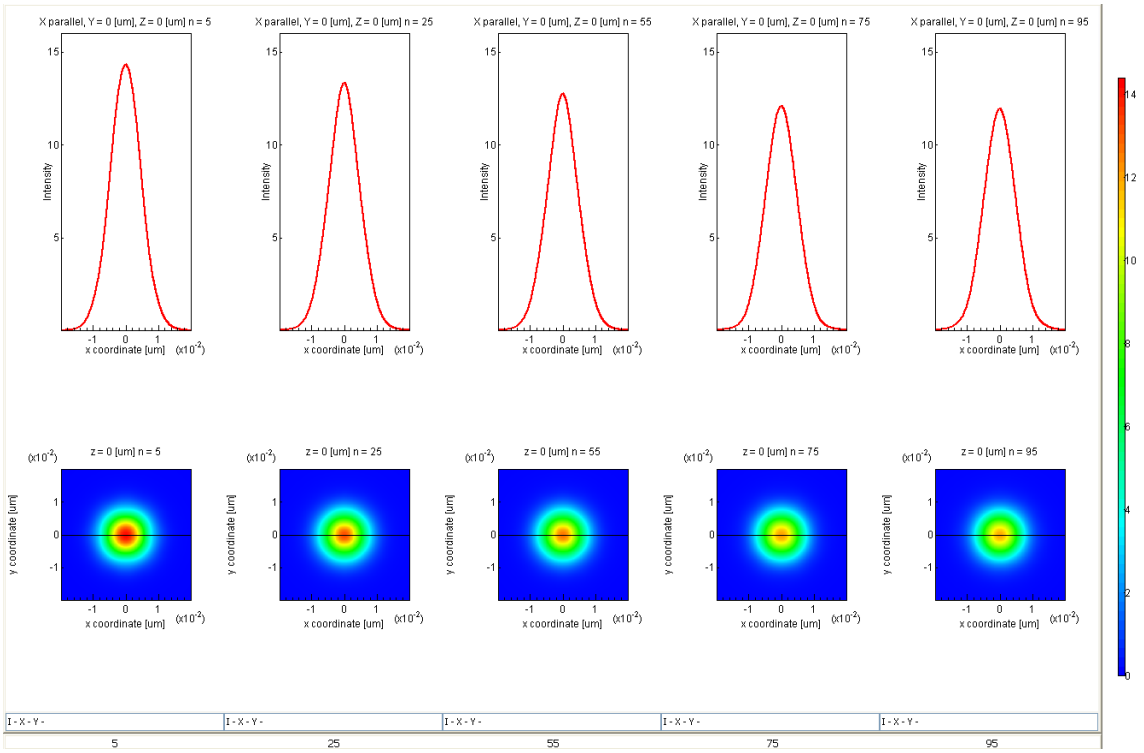

Figure 4.9. Energy distribution in 100 nm ZEP on silicon at depth of 5 nm, 25 nm, 55 nm, 75 nm, and 95 nm in the film from left to right, respectively. The dose received was 36000 $\mu C/cm^2$.

Figures 4.7-4.9 demonstrate the energy distributions throughout a 100 nm ZEP film on silicon at different doses. First, the results confirm the direct dependence of energy distribution on the dose. In addition, the figures indicate a strong dependence of deposited energy on depth in the resist. The deposited energy appears to generally decrease into the resist. We therefore expect the pores to taper down to a smaller size at the bottom than at the top.

Once these energy distributions were determined, it was necessary to calculate the threshold energy which would cause resist development. This was initially attempted by iteratively modulating the threshold energy to match the simulated pore sizes at the top of the films to the SEM data in Figure 3.1. However, iterating the threshold energy alone

was found to be insufficient in modeling the expected pore sizes. The dose dependence of the experimental pore size suggested that the process was operating at a higher beam blur than suggested by the beam image. In fact, to match the simulated pore sizes to experiment, it was necessary to increase the beam blur by a factor of 3-4. This result suggests that the beam image is just one source of an effective Gaussian broadening of the beam in the resist. A review of the literature reveals that it is not uncommon to experience a larger effective "average process blur" due to several overlapping effects. For example, stochastic Coulomb interactions imply that the beam blur is not constant [67, 68]. Fluctuations in the incident beam due to spatial and temporal variance, sometimes referred to as shot noise, create a spatial variance in the incident dose [69, 70]. Moreover, height mapping offsets in the focus of the beam during operation can result in effective blurring [67]. Non-uniformities in the photoresist can further amplify this effect. In addition, beam deflection in the subfield has been experimentally observed to further increase blur effects [71]. Finally, any additional effective blurring introduced during resist development is included in this finding. The combined behavior of these various effects is most likely responsible for the discrepancy between the iterated beam blur and the beam blur derived from the beam image. Due to the difficulty in accounting for each of the above effects in physical detail, we will instead interpret the beam blur as an effective average process blur. Similar approaches (i.e. grouping various contributions to the blur into a single parameter) have been documented in the literature [67, 72].

Thus, determination of the operating parameters required iterations of both the threshold energy and the beam blur. The iterations were carried out as follows. The beam blur was first set to 9.9 nm. The threshold dose was modulated to approximately match the pore size of the median data point in Figure 3.1 (dose of 21,000 $\mu C/cm^2$). The blur was then increased to match the trend of the pore size dependence on dose. The dose and blur were repeatedly adjusted in this manner to best fit the data. The threshold energy was

ultimately found to be 105 μC/cm^2. This was cross-checked with an independent experimental measurement. It is well known that the sensitivity of ZEP-520A varies with process conditions such as development conditions [57, 73] and film thickness [74]. In one relevant case using the same EBL instrument and developer at the Georgia Tech MiRC facility, it was found that 110 μC/cm^2 was required to clear 60 nm ZEP on silicon and 160 μC/cm^2 was required to clear 160 nm ZEP on silicon [74]. These dose values demonstrate that our threshold dose of 105 μC/cm^2 for 100 nm ZEP on silicon is physically reasonable. This value was thus used to determine the internal pore diameter throughout the film under a broad range of system parameters.

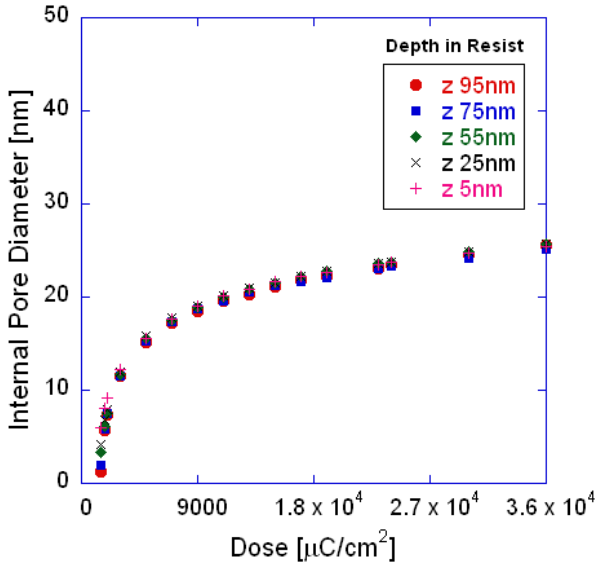

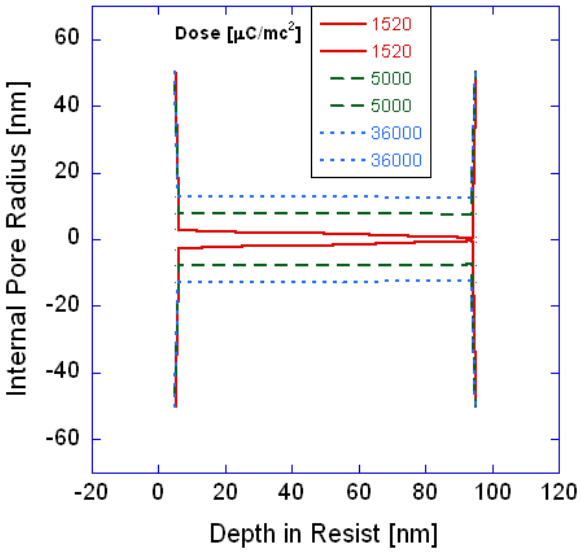

Figure 4.10. Internal pore diameter of single shot pores at different doses in 100nm ZEP on Si assuming a beam blur of 9.9 nm.

The first case studied was that of single-shot pores in 100 nm ZEP on silicon. Figure 4.10 details the internal geometry of single shot pores at different doses in 100 nm of ZEP for a beam blur of 9.9 nm. It is seen that the pores do in fact taper, and most significantly in the sub-10 nm range of pore size. The smallest pore size is reported at a dose of 1520 μC/cm^2 and measures 5.9 nm at the mouth and 1.2 nm at a depth of 95 nm in the film. Larger pores experience a lesser degree of tapering. However, as mentioned previously, the pore sizes in Figure 4.10 do not match well with the experimental data. The reason for this is that the beam image measured from the EBL tool is not the only source of blur in the entire process. Consequently, several simulations were performed to characterize the effects of a broad range of process variables on pore geometry. In every case, the internal pore diameter is reported at multiple depths in the resist and a two dimensional lateral view of the pore is shown on an x-y scale. The process variables studied are dose, beam blur, shot pattern, film configuration, and secondary electron effects. Shot pattern and film configuration are each studied for 2 cases coinciding with

the experimental results reported earlier. In each of these, beam blur and dose are studied extensively. When possible, simulated pore geometry is compared to experiment. The impact of secondary electrons is characterized for cases in which experimental data is available. First, the effects of the beam blur on pore shape are studied using a single shot on 100 nm ZEP on silicon. The results are shown in Figures 4.11-4.17 for blurs of 5, 15, 20, 25, 30, 35, and 39nm.

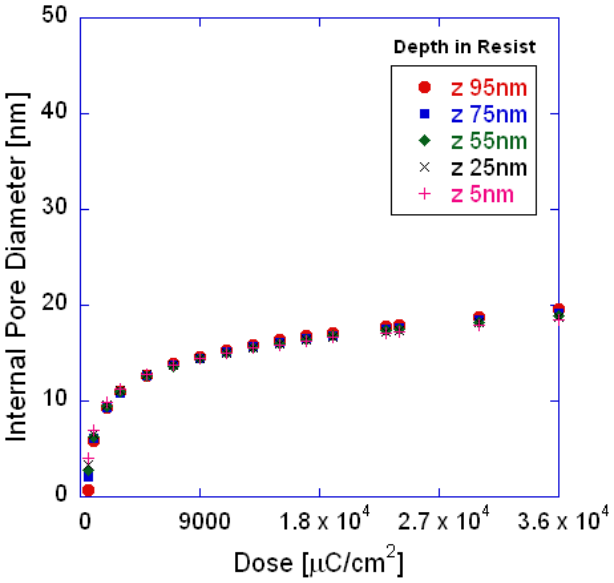

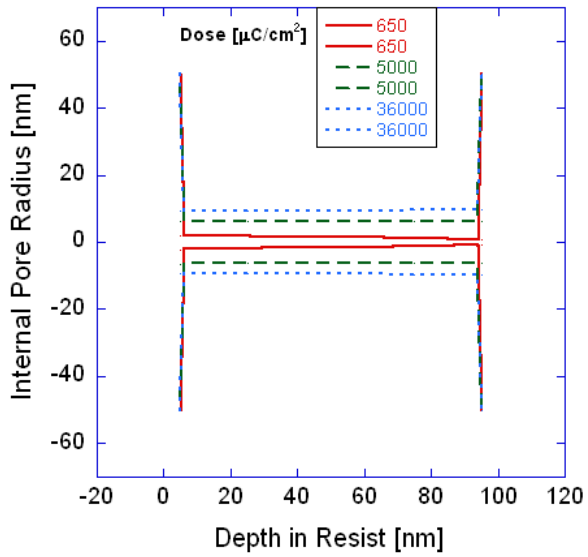

Figure 4.11. Internal pore diameter of single shot pores at different doses in 100nm ZEP on Si assuming a beam blur of 5 nm.

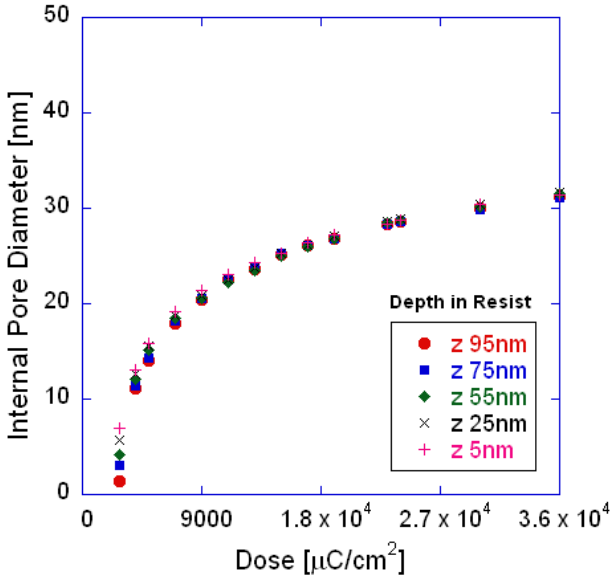

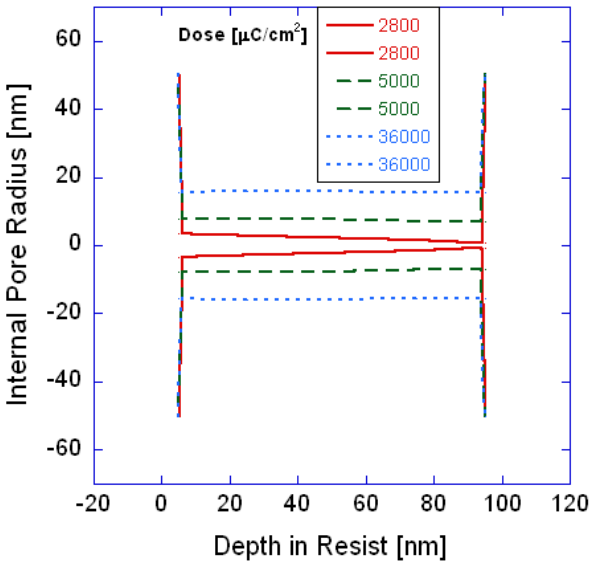

Figure 4.12. Internal pore diameter of single shot pores at different doses in 100nm ZEP on Si assuming a beam blur of 15 nm.

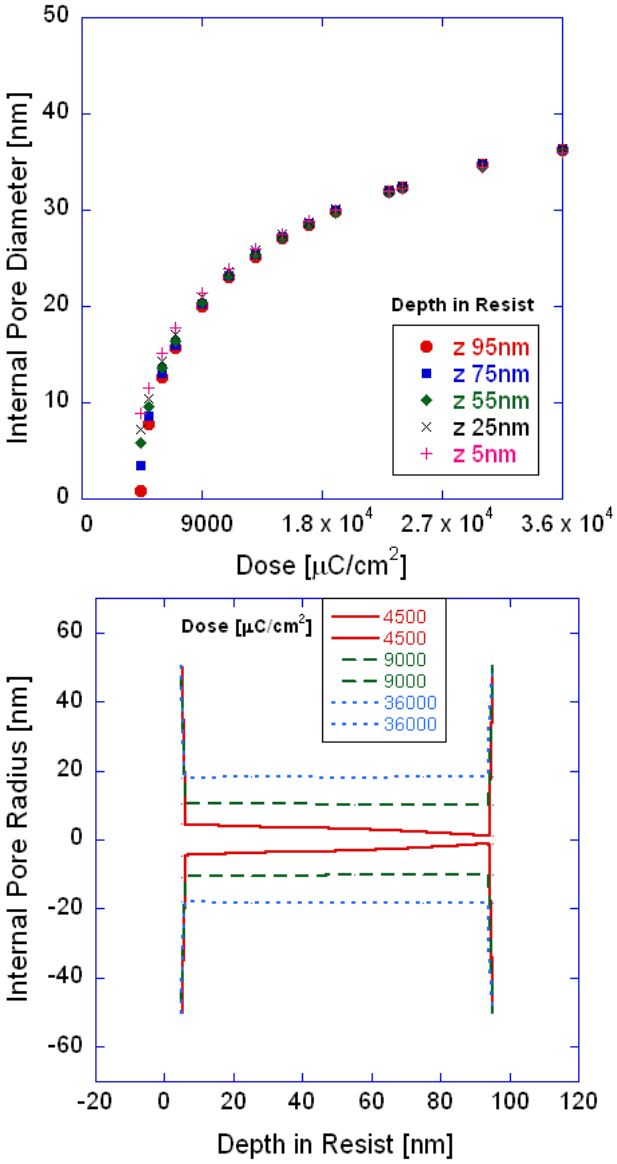

Figure 4.13. Internal pore diameter of single shot pores at different doses in 100nm ZEP on Si assuming a beam blur of 20 nm.

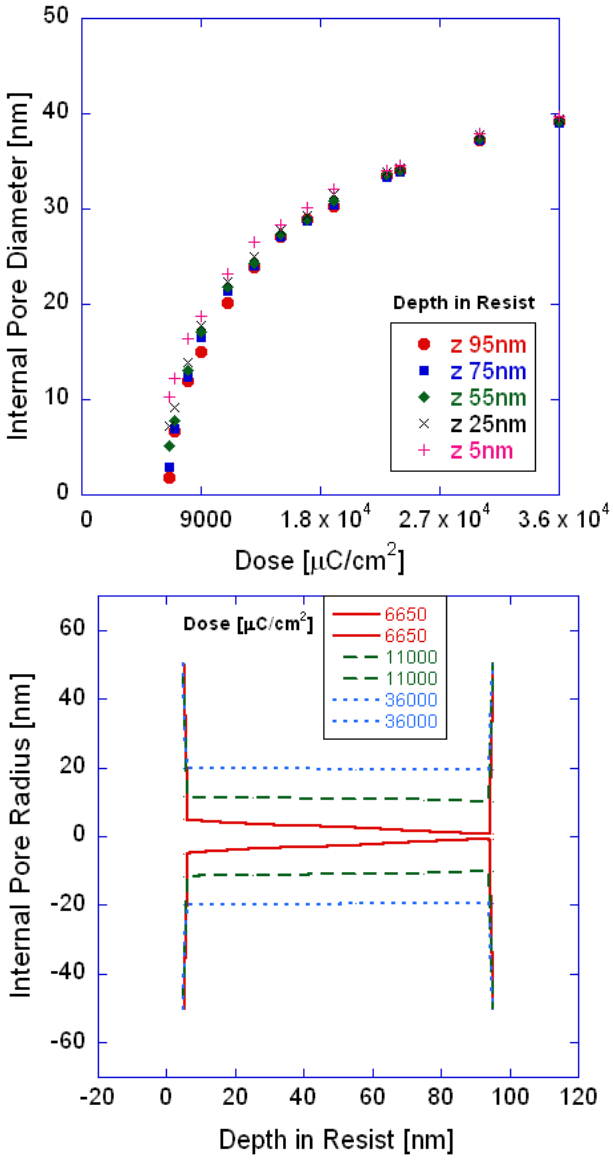

Figure 4.14. Internal pore diameter of single shot pores at different doses in 100nm ZEP on Si assuming a beam blur of 25 nm.

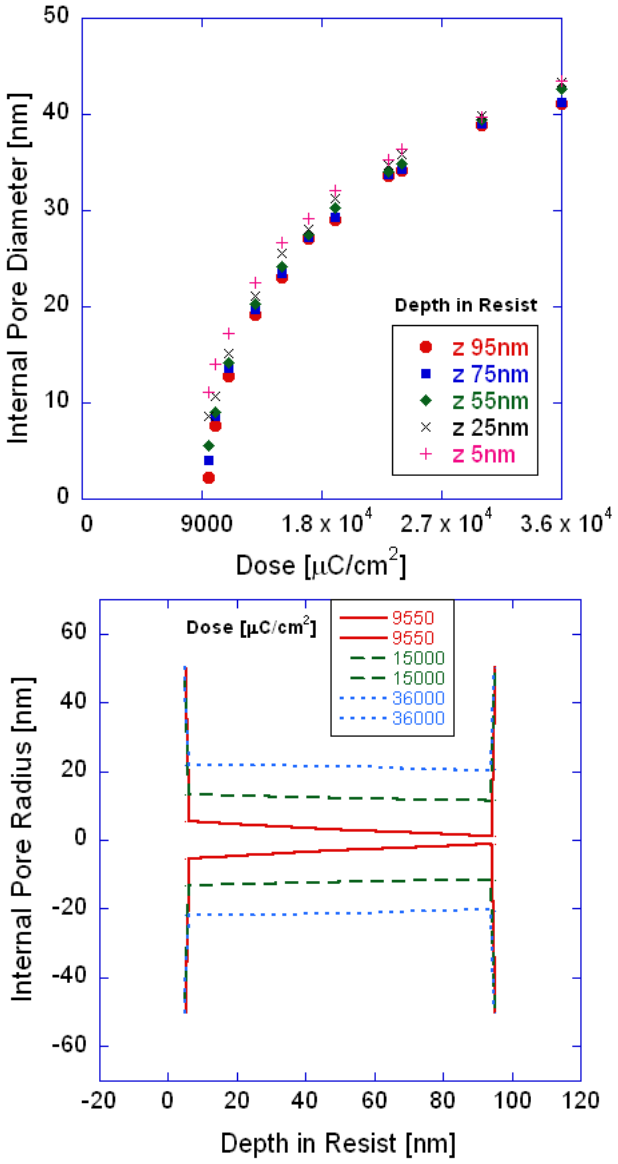

Figure 4.15. Internal pore diameter of single shot pores at different doses in 100nm ZEP on Si assuming a beam blur of 30 nm.

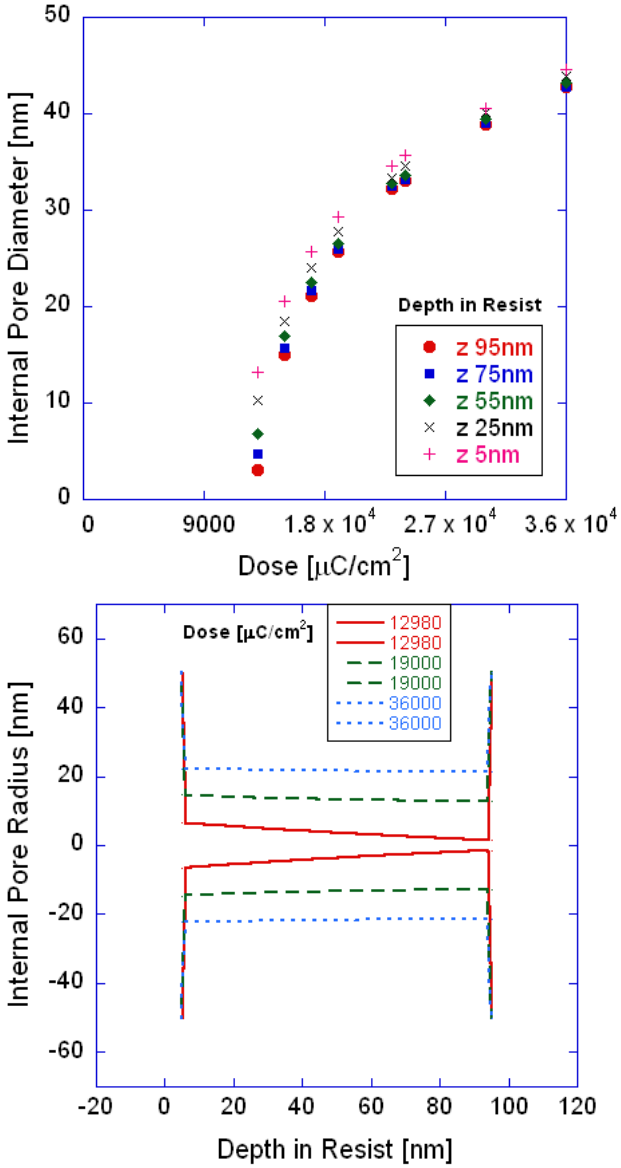

Figure 4.16. Internal pore diameter of single shot pores at different doses in 100nm ZEP on Si assuming a beam blur of 35 nm.

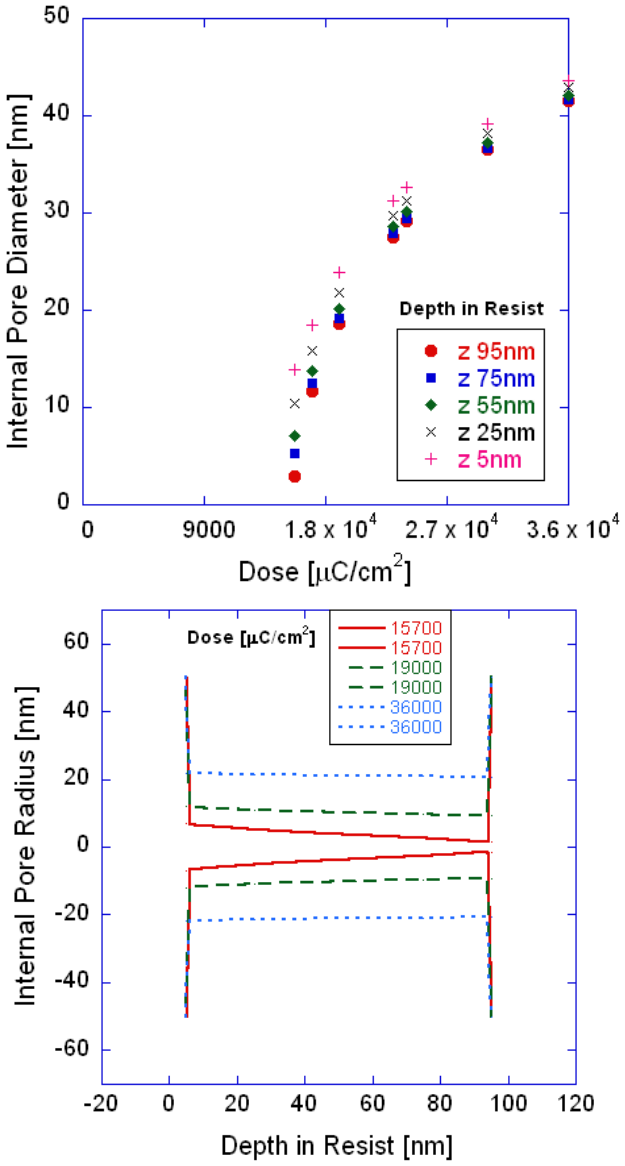

Figure 4.17. Internal pore diameter of single shot pores at different doses in 100nm ZEP on Si assuming a beam blur of 39 nm.

In every case through Figures 4.10 – 4.17, the smallest nanopores experience the highest level of tapering, even at a very small blur. Since the tapering transfers to the substrate (silicon nitride) during etching, we can expect that the nanopores after ICP will taper at least to the degree shown here (and possibly further due to any lateral spread in the ICP etch). If perfectly cylindrical pores are desired, it may be beneficial to actually pattern

larger pores in EBL, since they will have less tapering, and then fill them in with ALD to the desired pore size.

Figures 4.10-4.17 also indicate a notable effect of beam blur on the pore size distribution. As the blur increases, the degree of tapering increases dramatically, especially for the smallest pores. At a blur of 39 nm, the pore tapers from 12.6 nm near the mouth to 3.4 nm near the bottom. This is a sizable discrepancy which may not be well characterized by SEM data alone. To better understand the effects of blur, it was useful to observe the relationships between internal pore diameter and blur at a fixed depth in the pore. Figure 4.18 indicates how the internal pore diameter near the bottom end of the pore changes with blur.

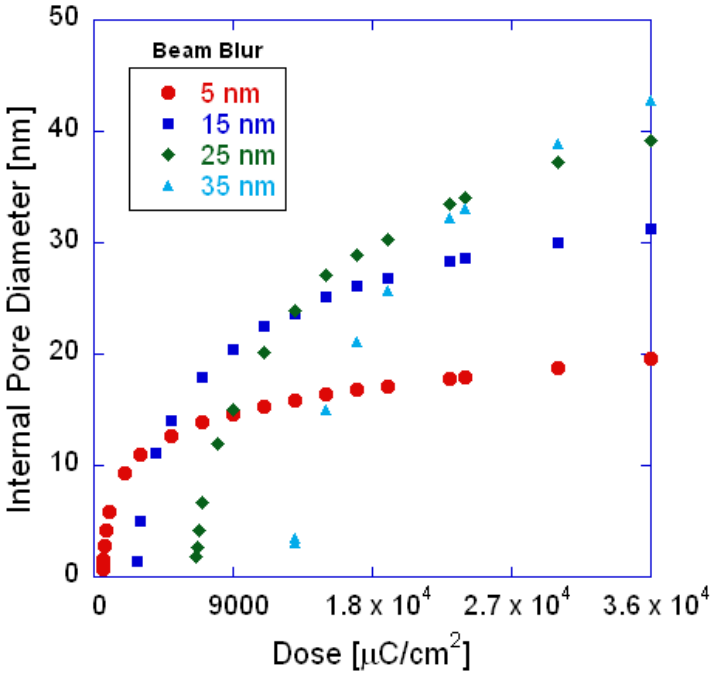

Figure 4.18. Internal pore diameter at a depth of 95 nm in the film (100nm ZEP on Si) when simulated at beam blur of 5 nm, 15 nm, 25 nm, and 35 nm.

From Figure 4.18, the sensitivity of the resist increases with beam blur for larger pore sizes. The relationship between pore size and dose is not linear, although it can appear linear within a range of doses. For each curve there appears to be a dosing region of relatively high sensitivity to the left and relatively low sensitivity to the right. If the beam blur is known for a given instrument, the END size can be predicted at any dose. It is also clear that different combinations of dose and beam blur can yield the same pore size at a given depth. To more closely investigate this relationship, Figures 4.19 and 4.20 examine the internal pore diameter as a function of beam blur at various doses near the bottom of the pore and the mouth of the pore respectively.

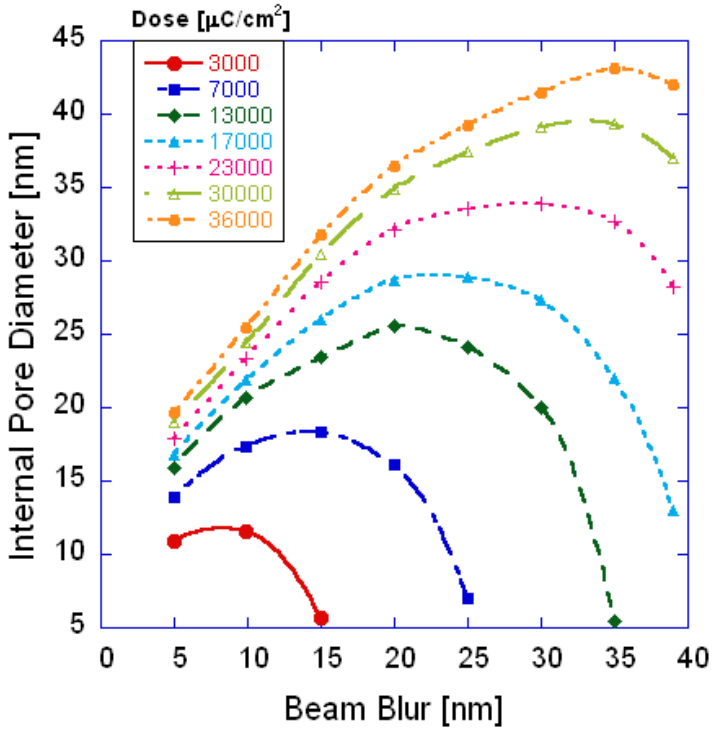

Figure 4.19. Internal pore diameter at a depth of 95 nm in the film (100 nm ZEP on Si) as a function of beam blur at multiple doses.

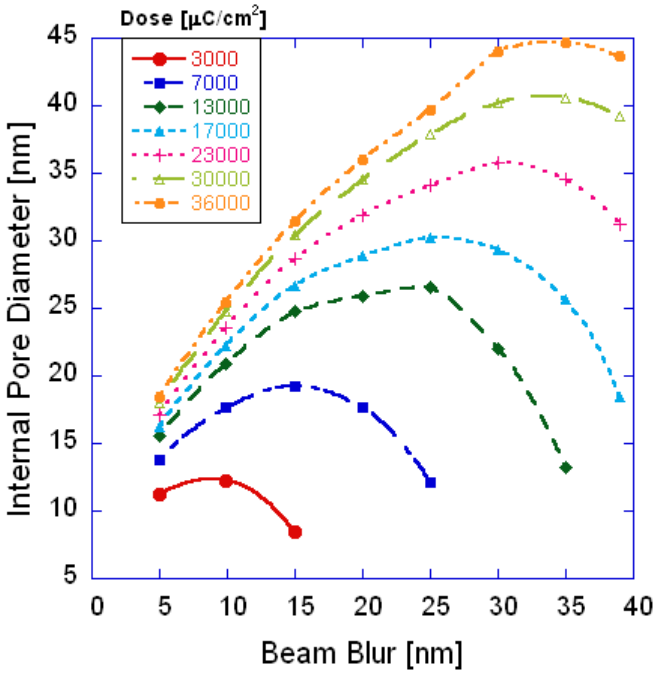

Figure 4.20. Internal pore diameter at a depth of 5 nm in the film (100 nm ZEP on Si) as a function of beam blur at multiple doses.

Figures 4.19 and 4.20 illustrate some interesting phenomena. For every given dose, as blur increases, the feature size increases to a critical value and then declines. As the beam is spread out, it exposes a broader lateral area. At some point the beam becomes too spread out and cannot fully expose the broadened area, causing the decline in feature size. We also recall from Figures 4.10-4.17 that the blur controls tapering of the features. Thus, if the blur can be controlled, multiple features of the same size (a target internal pore diameter at any given depth) can be produced, but *with different degrees of tapering*.

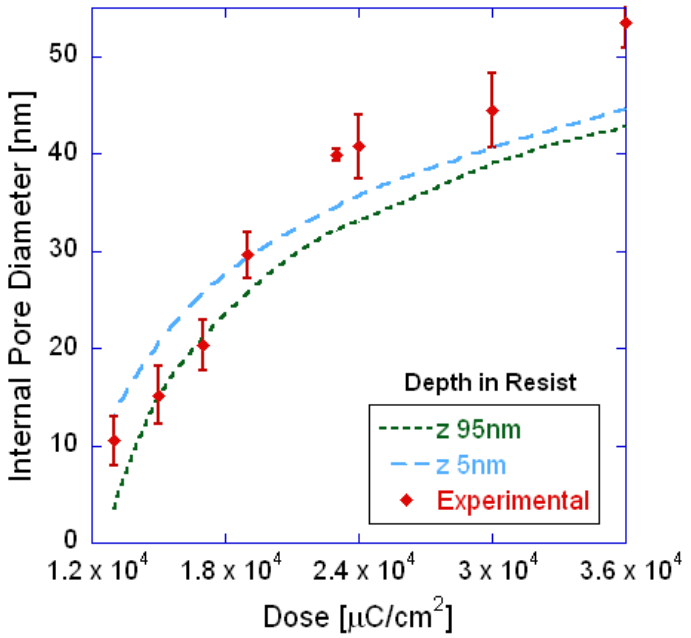

Figure 4.21. Simulated single shot pore geometry at a blur of 35 nm versus observed size in SEM for multiple doses in 100nm ZEP on Si.

Comparing the empirical data to the simulated pore geometry, a beam blur of 35 nm was found to be the operating blur in the experiments. Figure 4.21 demonstrates how the simulated pore size compares with the SEM data. Figure 4.21 shows reasonable agreement between the simulated pore size and the apparent pore size in SEM, especially at the smallest pore sizes. For END technology, this is the region of the most importance. It is noteworthy that the simulations seem to undershoot pore size at larger pore diameters, although it is not clear if this trend continues above 36,000 $\mu C/cm^2$. This may be due to the fact that the SEM data measured pores surrounded by other features. At higher doses, the pores are also larger, which puts them closer to the surrounding features and subjects them to greater proximity effect. This may account for the smaller size of the simulated pores, which were completely isolated.

As a final point of comparison, the energy distributions in the ZEP at a blur of 35 nm are shown in Figures 4.22-4.24. Comparing Figures 4.22-4.24 to Figures 4.7-4.9, we find that our original assumed operating blur produced a dramatically different energy distribution in the resist. The contrast curves in the new regime appear much flatter, indicating that the energy is distributed over a wider range in the radial direction. This concurs with the increase in dose sensitivity observed in the simulated pore geometry. The two dimensional mappings of the energy indicate that the broadening of the energy distribution affects scattering behavior at every depth and reaffirms tapering in the z-direction.

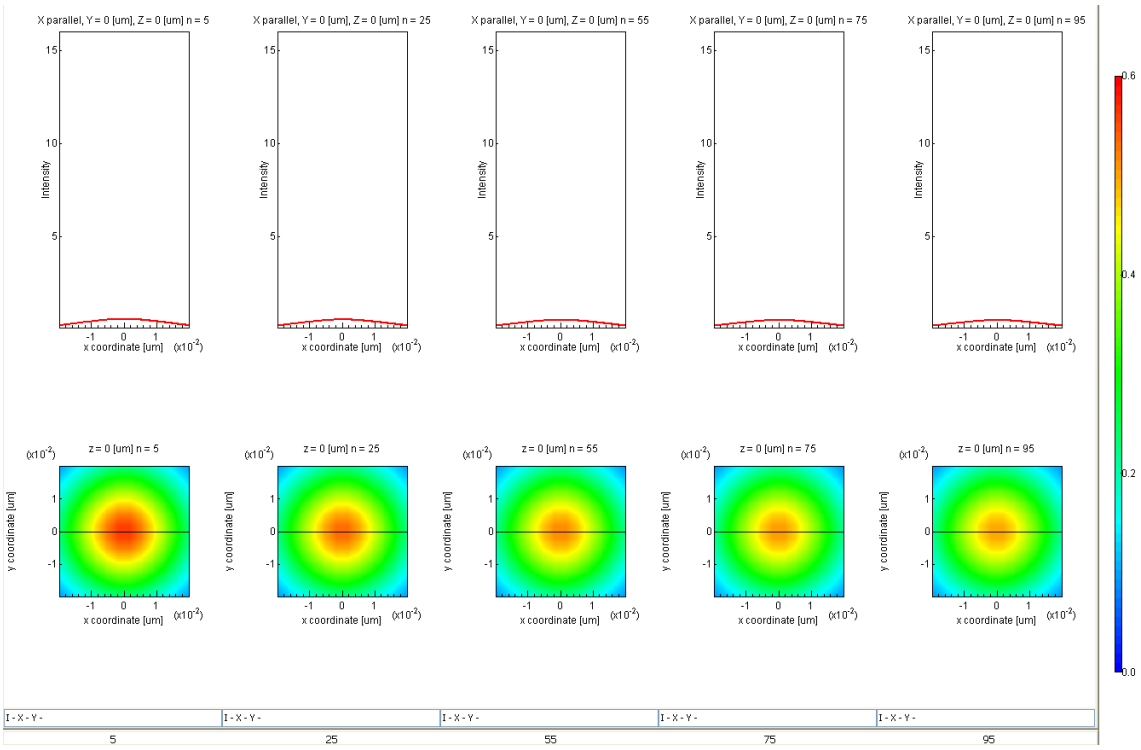

Figure 4.22. Energy distribution in 100 nm ZEP on silicon at depth of 5 nm, 25 nm, 55 nm, 75 nm, and 95 nm in the film from left to right, respectively. The beam blur was 35 nm. The dose received was 13000 $\mu C/cm^2$.

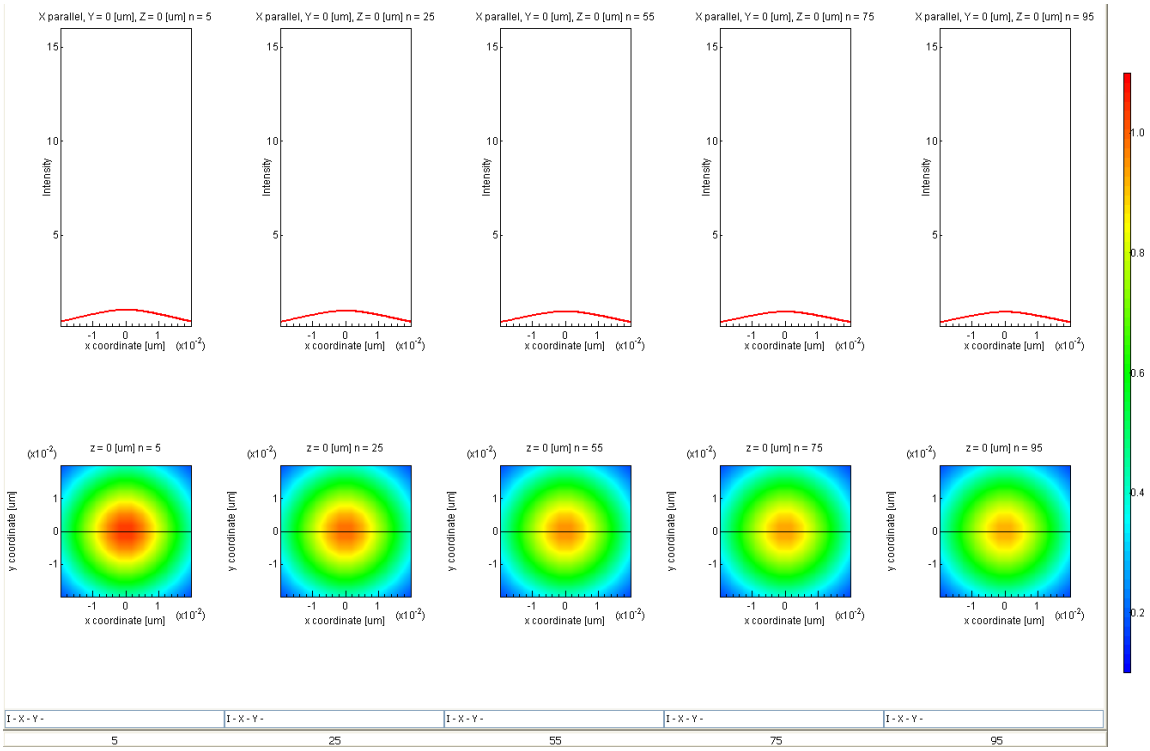

Figure 4.23. Energy distribution in 100 nm ZEP on silicon at depth of 5 nm, 25 nm, 55 nm, 75 nm, and 95 nm in the film from left to right, respectively. The beam blur was 35 nm. The dose received was 24000 $\mu C/cm^2$.

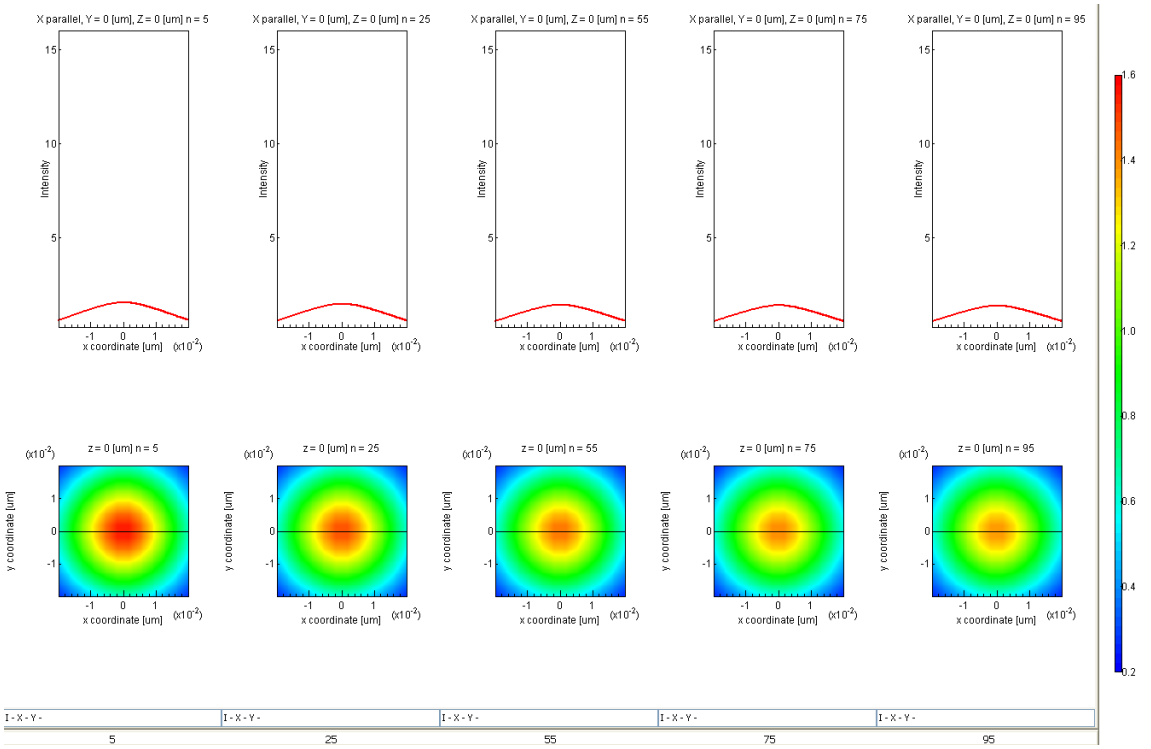

Figure 4.24. Energy distribution in 100 nm ZEP on silicon at depth of 5 nm, 25 nm, 55 nm, 75 nm, and 95 nm in the film from left to right, respectively. The beam blur was 35 nm. The dose received was 36000 $\mu C/cm^2$.

4.4 Simulating Single Shot Pore Geometry in ZEP on Silicon Nitride on Silicon

Following the course of the experiments, the next set of simulations studied single shot pores in 100 nm ZEP on 19 nm silicon nitride on silicon. Figures 4.25-4.32 demonstrate the simulated pore geometry over a broad dosing region and at beam blurs of 5 nm, 9.9 nm, 15 nm, 20 nm, 25 nm, 30 nm, 35 nm, and 39 nm. The results closely parallel the trends observed in 100 nm ZEP on silicon. The higher blurs result in a higher dose sensitivity and tapering. Again, the broadest tapering occurs at the smallest pore sizes / lowest doses. The results are compared to the pore sizes simulated for ZEP on Si in Figures 4.32 and 4.33 at fixed depths of 95 nm and 5 nm respectively.

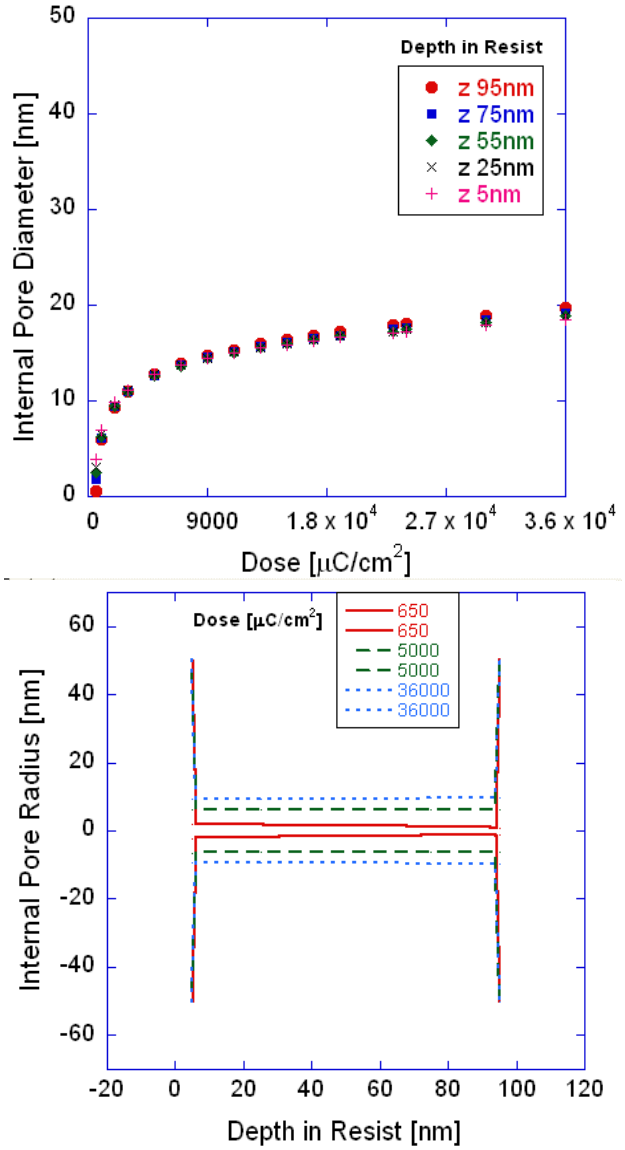

Figure 4.25. Internal pore diameter of single shot pores at different doses in 100nm ZEP on 19nm Si_3N_4 on Si assuming a beam blur of 5 nm.

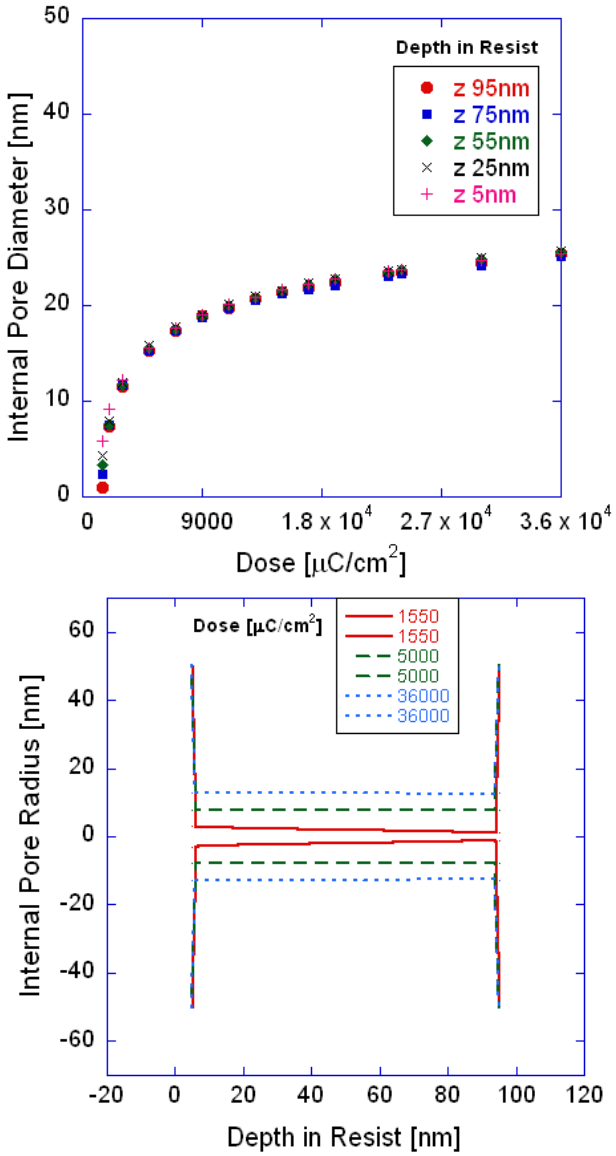

Figure 4.26. Internal pore diameter of single shot pores at different doses in 100nm ZEP on 19nm Si_3N_4 on Si assuming a beam blur of 9.9 nm.

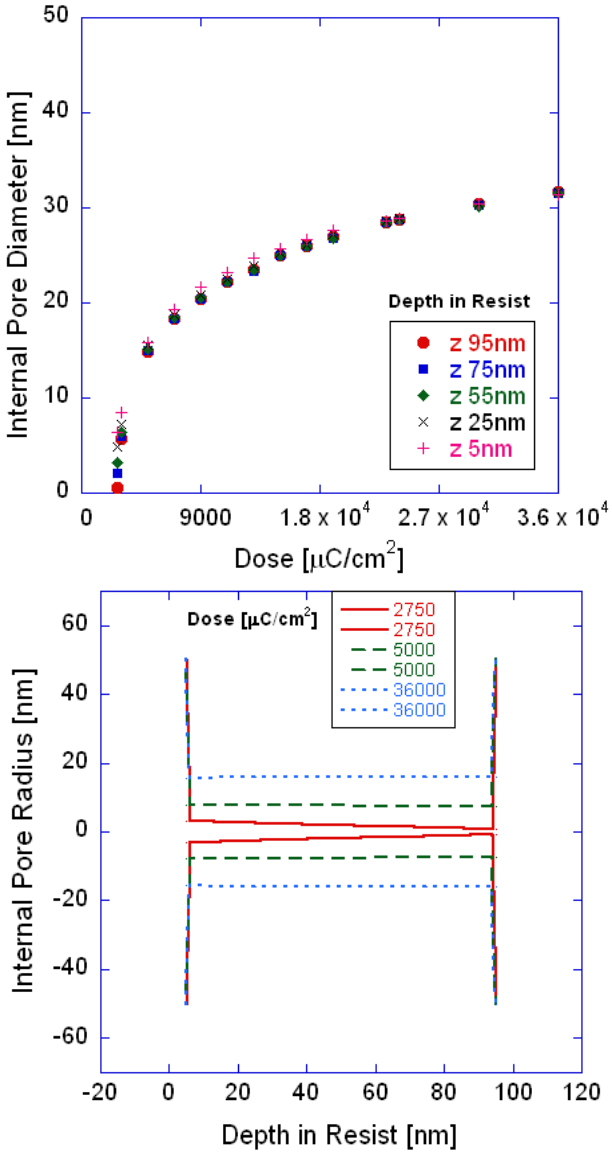

Figure 4.27. Internal pore diameter of single shot pores at different doses in 100nm ZEP on 19nm Si_3N_4 on Si assuming a beam blur of 15 nm.

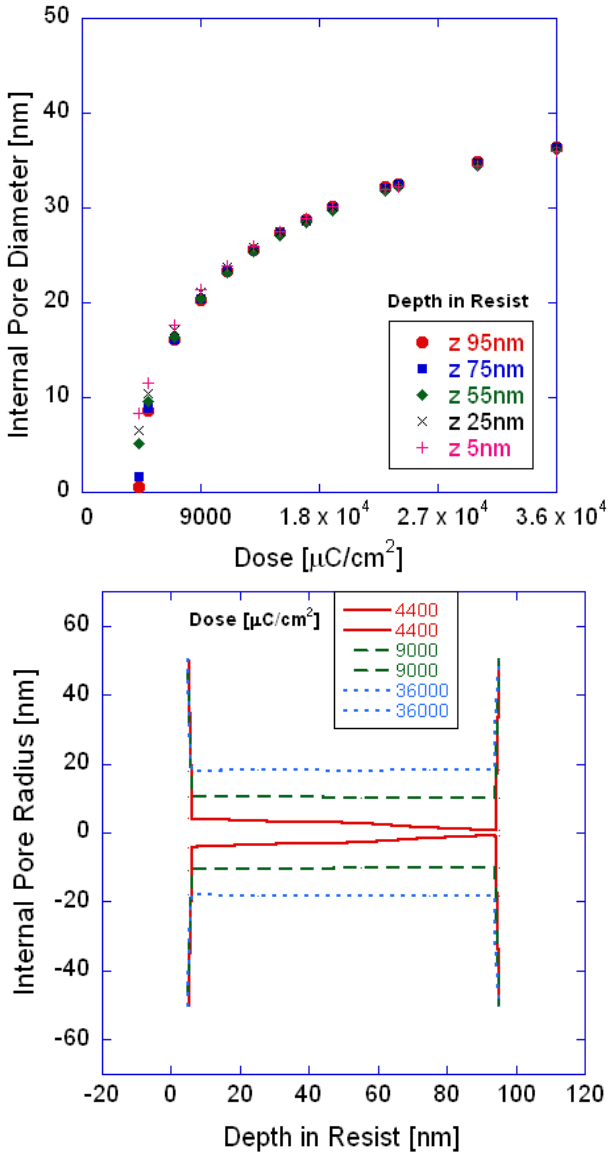

Figure 4.28. Internal pore diameter of single shot pores at different doses in 100nm ZEP on 19nm Si_3N_4 on Si assuming a beam blur of 20 nm.

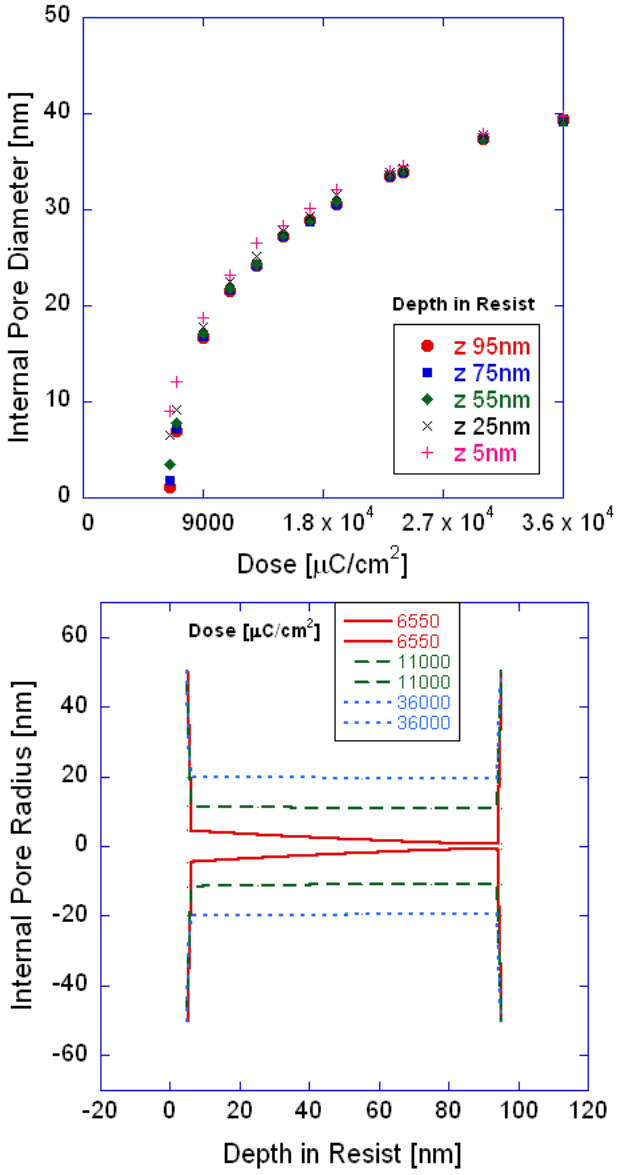

Figure 4.29. Internal pore diameter of single shot pores at different doses in 100nm ZEP on 19nm Si_3N_4 on Si assuming a beam blur of 25 nm.

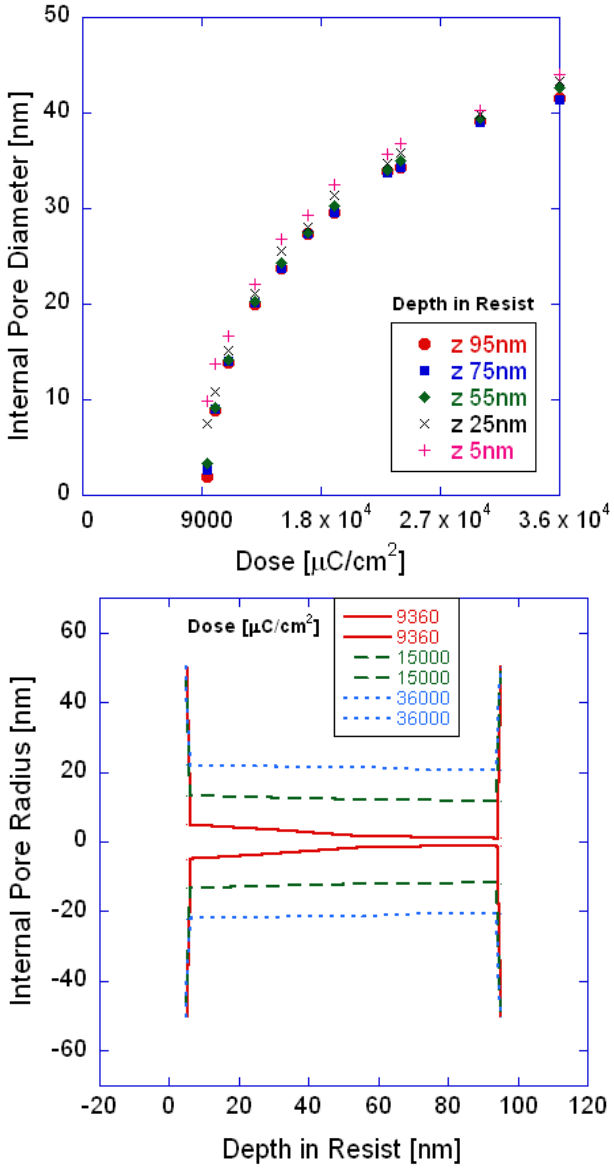

Figure 4.30. Internal pore diameter of single shot pores at different doses in 100nm ZEP on 19nm Si_3N_4 on Si assuming a beam blur of 30 nm.

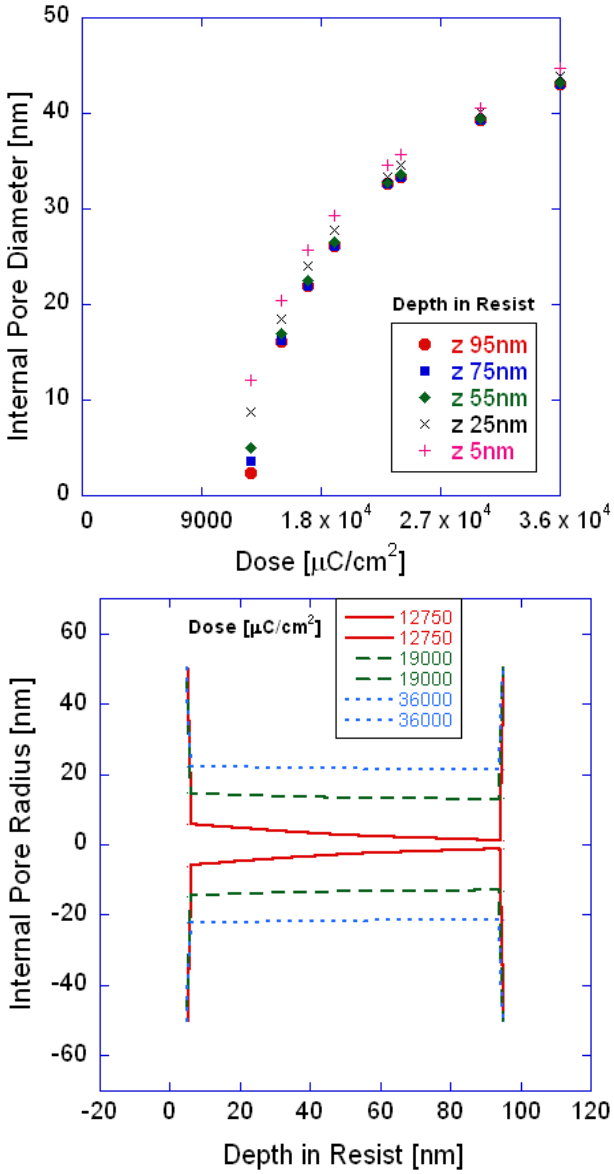

Figure 4.31. Internal pore diameter of single shot pores at different doses in 100nm ZEP on 19nm Si_3N_4 on Si assuming a beam blur of 35 nm.

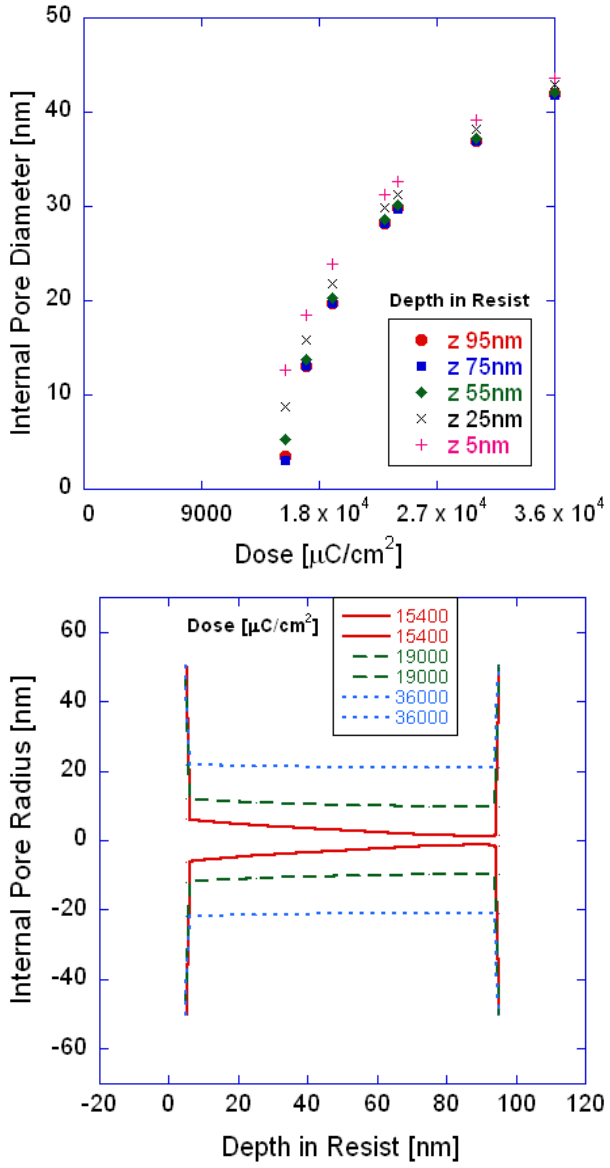

Figure 4.32. Internal pore diameter of single shot pores at different doses in 100nm ZEP on 19nm Si_3N_4 on Si assuming a beam blur of 39 nm.

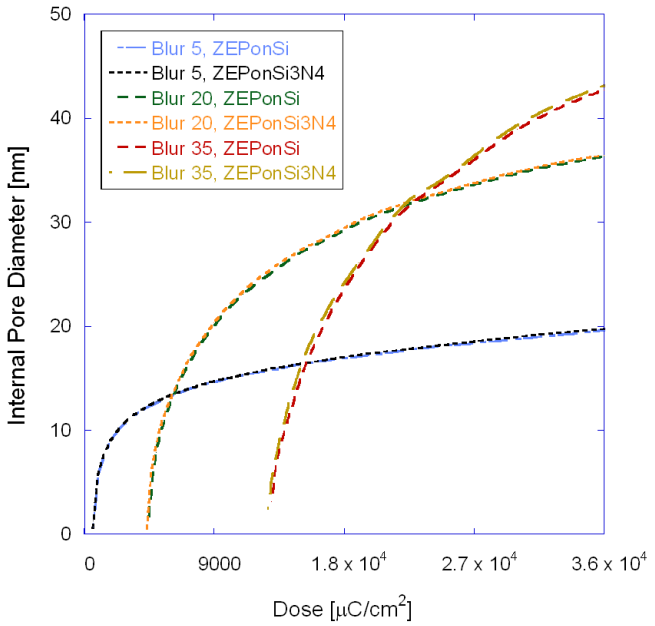

Figure 4.33. Simulated pore diameter as a function of dose and beam blur for 100 nm ZEP on silicon and 100 nm ZEP on 19 nm silicon nitride on silicon at a fixed depth of 95 nm in the film.

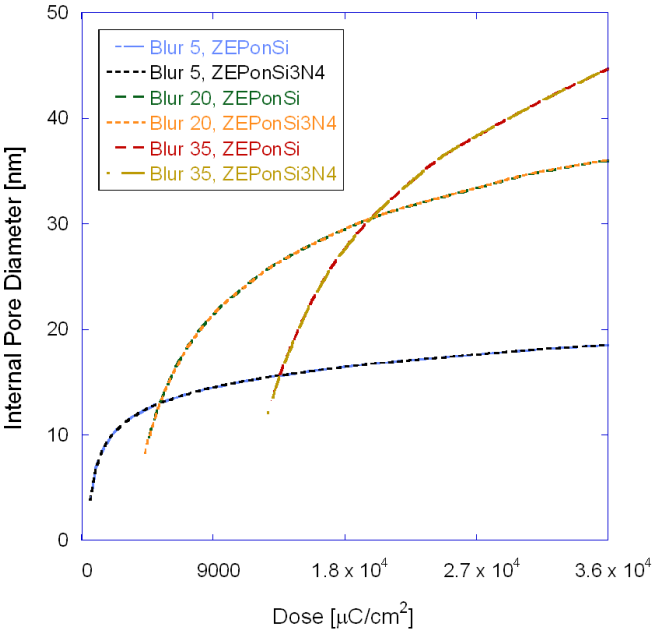

Figure 4.34. Simulated pore diameter as a function of dose and beam blur for 100 nm ZEP on silicon and 100 nm ZEP on 19 nm silicon nitride on silicon at a fixed depth of 5 nm in the film.

Figures 4.33 and 4.34 confirm that the internal diameter is nearly identical when silicon nitride backs the ZEP. There is a slight but important difference between the two film configurations at our operating blur of 35 nm. At a depth of 5 nm (near the mouth of the pore), the internal pore diameter is almost identical for both films. At a depth of 95 nm, however, the pores in ZEP on silicon nitride are slightly larger. This indicates that the pores over silicon nitride taper slightly less. This may be a trivial effect for larger pores, but it has a tremendous impact for END pores of sub-10 nm in size. Let us consider two pores: one patterned in 100 nm ZEP on silicon, and one patterned in 100 nm ZEP on silicon nitride on silicon. At a blur of 35 nm and a dose of 13,000 μC/cm^2, both pores will appear to be 13 nm near the mouth, but the pore in ZEP on silicon will taper down to 3.5 nm while its counterpart on nitride will taper down to 5.5 nm. This is critical information for planning the ensuing ICP step. Comparing the simulated pore sizes to the experimental data in Chapter 3 yields an effective operating blur of about 39 nm. The experimental and simulated data is compared in Figure 4.35 below.

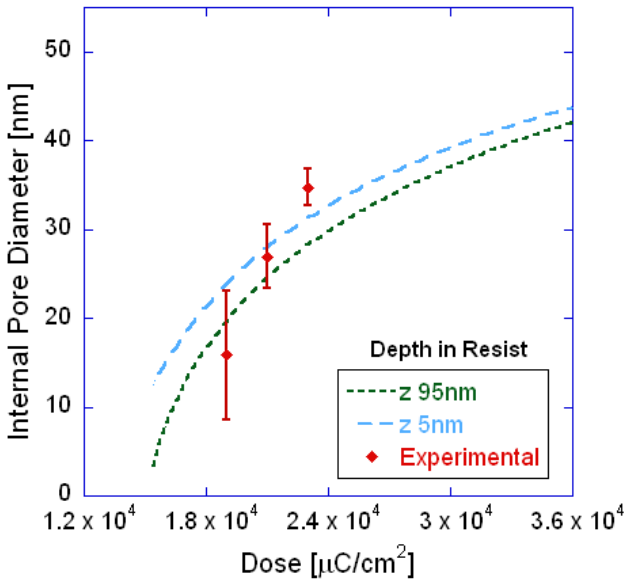

Figure 4.35. Simulated single shot pore geometry at a blur of 39 nm versus observed size in SEM for multiple doses in 100nm ZEP on 19nm silicon nitride on Si

From Figure 4.34, it is seen that the experimental data follows the trend of the simulated data, and the derived blur of 39 nm agrees closely with the 35 nm blur for ZEP on silicon.

4.5 Pattern Transfer from ZEP to Silicon Nitride Film

Once the pores are patterned in the ZEP, they are transferred to the silicon nitride below by ICP etching. Here it is assumed that the effects of undercutting and tapering in the ICP are nominal and that the pattern transfer occurs at a uniform rate in the z-direction (into the nitride). It is also important to note that because the nitride is much thinner than the ZEP, the pattern transfer to the nitride depends on how much etching occurs. This can be determined from SEM data of the pore size distribution in the silicon nitride following etching.

The tapering of the pore is transferred to the nitride as well, but the degree of tapering changes because of the difference in etch ratio between the ZEP and nitride. To correct for this, the initial tapering profile is flattened (or stretched) by a factor of the etch ratio of ZEP to silicon nitride. Over the course of several trials the average etch ratio of ZEP:Si_3N_4 under the operating parameters was 2:1. Therefore, the slope of the pore wall in the nitride is twice the slope in the initial ZEP. This means twice the level of tapering. To illustrate this point, Figures 4.36a-c visually demonstrate the method to attain the pore geometry in 19 nm silicon nitride following etching. We begin with the simulated internal pore geometry in 100 nm ZEP shown in Figure 4.36.a. Let us then assume that we etch this pore, remove the resist, and measure the mouth of the pore in nitride to be 30 nm in SEM. In Figure 4.36.b, we identify where this occurs in the ZEP profile. Mathematically, we can fit the walls of the pore to polynomial functions, subtract them, and solve for the depth *z* where the difference is 30 nm. The green box in the figure spans the thickness of the silicon nitride (19 nm).

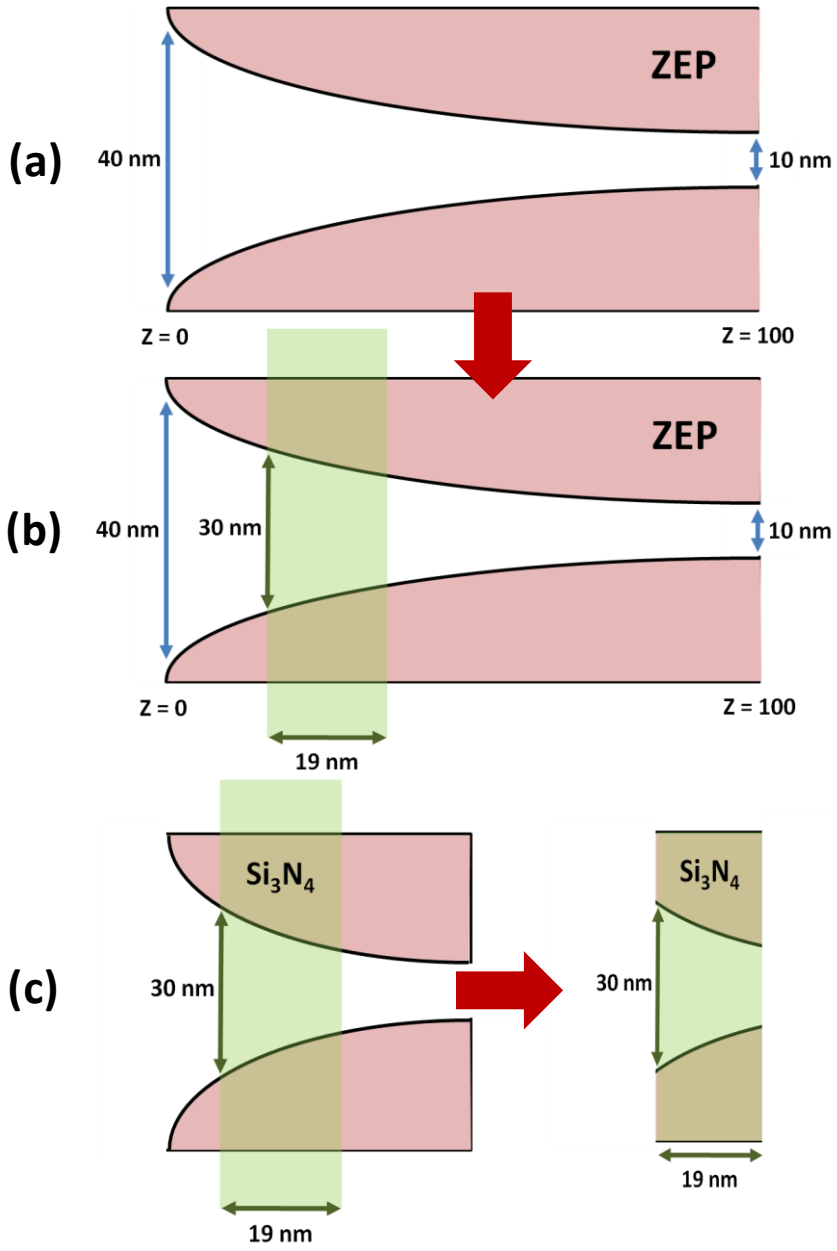

Figure 4.36. (a) Start with the simulated internal pore geometry of a 40 nm pore in 100 nm ZEP. (b) Identify the new size of the pore mouth from the SEM size distribution. (c) Adjust the tapering profile in silicon nitride.

Figures 4.36a-c demonstrate that pore size distribution can be tuned to a degree by choice of etching depth in the ICP. The size of the final pore can essentially range from the smallest to the largest internal diameter of the pattern in ZEP. The profiles of the experimental single shot pores in silicon nitride were determined using this method at blur 39 nm and are reported in Figure 4.37 below relative to their original geometry in ZEP. This demonstrates the variability in internal geometry resulting from different degrees of etching in the ICP. The pores dosed at 19000 and 21000 μC/cm^2 were etched to a lesser degree and therefore the pattern was transferred to the nitride in a region of less tapering (higher z). In contrast, the pore dosed at 23000 μC/cm^2 was etched in a region of more tapering (lower z) and the tapering was magnified in the nitride.

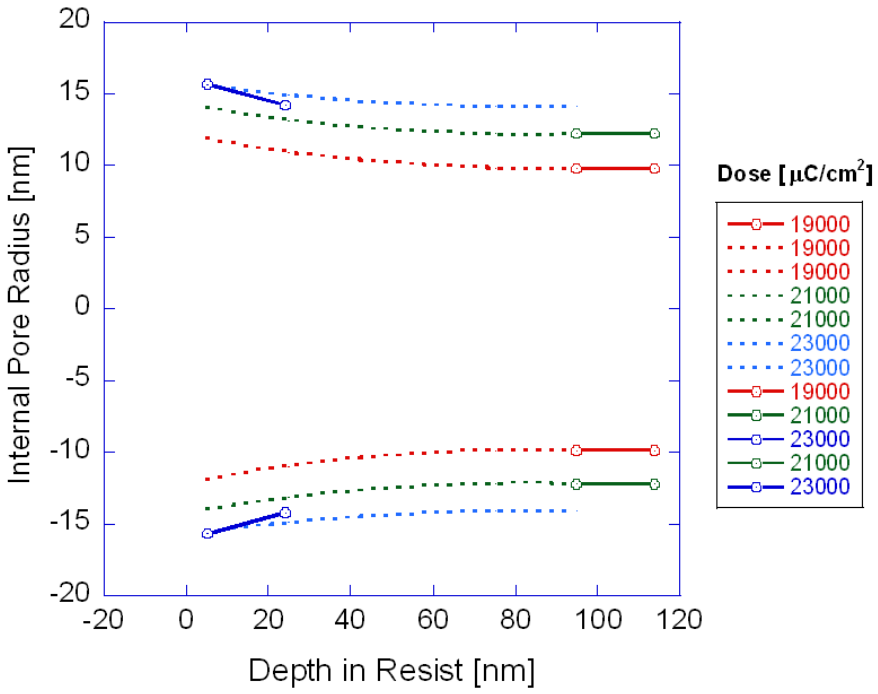

Figure 4.37. Internal pore geometry for single shot pores in silicon nitride at three different doses. Dotted lines represent the original pore geometry. Solid lines indicate the calculated pore geometry in the silicon nitride after etching.

4.6 Role of Secondary Electrons in EBL

Sceleton X was also used to calculate PSFs and perform analogous simulations to those discussed in section 4.4. Because Sceleton X does not calculate secondary electron emission, the results here are compared to Figures 4.12-4.19 to determine the effects of secondary electrons on the pore geometry in the resist. This is not only of fundamental interest, but also useful in practice because many researchers currently rely on Sceleton X for proximity correction in EBL. Figures 4.38-4.43 below demonstrate the simulated pore geometry without secondary electrons at a blur of 5 nm, 9.9 nm, 15 nm, 20 nm, 25 nm, and 30 nm.

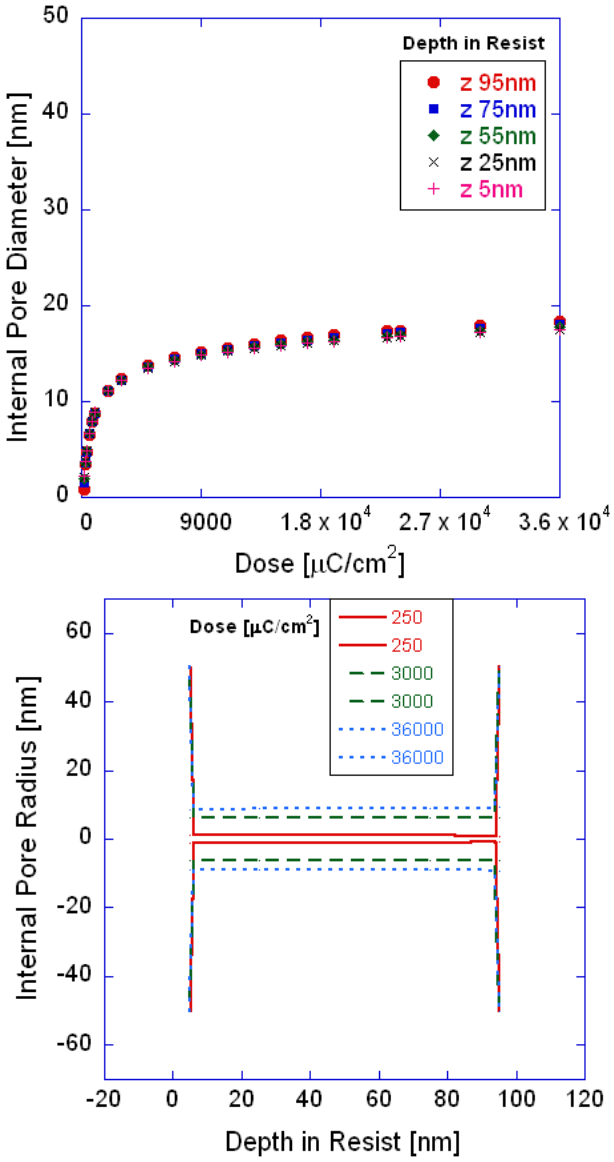

Figure 4.38. Internal pore diameter of single shot pores at different doses in 100nm ZEP on Si assuming a beam blur of 5 nm and no secondary electron emission.

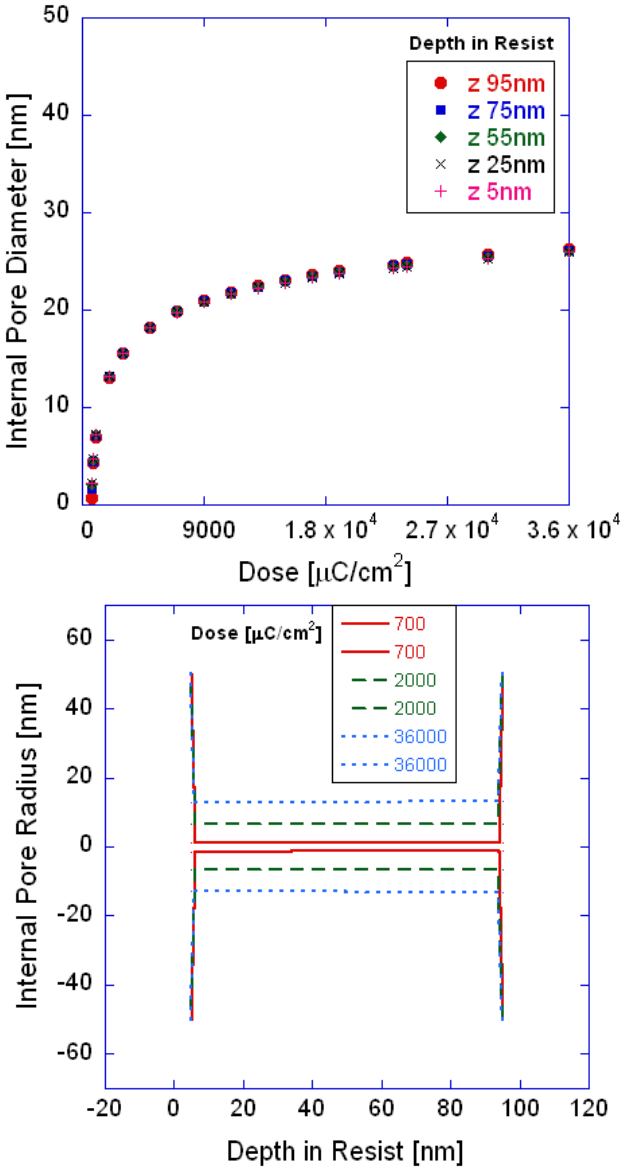

Figure 4.39. Internal pore diameter of single shot pores at different doses in 100nm ZEP on Si assuming a beam blur of 9.9 nm and no secondary electron emission.

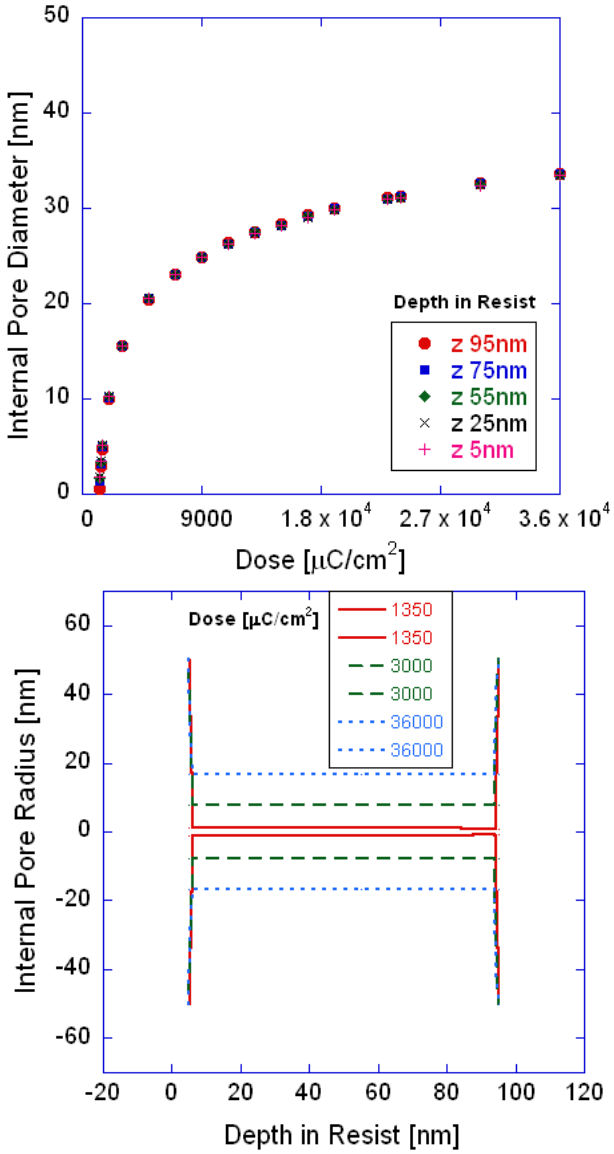

Figure 4.40. Internal pore diameter of single shot pores at different doses in 100nm ZEP on Si assuming a beam blur of 15 nm and no secondary electron emission.

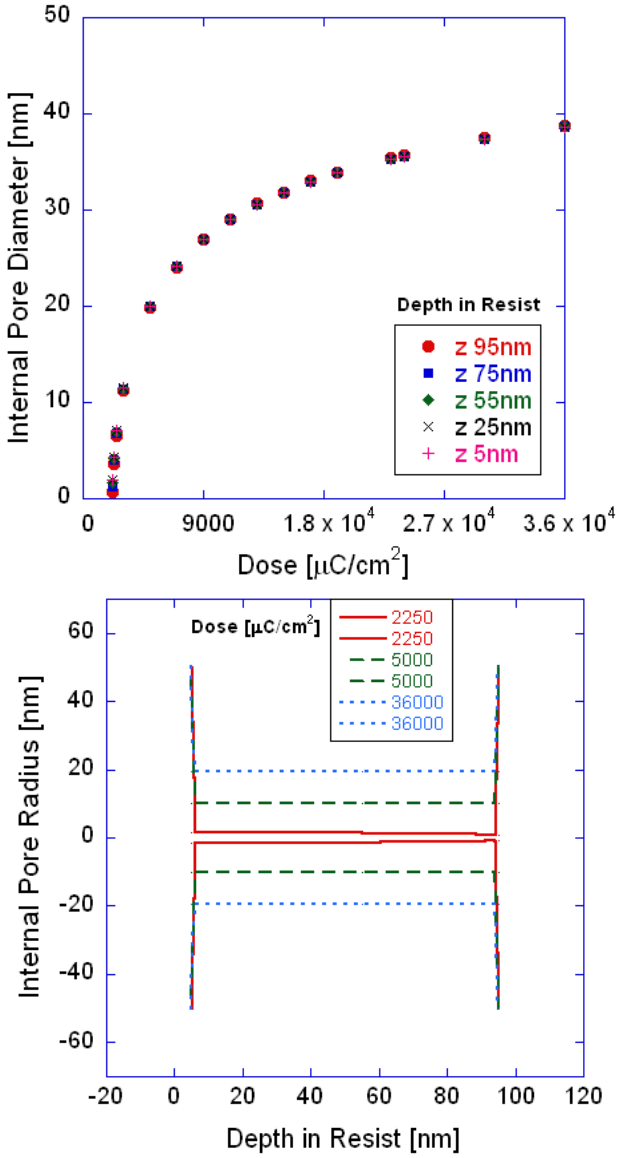

Figure 4.41. Internal pore diameter of single shot pores at different doses in 100nm ZEP on Si assuming a beam blur of 20 nm and no secondary electron emission.

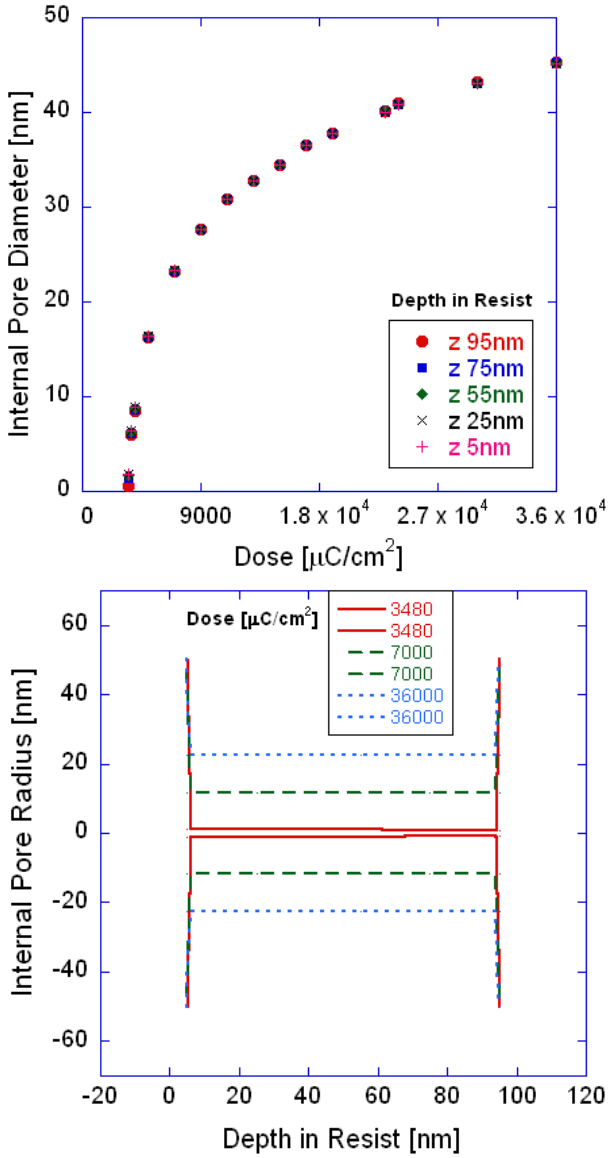

Figure 4.42. Internal pore diameter of single shot pores at different doses in 100nm ZEP on Si assuming a beam blur of 25 nm and no secondary electron emission.

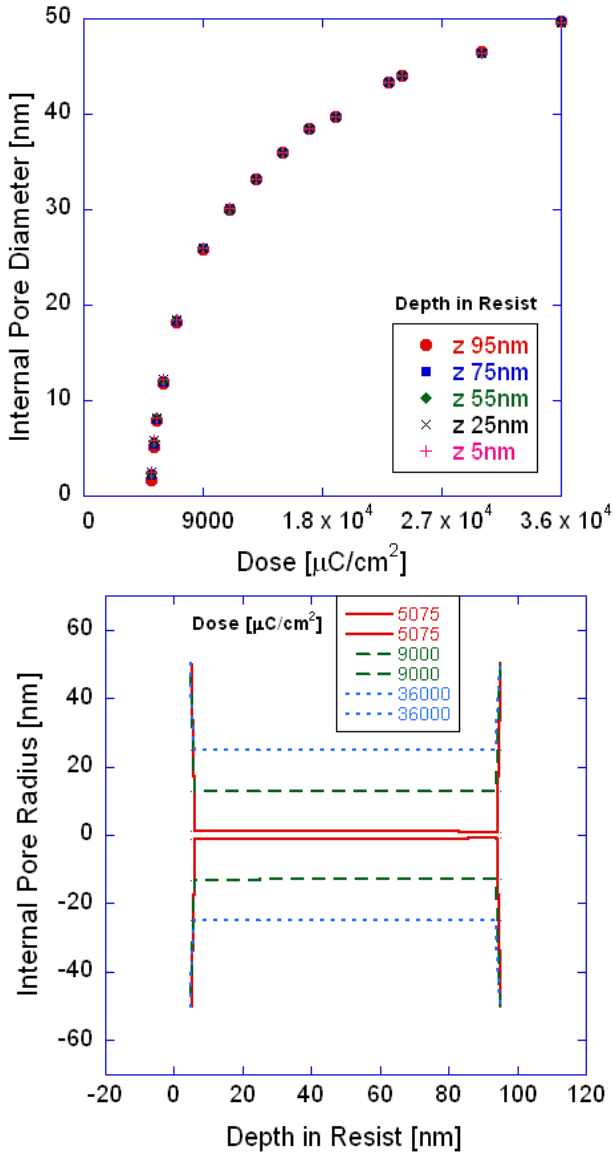

Figure 4.43. Internal pore diameter of single shot pores at different doses in 100nm ZEP on Si assuming a beam blur of 30 nm and no secondary electron emission.

From Figures 4.38-4.43, it is found that omitting secondary electron emissions fails to adequately model the tapering of the pore in every case. This is a critical insight for small pore sizes and high blurs. The figures also reveal that without secondary electron emissions, the resist would not develop at a blur of 35 nm (or 39 nm) even at a dose of 36,000 μC/cm^2. Analogous simulations were performed using Sceleton X for 100

nm ZEP on 19 nm silicon nitride on silicon. The results were nearly identical to those in Figures 4.38-4.43, and are not reproduced here but rather in Appendix A simply for completeness. Based on this fact, the differences between electron scattering in ZEP versus scattering in ZEP on nitride is due primarily to secondary electron emissions. Thus, from Figures 4.33 and 4.34, silicon nitride increases the production of secondary electrons relative to silicon while forward and back scattering events occur with nearly the same frequency and length scales.

4.7 Simulating Multiple Shot Pore Geometry in ZEP on Silicon Nitride on Silicon

Finally, simulations were performed using multiple shot dosing. The pattern studied was the 30 nm circle used in the experimental pores whose size distribution was reported in Figure 3.4. Figures 4.44-4.47 demonstrate the internal geometry of the pores at beam blurs 20, 30, 40, and 50 respectively.

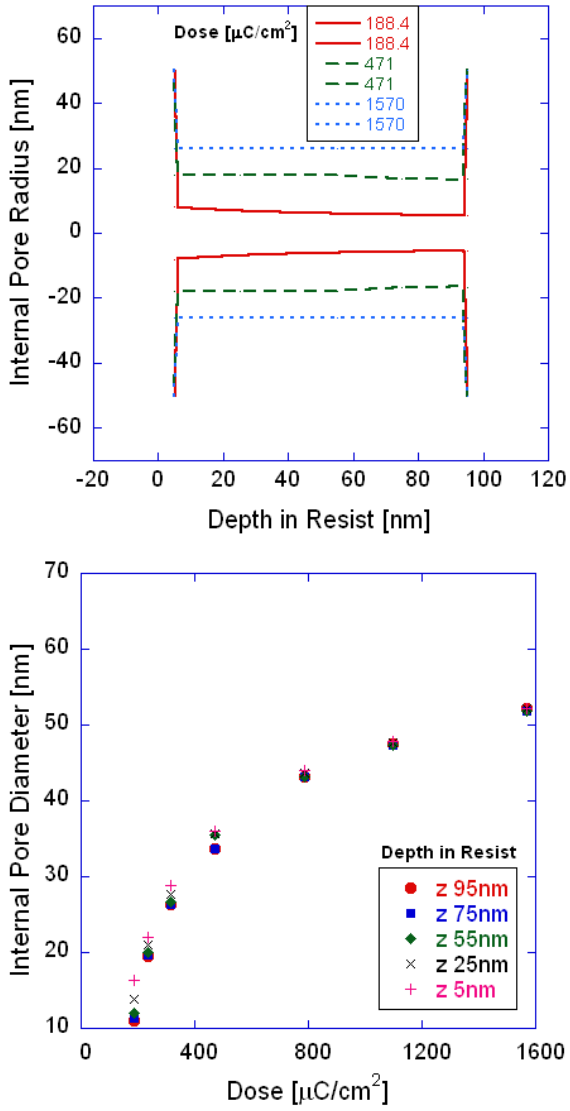

Figure 4.44. Internal pore diameter of multiple shot pores at different doses in 100nm ZEP on 19 nm silicon nitride on silicon at a beam blur of 20 nm.

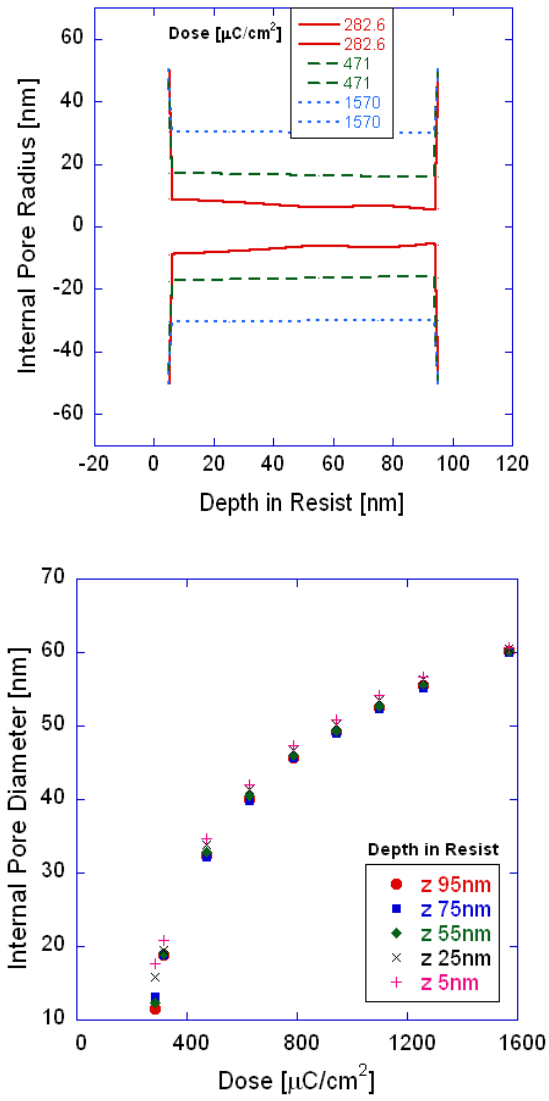

Figure 4.45. Internal pore diameter of multiple shot pores at different doses in 100nm ZEP on 19 nm silicon nitride on silicon at a beam blur of 30 nm.

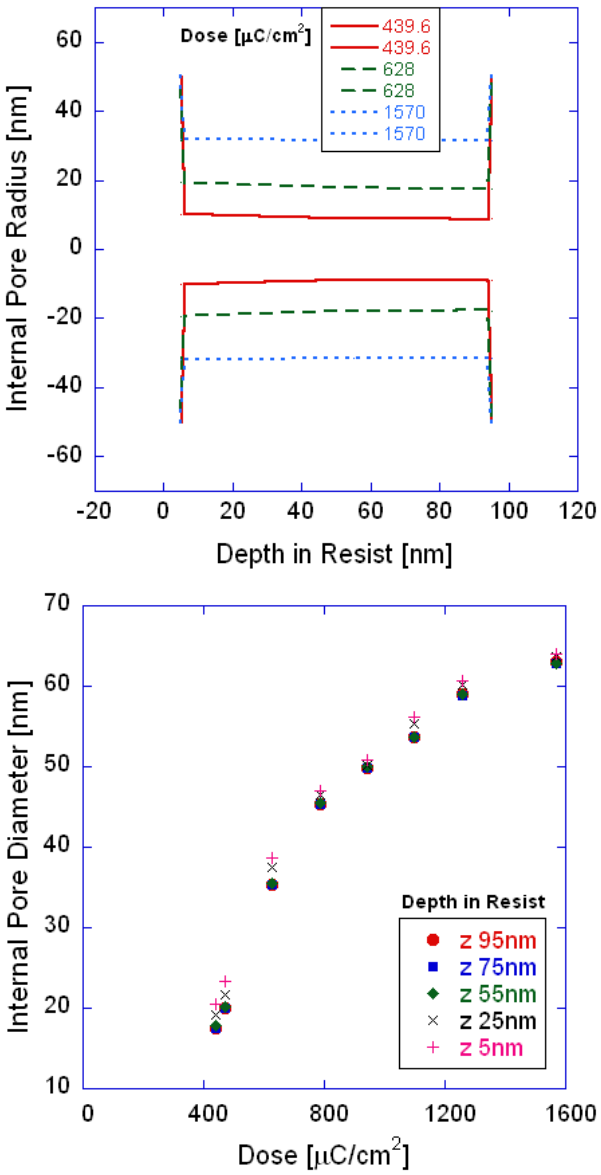

Figure 4.46. Internal pore diameter of multiple shot pores at different doses in 100nm ZEP on 19 nm silicon nitride on silicon at a beam blur of 40 nm.

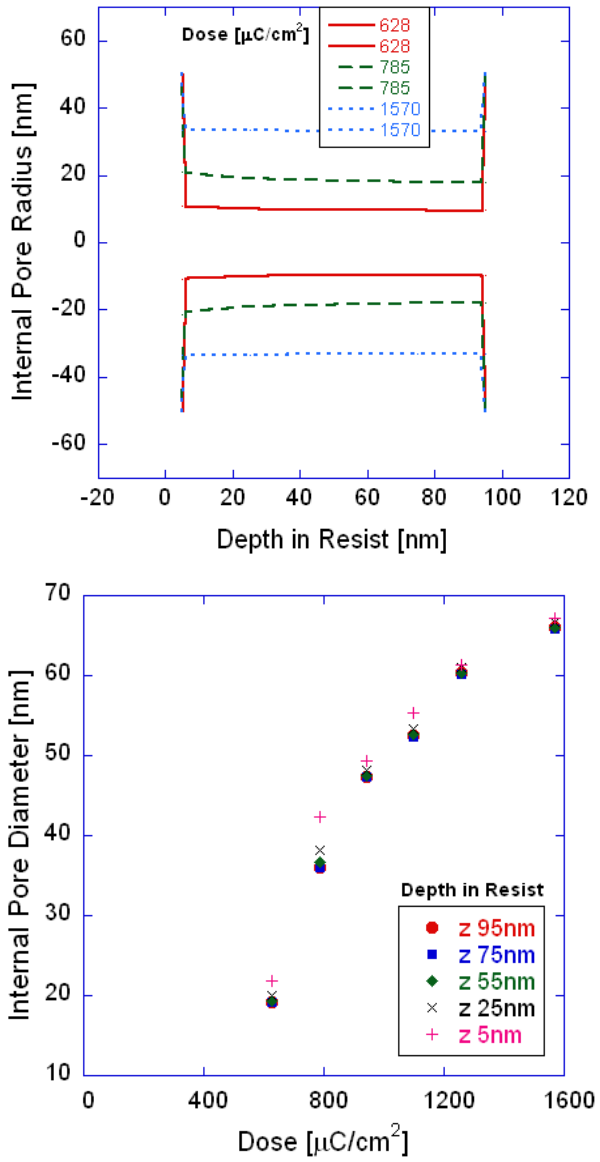

Figure 4.47. Internal pore diameter of multiple shot pores at different doses in 100nm ZEP on 19 nm silicon nitride on silicon at a beam blur of 50 nm.

From Figures 4.44-4.47, it is seen that the smallest pore sizes attainable tapered down to 5 nm, which is unexpectedly small considering the pattern size of 30 nm. A pore size of 5 nm is still more than twice as large as the smallest pore sizes predicted using a single shot of the beam. Tapering in Figures 4.44-4.47 is generally less than in the single shot case. The very fact that tapering occurs differently suggests that the level of tapering can be

controlled by fragmenting shots in a particular fashion. The upper and lower bounds of tapering angle and length scales are not clear from this first study, but may certainly warrant interest in future work. Figure 4.48 demonstrates how the blur affects the dependence of pore diameter on dose for multiple shot dosing.

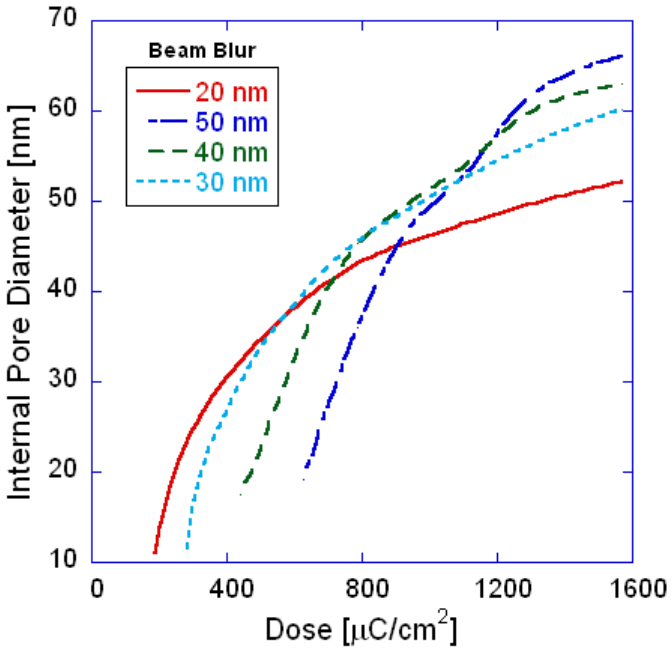

Figure 4.48. Internal pore diameter at a depth of 95 nm in the film (100nm ZEP on 19 nm silicon nitride on silicon) when simulated at beam blur of 20 nm, 30 nm, 40 nm, and 50 nm.

From Figure 4.48, it is seen that the pore size increases with blur over a common range of operating blurs. This is in contrast to the single shot case (Figures 4.19-4.20), where increasing the blur led to an increase and subsequent decrease in pore size. The operating blur was found to be approximately 40 nm by comparing the pore size distribution to experimental values as in previous cases. Figure 4.49 below compares the experimental pore size to the simulated internal pore size at the top and bottom of the pore.

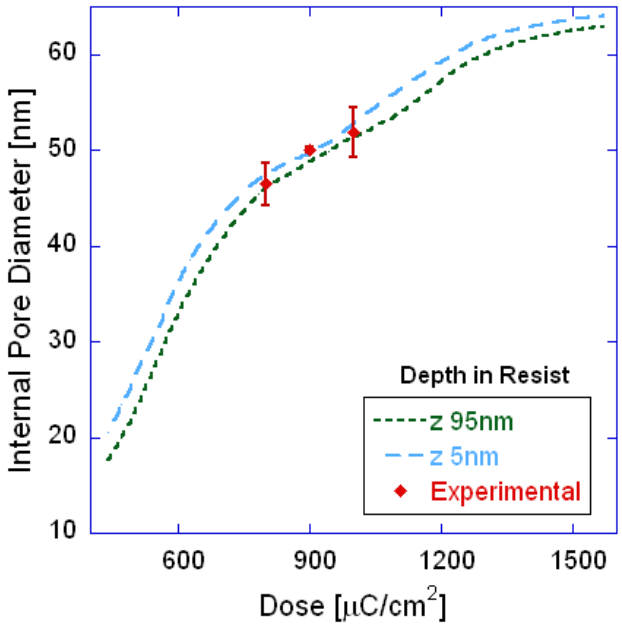

Figure 4.49. Simulated multiple shot pore geometry at a blur of 40 nm versus observed size in SEM for multiple doses in 100nm ZEP on 19nm silicon nitride on silicon

The beam blur of 40 nm closely parallels the beam blur of 35 nm and 39 nm reported earlier for the single shot cases. Figure 4.49 indicates the closest agreement with experimental data reported throughout the simulation studies. This is probably due to the fact that the experimental data in this case was available from isolated pores in silicon nitride. Earlier comparisons between simulations and experiment were made to pores which were patterned with surrounding features.

4.8 Simulating a Single Shot of the Beam at Zero Blur

There is another important recurring trend observed in the simulated pore profiles discussed above. Generally, the internal structure of the pores tends to taper inwards as the depth increases. This may seem counterintuitive to the scattering behavior of electrons – that is, an apparent tendency to disperse inwards instead of outwards. In fact,

the following empirical relationship can be used to estimate the effective *widening* of the electron beam in a resist due to forward scattering [75]:

$$\Delta d = 0.9\left(\frac{t_R}{V_b}\right)^{1.5} \tag{4.54}$$

Here, Δd is the change in beam diameter after entering the resist in [nm], t_R is the resist thickness in [nm], and V_b is the accelerating voltage in [kV]. Applying this equation to our operating conditions (100 nm ZEP, 100 kV) gives an approximate broadening of about 0.9 nm. This is very small, indicating very little tapering of the beam through the resist, but still representative of some outward tapering. To investigate the reason for this apparent discrepancy, we present "theoretical" internal pore geometry of pores dosed by a point source of electrons (an effective beam blur of 0 nm).

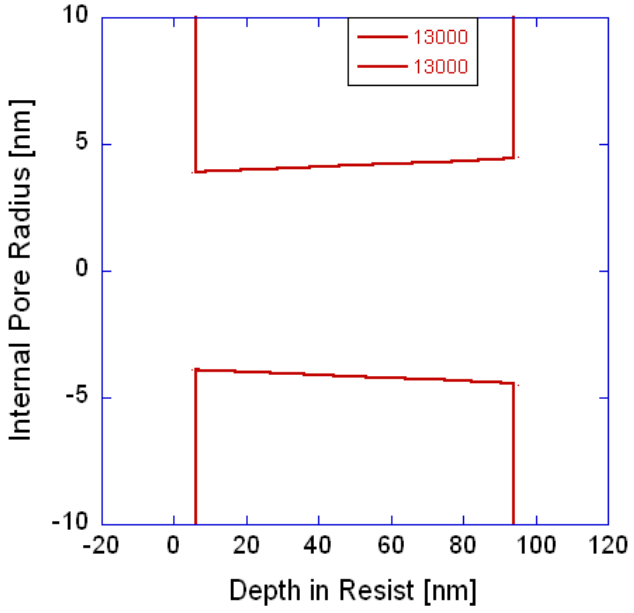

Figure 4.50. Simulated "theoretical" single shot pore geometry by a point source of the beam in 100nm ZEP on silicon at a dose of 13,000 $\mu C/cm^2$

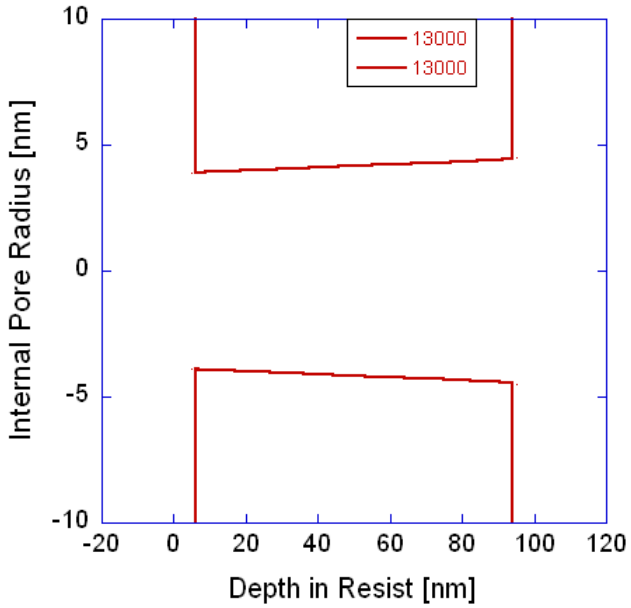

Figure 4.51. Simulated "theoretical" single shot pore geometry by a point source of the beam in 100nm ZEP on 19 nm silicon nitride on silicon at a dose of 13,000 $\mu C/cm^2$

Figures 4.50 and 4.51 respectively illustrate the simulated pore tapering behavior in 100 nm ZEP on silicon and 100 nm ZEP on 19 nm silicon nitride on silicon if the beam entered the film as a point source. Of course, this also implies that we are ignoring all other contributions to the effective process blur. We see that the pore tapering profile in this case tapers outwardly, with a broadening of about 1.2 nm from pore mouth to the bottom in both film configurations.

This result shows that we can attribute the inward tapering behavior observed in earlier sections to the incorporation of the high value of the process blur. The blur spreads the beam out radially, concentrating more energy in the center than at the edges, which effectively deposits the energy in a profile that tends to tapers inwards. This effect competes with forward scattering effects which tend to spread the electrons outward. Due to the thin resist and relatively high accelerating voltage, we found that the forward scattering effects are quite nominal, accounting for only about a 0.9 nm increase in lateral

dimension via Equation (4.54). We postulate that the contribution of the beam blur to shaping the electron distribution in features becomes more important as the feature sizes approach the length scale of the beam blur.

4.9 Conclusions and Recommendations

Simulations of internal pore geometry have provided valuable insights for END fabrication *via* EBL processes. Pore geometry was simulated and analyzed for several combinations of dose, beam blur, substrate, and single shot versus multiple shot dosing. The effects of secondary electron emissions were also studied and found to be the primary contributor to pore tapering. It is therefore recommended that simulated electron PSFs should account for the effects of secondary electrons, especially when modeling the patterning of sub-20 nm features.

The pores in ZEP tapered to varying degrees in the *z*-direction, but the effects were always more notable for the smallest pores and lowest doses in each study. ZEP backed with silicon nitride found to increase tapering with this effect increasing with blur. Tapering was found to increase significantly with beam blur. In all cases, as the blur increased, the resist also became more sensitive to dose. It was found that the operating blur in the experiments was in the range of 35 - 40 nm. It is speculated that the large blur is the result of process effects such as patterning the features in the corner of the subfield. It is therefore recommended that future studies pattern pores at the center of the subfield and compare the pore size distributions to the data here to calculate the intrinsic lowest blur of the tool. This value is expected to be nearly 9.9 nm as measured by the FWHM of the beam intensity. This would provide a tunable range of attainable blurs for the machine. Beam blur may also change with accelerating voltage, which offers another route for tuning this key parameter.

The EBL simulations here not only quantify our understanding of internal structure for ENDs in ZEP. They allow optimization of fabrication parameters to attain a desired feature size and geometry for any combination of substrate and shot pattern. In order to accurately translate patterns from ZEP to silicon nitride, the following three-step approach is therefore recommended:

1. Measure feature size in SEM to obtain operating blur and threshold dose
2. After etching, find the etch depth (z-value) by matching the measured feature size to the simulated internal pore diameter
3. Use the etch ratio and film thickness to construct the internal geometry in the film from the internal geometry in the resist, starting at the z-value for the etch depth.

Using only SEM data, the full internal geometry of the nanopore devices can therefore be mapped.

CHAPTER 5

THIN FILM ISSUES RELEVANT TO NANOPORE FABRICATION

Thin and ultra-thin films are a recurring factor in designing an optimal END fabrication methodology. The first instance requiring thin film growth was in order to produce a short enough channel for a high sensitivity application such as DNA analysis. For DNA, the film thickness should be on the order of magnitude of a single base length. Reports thus far for ENDs have been described in the literature to produce ENDs with channels of length order 10 nm and smaller. Thus, the next benchmark for a wafer scale process is to demonstrate that comparable results are achievable.

The composition of the initial thin film housing the pore is of vital necessity to the integrity of the END as well. The material is required to have high mechanical strength, be stable in solution, and to have the ability to be deposited with high uniformity and a high level of control at very thin thicknesses. The material is also required to have good etch resistance relative to silicon and to survive the other processing steps as well as provide a favorable surface chemistry, in the sense of allowing for functionalization but not over-reactive so as to interfere with measurements or subsequent processing.

Silicon nitride deposited by low pressure chemical vapor deposition was a strong candidate because it met all of these criteria and was also demonstrated to yield good results by similar fabrication methods in the literature. Silicon nitride deposited by plasma enhanced chemical vapor deposition was also considered. PECVD silicon nitride is known to generally exhibit less ideal properties than LPCVD nitride (higher porosity, higher stress, less pure) especially at thin thicknesses but they can be deposited at much lower temperatures which would allow integration of electrodes at an earlier phase in the process. There have also been several works that demonstrate tuning of process

parameters to achieve higher quality PECVD films [76, 77]. However, these works generally do not deal with nitride of the very thin order required here (order 10 nm), nor do they expose the nitride to a produce a free standing structure of the high aspect ratios (100-10,000) described here. Thus, in this work, it was investigated whether ultrathin PECVD silicon nitride or silicon oxide could be compatible with END processing.

The quality of the films was measured quantitatively by ellipsometry and qualitatively by placing the wafers in a bath of 45% potassium hydroxide at 70^{o}C for 15 to 20 minutes. The ellipsometry measurements were taken at 13 points across the wafer and yielded refractive index of each point at two different wavelengths as well as the thickness of the film at each point. This data indicated the film thickness, uniformity, and qualitative information about the stoichiometry of the film composition. Specifically, the measured refractive indices were compared to the refractive index of pure crystalline silicon nitride. Higher values may have indicated a higher concentration of silicon, and lower values may have indicated the presence of oxygen. The presence of oxygen impurities in the film was especially of concern, because this would cause the film to be etched in potassium hydroxide. The qualitative experiment with the potassium hydroxide was used to reveal the presence of defects anywhere on the wafer because the solution would etch into the wafer at the defect sites. This was critical because ellipsometry only measured data at a finite number of points.

The primary benchmark of a film from a quality control standpoint was its ability to withstand the KOH etch step and to yield a large percentage of surviving free standing films following the process.

5.1 PECVD Silicon Oxide Growth

Silicon dioxide deposited by PECVD was performed with precursor gases of silane at 400 sccm and nitrous oxide at 900 sccm at a pressure of 900 mTorr. The power was varied depending on the target film thickness. Lower power was used to produce thinner films due to the lower deposition rate and therefore a higher degree of control. Figure 4.1 shows calibration curves of PECVD deposition of silicon oxide at different power settings.

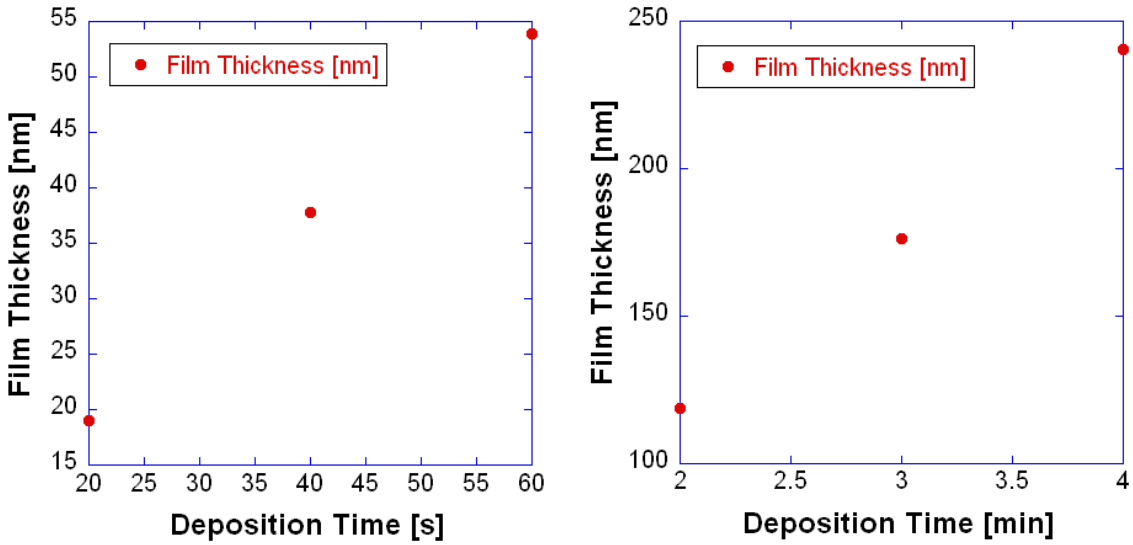

Figure 5.1. Silicon oxide deposition thickness at 20 W (target 50 nm) and 25 W (target 200 nm respectively from left to right.

Silicon oxide deposited by PECVD was found to be easily etched in KOH and was therefore rejected for use in the final process.

5.2 PECVD Silicon Nitride Growth

Silicon nitride deposited by PECVD was performed with precursor gases silane at 4 sccm, ammonia at 5 sccm, and nitrogen gas at 1100 sccm. The pressure was 900 mTorr and the power was 25 W. Figure 5.2 shows calibration curves of the silicon nitride deposition rate. The linearity of deposition was consistent at small and large times.

Silicon nitride deposited by PECVD was found to yield reasonably good uniformity, but several areas of defect caused it to etch away in KOH and it was therefore rejected for use in the final process. This was probably due to the formation of pinholes during the deposition.

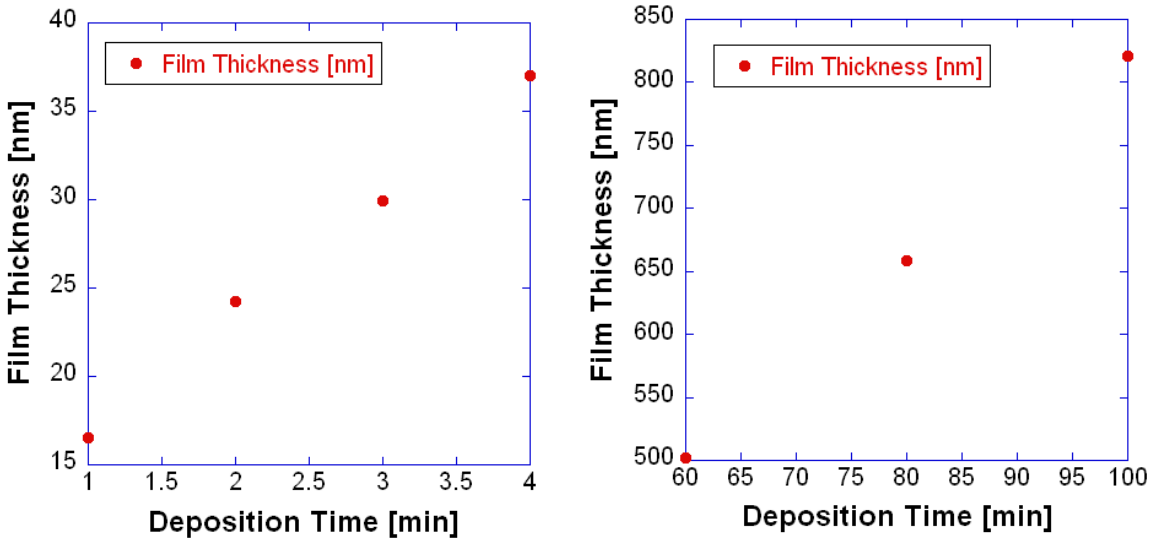

Figure 5.2. Silicon nitride deposition thickness at 25 W (target 20 nm) and 25 W (target 500 nm), respectively from left to right.

5.3 LPCVD Silicon Nitride Growth

Silicon nitride deposited by LPCVD was performed with precursor dichlorosilane at 100 sccm and ammonia at 20 sccm at 800 C. The calibration curve for the deposition rate is shown in Figure 5.3.

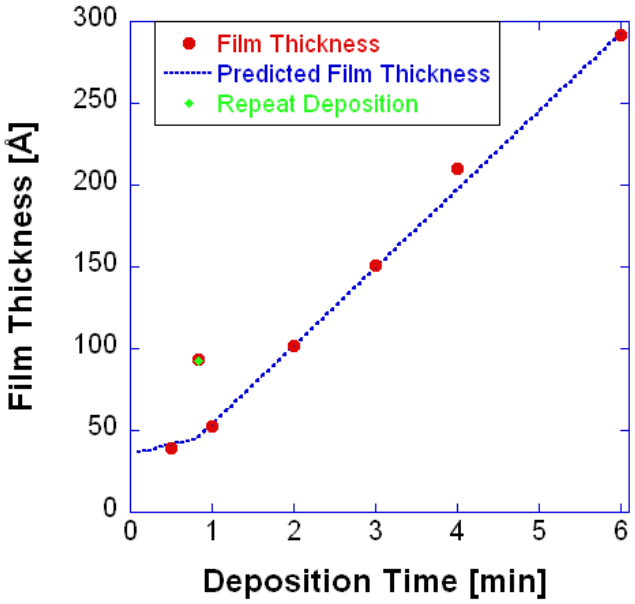

Figure 5.3. Piecewise linear calibration curve of LPCVD silicon nitride deposition rate accompanied with experimental data points

In Figure 5.3, the 5 nm and 10 nm films with deposition times of 30 seconds and 1 minute respectively did not survive the KOH immersion test. In an attempt to produce a better quality 10 nm film, one wafer was placed in the furnace for 2 consecutive deposition cycles, the first for 30 seconds and the second for 20 seconds (a common practice to reducing defects such as pinholes, especially in PECVD films). The result (the outlying point in Figure 5.3) revealed an extraneous parameter in the film growth which may be empirical. Although the growth appeared linear at deposition times greater than 1 minute, in the case of the repeat deposition the sample experienced nearly twice the expected deposition rate.

In developing the model for the calibration curve, it was speculated that there are two mechanisms contributing to this result. The first is continued reaction after the programmed reaction time is over. This may occur within the boundary layer at the surface while the bulk reactants are purged out of the chamber. The result is an effectively longer deposition time. The second is a dampened deposition rate for reaction

times on the order of 10 seconds and smaller. The reaction may be slower at very early reaction times because of unsteady state and disparity of the reaction surface (silicon at time zero versus silicon nitride as deposition progresses). The experimental data indicates a highly linear behavior from approximately 1 minute to 6 minutes. Therefore, a piecewise linear approach was applied to modeling deposition behavior and the following parameters were defined: early growth rate r_{Si}, late growth rate r_n, additional film growth A, and threshold thickness T_t. T_p is predicted film thickness and t is time. The model is as follows:

For $t \leq \frac{T_t}{r_{Si}}$ (low deposition times),

$$T_p = t r_{Si} + A \tag{5.1}$$

For $t > \frac{T_t}{r_{Si}}$ (high deposition times),

$$T_p = T_t + r_n \left(t - \frac{T_t}{r_{Si}} \right) + A \tag{5.2}$$

Fitting the experimental in the higher range of time gives r_n = 47.8 Å/min and

$$A = 5.71 - T_t \left(1 - \frac{47.8}{r_{Si}} \right) \tag{5.3}$$

Therefore, there were two independent fit parameters r_{Si} and T_t remaining which were best fit to reduce the standard deviation from experimental data. The results were T_t = 10 Å, r_{Si} = 12.1 Å/min, and A = 35.2 Å. As a preliminary analysis, the results match well with the limited experimental data set. It is recommended that further experimental data be produced at short deposition times and with several repeated trails to develop a detailed process characterization. The goal of this analysis is towards reliable ultrathin silicon nitride membranes in the sub-10 nm range. The effects of "excessive deposition" may be controlled by reducing gas flow rates to generally achieve a more controlled deposition rate in the sub-10 nm growth regime. This would certainly be the next step in routinely achieving the single nanometer channels required for high resolution END analysis.

Figure 5.4 below shows the corresponding refractive index of good quality films of silicon nitride deposited by LPCVD in a consecutive series of deposition steps in the furnace (which was empirically found to give the most consistent results). These films were exposed to 45% KOH at 60-70 C for 30 minutes and found to yield no defects.

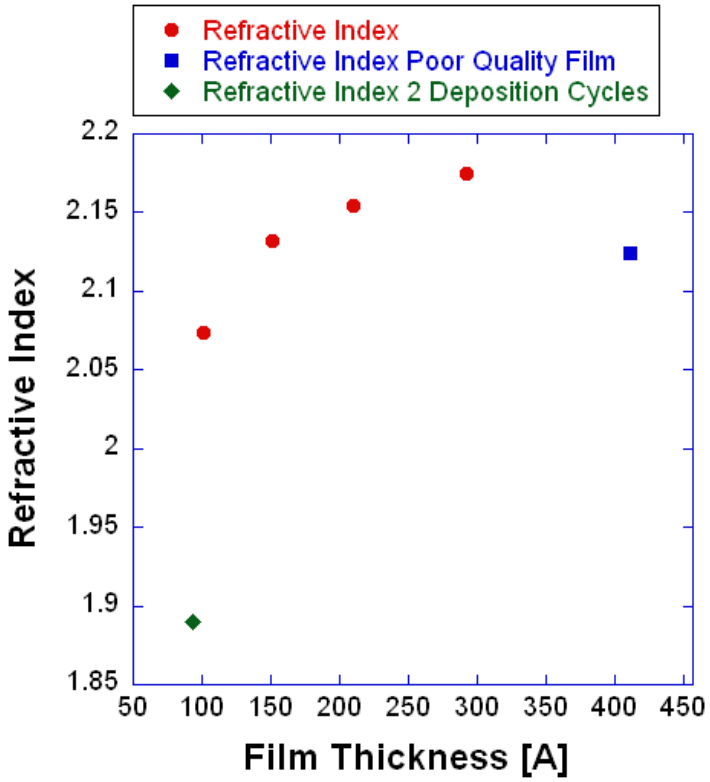

Figure 5.4. Refractive Index of High Quality LPCVD Silicon Nitride at Different Thicknesses.

Here, again it is noted that the first point represents a film deposited in 2 distinct LPCVD cycles of 30 seconds followed by 20 seconds. The final point represents a wafer that failed the KOH immersion test and therefore was classified as a poor quality film in the context of END application.

The refractive index can be used not only to provide general qualitative insights about film quality, but also to extract important specific details about the film composition. This is because of its dependence on fundamental material properties such as atomic density and dielectric constant [78-81], which can be used to determine stoichiometry. In fact, stoichiometry of silicon nitride films deposited by CVD has been well characterized by ellipsometry and confirmed by X-ray photoelectron spectroscopy, Fourier transform infrared spectroscopy, and high resolution transmission electron microscopy [80, 82].

From Figure 5.4, we observe a definite trend in the refractive index corresponding to a shift in stoichiometry from stoichiometric silicon nitride to silicon rich species at larger film thicknesses. This may be an impact of the effect described earlier that was responsible for the unexpectedly high thickness of the 100 Å film, i.e. residual film growth at the end of the process. Another qualitative observation is that the wafer of poor quality clearly strays from the trend, which may be due to oxygen contamination or a large number of defects in the film. It is also interesting that the 100 Å film drops significantly in refractive index (seemingly indicating oxide contamination), yet it survived KOH immersion. In all cases, a film that was able to survive KOH immersion was also able to yield a significant number of mechanically stable films following the back etch.

To better understand and further investigate the variations in Figure 5.4, it is useful to calculate the stoichiometry of the films from the refractive index. This allows us to quantify the relationship between the measured refractive index and film quality, and also provides insight into the early stages of the film deposition. We employ the Clausius-Mossoti model [79, 80] for a material that can be polarized by an electric field:

$$\frac{\epsilon-1}{\epsilon+2} = \frac{4\pi}{3} n\alpha \tag{5.4}$$

where ε is the material dielectric constant, *n* is volume density, and α is the polarizability. A similar relationship can also be derived for a heterogeneous composite of two phases with individual polarizabilities α_A and α_B [80]:

$$\frac{\epsilon-1}{\epsilon+2} = \frac{4\pi}{3} (n_A \alpha_A + n_B \alpha_B) \tag{5.5}$$

Combining the above two expressions gives the Lorentz-Lorentz equation, which relates the dielectric constant of a composite to the dielectric constant of the pure components weighted by volume fraction *f*:

$$\frac{\epsilon-1}{\epsilon+2} = f_A \frac{\epsilon_A-1}{\epsilon_A+2} + f_B \frac{\epsilon_B-1}{\epsilon_B+2} \tag{5.6}$$

The dielectric constant can be rewritten in terms of refractive index *n* and absorption coefficient *k*, as $\epsilon = (n - ik)^2$. It is assumed that *k* << *n*. This is a reasonable assumption as evinced by ellipsometry measurements, which show that the absorption coefficient of Si_xN_y is negligible in the photon wavelength range of interest [80]. This allows the volume fraction of each component to be calculated:

$$f_A = \frac{2n^4 + n^2(n_A^2 - 2n_B^2) - n_A^2 n_B^2}{3n^2(n_A^2 - n_B^2)} \tag{5.7}$$

$$f_B = \frac{2n^4 + n^2(n_B^2 - 2n_A^2) - n_B^2 n_A^2}{3n^2(n_B^2 - n_A^2)} \tag{5.8}$$

For silicon (component A) and silicon nitride (component B), the stoichiometry of the film can then be expressed as:

$$\frac{N}{Si}\ Ratio = \frac{f_{Si3N4}[N]_{Si3n4}}{f_{a-Si}[Si]_{a-Si}+f_{Si3N4}[Si]_{Si3N4}} \tag{5.9}$$

The concentrations of nitrogen in silicon nitride, silicon in amorphous silicon, and silicon into silicon nitride were obtained from the literature [80]:

$$[Si]_{a-Si} = 5 \times 10^{22}\,\frac{atoms}{cm^3}$$

$$[Si]_{Si3N4} = 3.6 \times 10^{22}\,\frac{atoms}{cm^3}$$

$$[N]_{Si3N4} = 4.8 \times 10^{22}\,\frac{atoms}{cm^3}$$

Figure 5.5 demonstrates the stoichiometric ratio as a function of film thickness.

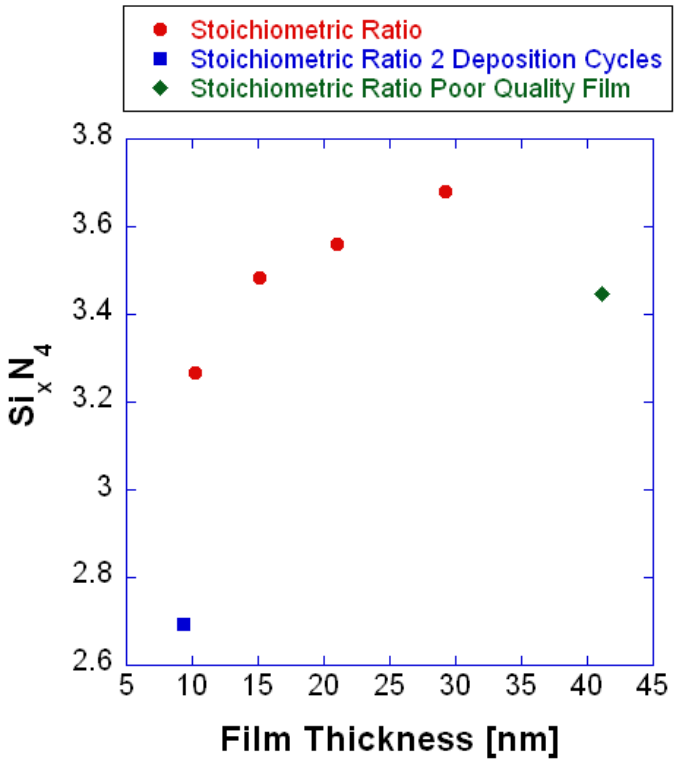

Figure 5.5. Stoichiometric ratio of silicon nitride as a function of film thickness

It is important to note that the model assumes a negligible concentration of impurities in the film. This is a reasonable assumption of the wafers which survived the KOH immersion test because any defects are quickly attacked and dissolved. The data point indicated in green, on the other hand, represents a wafer which failed the KOH immersion test. Therefore, this wafer may have had some oxygen contamination (e.g., due to a leak in the chamber) or other defect which caused it to stray from the trend of the surviving films. For this case, the true stoichiometry is unclear and more detailed analyses such as XPS would be necessary to determine the composition and stoichiometry. Nonetheless, from a quality control standpoint there is a distinct correlation between pure predicted stoichiometry and wafer integrity. In other words, the initial results indicate that the quality of the wafers (i.e. survivability in KOH immersion) can be predicted by the refractive index data.

There is another factor which warrants discussion here. In general, LPCVD deposited silicon nitride stoichiometry / refractive index has been reported as a function of reactant ratios and temperature, not as a function of film thickness [82-84]. Nonetheless, the refractive index measured in the thickest film agrees closely with the literature at the same deposition conditions [84]. This gives further credence to the possibility that there is a different mechanism at work early on in the reaction. It is well documented that the stoichiometry of the silicon nitride is controlled by the ratio of the reactants [84, 85]. The stoichiometric reaction can be summarized as:

$$3SiH_2Cl_{2\,(g)} + 4NH_{3\,(g)} \rightarrow Si_3N_{4\,(s)} + 6HCl_{(g)} + 6H_{2\,(g)} \qquad (5.10)$$

It is also clear that the film stoichiometry is strongly influenced by the availability of reactants at the surface. The observed dependence of stoichiometry on film thickness may therefore be due to the initial conditions in the chamber during which the reaction is at an unsteady state. The first step in the reaction is a gas stabilization phase in which ammonia is flowing but dichlorosilane is not. As the dichlorosilane is introduced it must diffuse through the boundary layer at the surface of the wafer (which is at this point purely ammonia) and adsorb to the surface itself. Thus, there is a period during which there is a steadily increasing flux of dichlorosilane to the surface. This is shown in Figure 5.6.

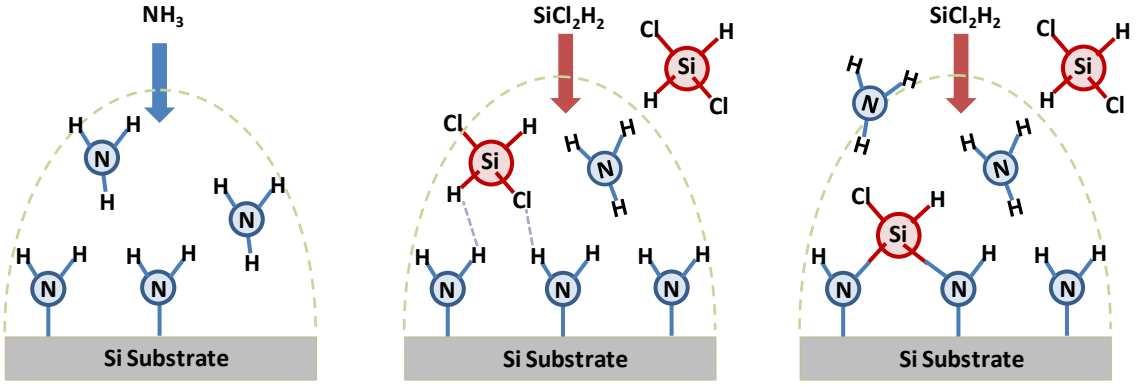

Figure 5.6. Diffusion-limited reaction in the early stages of Silicon Nitride LPCVD.

During this phase, the nitride deposited is relatively silicon-poor, even dipping below the silicon content of stoichiometric nitride in one case in Figure 5.5. This is very probably due to the creation of atomic voids or other imperfections in the film. These defects cannot be due to pinholes or oxygen contamination, because they would appear rapidly during KOH immersion. The above considerations also explain the sharp difference in stoichiometry between the first two data points in Figure 5.5. The wafer deposited in two cycles experienced this effect of limited dichlorosilane surface diffusion twofold. Nonetheless, the trend of the wafers which underwent single stage depositions is clear and well characterized. By the latter end of the growth (300s) the nitride approaches a steady stoichiometry of 3.4-3.5 in silicon, and constitutes a relatively low stress (<200 MPa from [84]) silicon-rich species.

To investigate the effects of boundary layer diffusion, the time required for dichlorosilane to diffuse through the boundary layer can be roughly estimated by

$$t \sim \frac{\delta^2}{D_{AB}} \tag{5.11}$$

where δ is the boundary layer thickness and D_{AB} is the diffusivity of dichlorosilane in ammonia. The diffusivity was calculated from the following semiempirical relationship [86]

$$D_{AB} = \frac{1.0\times10^{-9}T^{1.75}}{P\left[(\sum v)_A^{1/3}+(\sum v)_B^{1/3}\right]^2}\left(\frac{1}{M_A}+\frac{1}{M_B}\right)^{1/2} \tag{5.12}$$

In this equation, *A* represents dichlorosilane, *B* represents ammonia, D_{AB} has units of [m^2/s], *T* is temperature in [K], *P* is pressure in [atm], Σv is the sum of the atomic volumes of all elements in each molecule in [m^3/kgmol], and M_A and M_B are the molecular weights of dichlorosilane and ammonia respectively in [kg/kgmol]. The diffusivity at the reaction temperature of 800 C (1073 K) was calculated by (5.12) to be 0.355 m^2/s. Next, the boundary layer thickness was estimated from

$$\delta = \frac{x}{\sqrt{Re}} \tag{5.13}$$

where *x* is the characteristic length scale (wafer diameter) and *Re* is Reynolds number of the dichlorosilane. The Reynolds number was calculated by definition

$$Re = \frac{\rho v d}{\mu} \tag{5.14}$$

where ρ is the density, *v* is the velocity, *d* is the characteristic length scale (diameter of the reaction tube), and μ is the viscosity. The Reynolds number was calculated to be 0.4, well within the regime of laminar flow, and the corresponding boundary layer thickness was 0.16 m. Thus, the time to diffuse through the boundary layer was estimated from (5.11) to be 0.07 s. Although this result suggests that boundary layer diffusion is fast and unlikely to be a limiting factor, it is important to recall that the calculations assume that the bulk flow over the wafer is well developed. In order to determine how quickly the

chamber may fill with the reactants, the residence time of the system was calculated by the following relation.

$$\tau \sim \frac{V}{q} \tag{5.15}$$

where V is the volume of the reactor and q is the volumetric flow rate of the reactants. The system residence time was calculated to be 456 minutes, which seems very high until the context of the reaction is considered. For thin film growth of silicon nitride the process has been semi-empirically optimized to achieve a balance of uniform deposition on the substrate while reducing reactions in the bulk gas phase. The process relies on surface adsorption and reaction and is in fact undermined by a large number of collisions in the bulk. The regime in which this is possible is of low flow rate, low pressure, and high temperature. The trade off is that the deposition rate is very slow, but well controlled to nearly nanometer rates.

To demonstrate the final process step and investigate the survival rate of the devices, several wafers were etched to the silicon nitride, thus exposing the free standing films each containing a nanopore. Two examples of optical micrographs of free-standing films are given in Figure 5.7. The aspect ratios (length:thickness) of the free-standing surfaces in Figure 5.7a-b are 1,000 and 19,750 respectively, demonstrating the high mechanical strength of the thin films. Larger windows such as those in Figure 5.6b exhibit ripple-like effects in the optical images, which are evidence of the mechanical stresses in the LPCVD silicon nitride. This behavior was only visible optically in the highest aspect-ratio films, and is not observed in Figure 5.7a.

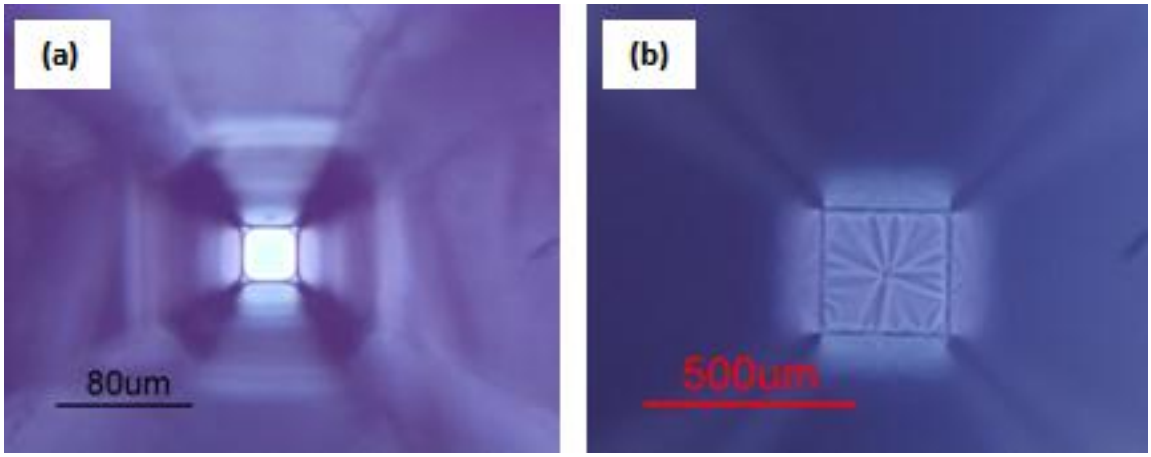

Figure 5.7. Optical micrographs of: (a) a 30 μm window exposing a 30 nm thin silicon nitride film, and (b) a 300 μm window exposing a 16 nm silicon nitride film. Each film contains a single nanopore.

The survival rate of devices following the KOH wet etch was determined by optical microscopy of *every device on each wafer*. The best results were obtained for wafers containing 50 nm free-standing films with 60-80 μm windows. Figure 5.8 shows examples of these films. A survival rate of 903 out of 940 devices, or 96% across the wafer, was achieved. Devices at the edges of the wafer were included in the analysis. For the case of the 16 nm films over 200-500 μm windows, the survival rate was 15%. This indicates that further optimization of the window dimensions for ultra-thin films is necessary. The aspect ratio was likely too large to allow the films to withstand the mechanical stresses arising from the KOH etching process.

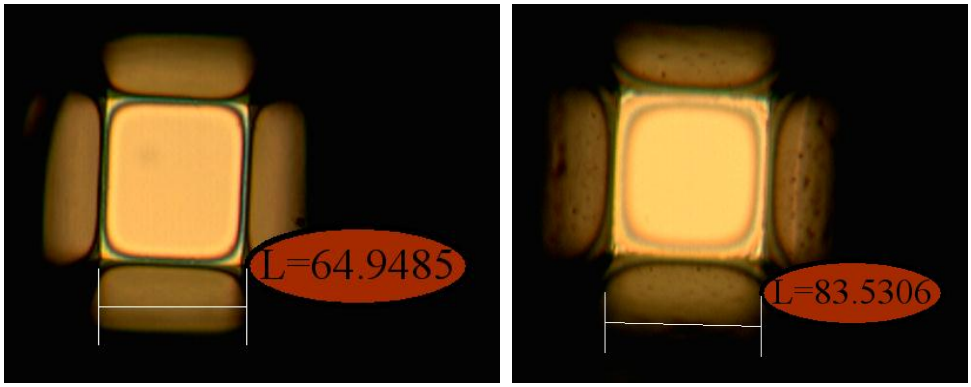

Figure 5.8. Optical images of two devices (50 nm silicon nitride) after backside wet etch. The window dimensions shown are in microns.

In one case, a sample was etched in inductively coupled plasma following the backside wet etch in order to reduce the channel length of the END. The nitride film was successfully reduced in thickness by approximately a factor of 2. This is shown in Figure 5.9.

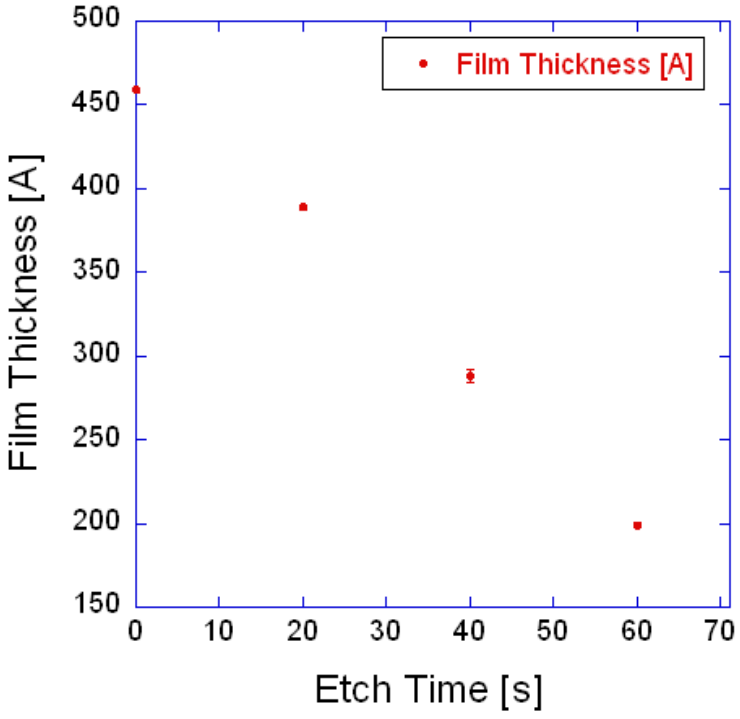

Figure 5.9. A free standing silicon nitride film after etching in ICP for 20 second intervals.

This result shows the potential for tuning channel length in ENDs on the wafer scale in a manner similar to tuning the pore size by atomic layer deposition. Reducing RF power and gas flows would allow for slower and therefore more controlled etching at the sub-10 nm level.

5.4 Atomic Layer Deposition of Aluminum Oxide

Atomic layer deposition (ALD) is a wafer scale deposition process that deposits a single molecular layer at a time. The mechanism pulses reactants and purges the chamber in sequence to produce the film. ALD was used to tune the pore size further following EBL. The objective of ALD is to demonstrate that the ENDs can be tuned down in size from order 10 nm to order 1nm, thus bridging the gap in resolution between EBL and TEM. ALD [87, 88] of aluminum oxide was performed on the nanopore arrays following their fabrication in order to tune the size of the pores. Up to 215 ALD cycles were performed. Figure 4.9 shows the measured pore size as a function of the number of cycles, for two pores of initial size 38 nm and 45 nm respectively. Figure 5.10 also shows the average pore size reduction of 25 pores on a wafer that underwent ALD.

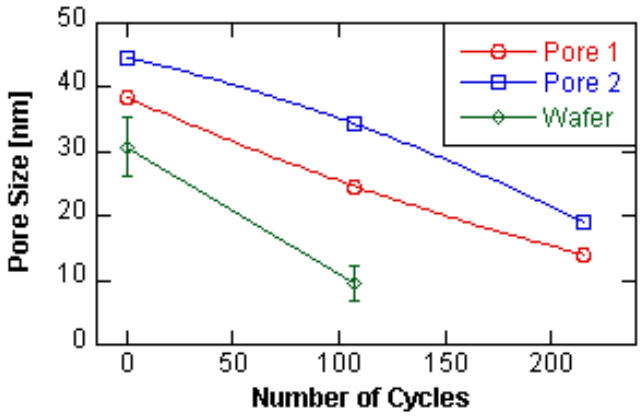

Figure 5.10. Nanopore size as a function of number of ALD cycles for two pores and an entire wafer. The curves are only a guide to the eye.

For the two individual pores, the aluminum oxide deposition rate (and hence the rate of pore size shrinkage) is nearly linear, with an average deposition rate of 0.58 Å Al_2O_3 per cycle. The nanopore diameters were successfully downsized to 20 nm and smaller. Figure 5.10 also clearly indicates that the pore size can be easily scaled below 20 nm by additional ALD cycling (as demonstrated by other authors with individual nanopores [89], and also suggested by Figure 5.9). However, once these pores were sized below 20 nm, their sizes could not be clearly measured by SEM. Figure 5.11 shows SEM images of a nanopore at different stages of ALD processing. By the last set of cycles the pore has been very nearly closed.

Under the same conditions, a wafer containing 25 pores also underwent ALD for 107 cycles. The pores on this wafer were initially of size 30 nm. As the 10 nm and smaller pore size was approached with ALD, it was expected that two effects would become more and more prominent in influencing the deposition rate. Due to the intrinsic internal pore geometry, if the rate of volume deposited remained constant, the pore size would shrink faster over time. On the other hand, pore sizes on the nanoscale may begin to cause limited diffusion and flux of precursor gases along the pore's internal surface, thus reducing the deposition rate. It is quite possible that both of these effects were competing as the pores in the wafer approach the sub-10 nm range. The average deposition rate observed on the wafer was 0.9 Å Al_2O_3 per cycle, which is higher than the rate of the individual pores. Figure 5.10 provides the average pore size shrinkage and Figure 5.11 below provides SEM data of one of the pores following ALD. Figure 5.12 provides SEM detail of one of the nanopores tuned to the 10 nm range by wafer scale ALD.

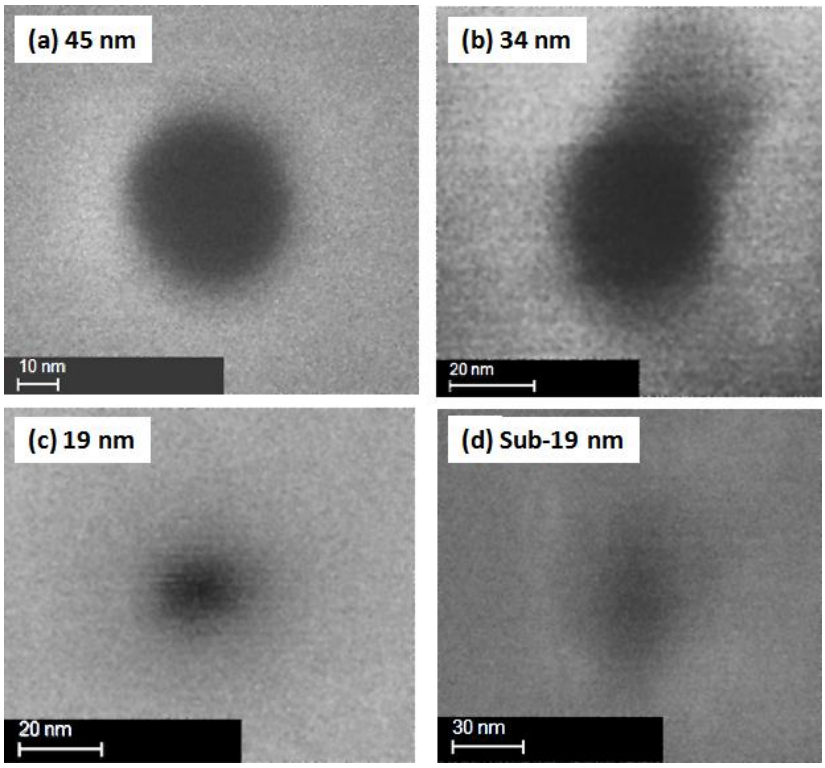

Figure 5.11. SEM images of a single nanopore undergoing ALD cycles as shown in Figure 5.10 (Pore 2). The nanopore size is reduced in a controlled manner and with nanometer scale precision.

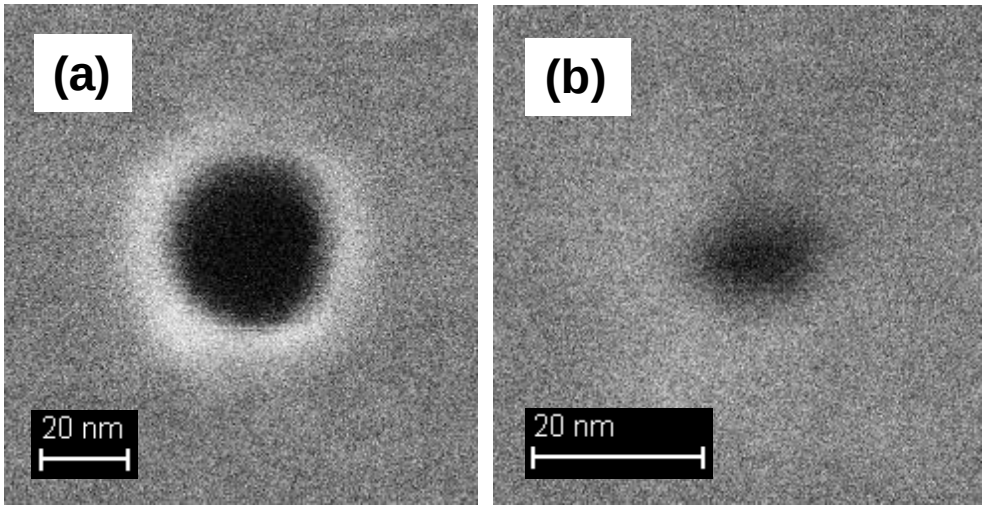

Figure 5.12. SEM images of a nanopore (a) initially and (b) following ALD for 100 cycles.

5.5 Conclusions and Recommendations

LPCVD silicon nitride was found to exhibit the mechanical strength required to yield high survival rates following KOH etch. It was reproducibly deposited at thicknesses of 50 nm down to 10 nm and thinner, retaining bulk chemical stability with regard to KOH, i.e. without defects, pinholes, or stoichiometric deficiencies. The highest aspect ratio achieved with high survival rate was of order 10,000. Therefore, as long as the material can be deposited without these defects and still retains bulk material properties, ENDs can be scaled down to a channel length of just a few nanometers over an order 10 micron window. The thinnest films produced that demonstrated good quality by immersion in KOH was 9 nm. 5 nm films deposited in a single run did not survive the immersion test in KOH. However, it was demonstrated that multiple consecutive deposition steps allows for films in the sub-10 nm thickness. Coupled with reduced precursor flow rates, surely thinner chemically and mechanically stable films can be achieved. Atomic layer deposition was demonstrated to scale down a wafer of ENDs by a factor of 3. Smaller features were more difficult to determine with certainty the size and quality of the ENDs in SEM. It may be an instance where TEM would be useful to confirm that the process can be extrapolated to the sub 10 nm range. Nonetheless, it is clear that ALD is capable of scaling features down effectively, reproducibly, and on the nanoscale.

CHAPTER 6

NANOPORE CONDUCTANCE MEASUREMENTS

In this chapter, we describe our efforts to construct and test an apparatus for conductance measurements from our nanopore devices. Whereas the array of ENDs would ultimately be operated using microfabricated "on-chip" electronics, it is first necessary to be able to test the ENDs individually in order to study in detail the transport of ions and biomolecules through them and draw structure-property correlations. Although this task proved to be quite challenging, we were able to make preliminary progress and show the successful conductance characterization of a nanopore.

6.1 Measurement Setup and Theory

The conductance measurement apparatus consists of computer, digitizer, amplifier, electrodes, and conductance chamber. A flow diagram and photographs of the apparatus are shown in Figure 6.1. The electrodes are placed in the opposing reservoirs of the chamber, between which lies the END. From here they are fed into the Axon Instruments CV203BU Headstage (electrode holder). The signal is transferred to the Axon Instruments Axopatch 200B Integrating Patch Clamp for amplification. Finally, the amplified signal is converted to a digital signal for recording by the digitizer Axon Instruments Digidata 1322A 16-Bit Data Acquisition System. The conductance chamber sits on a vibration isolation table and within a Faraday cage to reduce mechanical and electromagnetic disturbances. This configuration allows for optimal noise reduction. The electronics are controlled by the software PClamp from Axon Laboratories. The software allows the user to apply any combination of step and/or ramp voltage inputs to the system over the measurement timescale while monitoring the ionic current.

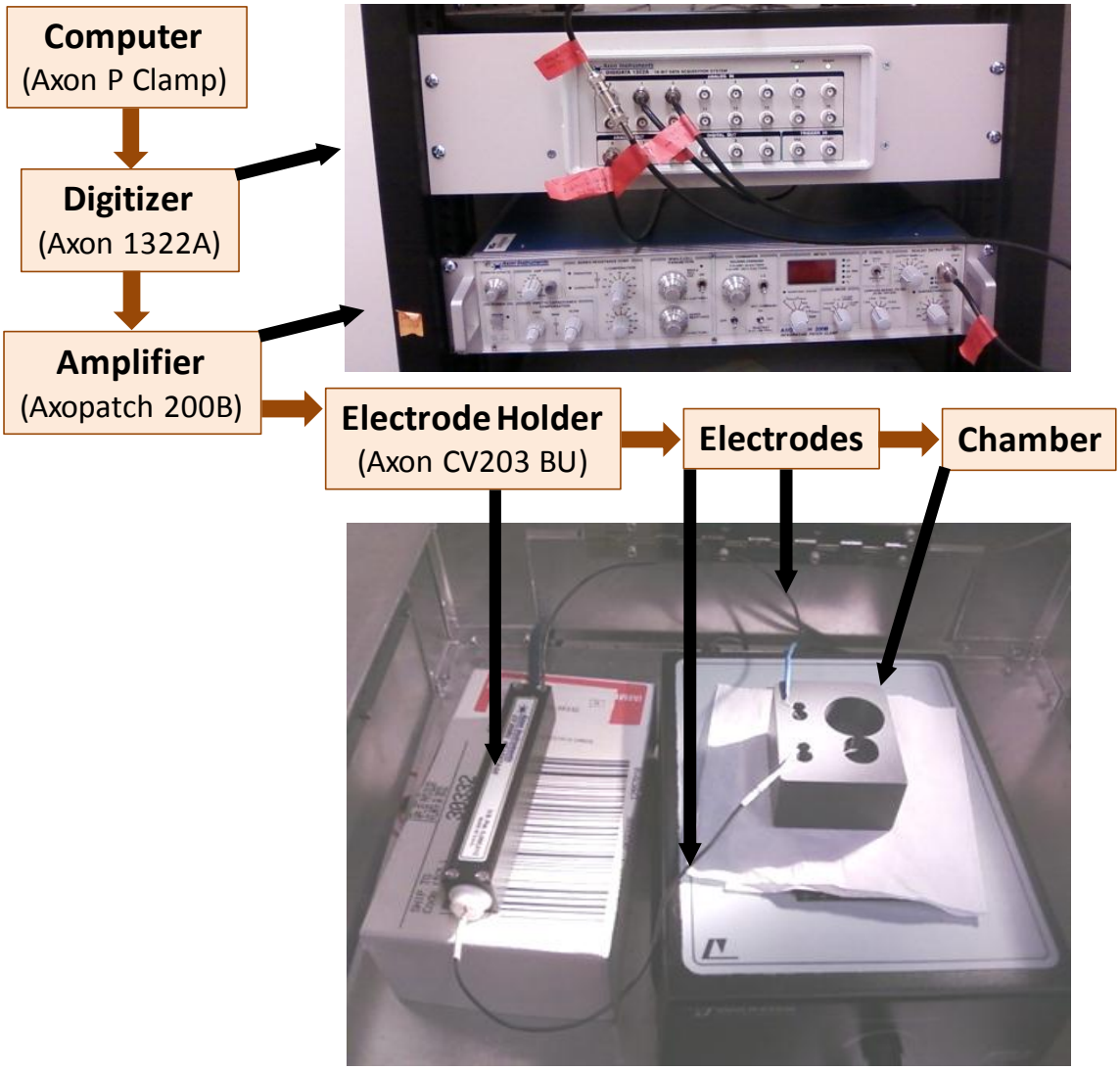

Figure 6.1. Conductance Measurement Experiment Apparatus and Flowchart

The conductance apparatus with the mounted sample is modeled as a series resistance problem. A series of voltage steps are applied to the system and the resulting current is measured. The resistance is calculated by Ohm's Law:

$$R = \frac{V}{I} \tag{6.1}$$

The total Ohmic resistance is the sum of two components: the intrinsic resistance of the chamber (R_0), and the resistance through the sample (R_{sample}). The intrinsic resistance of the chamber R_0 is determined by measuring conductance across the chamber with no sample mounted. When the sample is mounted, the resistance measured is the total resistance of both the chamber and the sample, R_T; and the resistance of the sample can thus be easily determined, i.e.

$$R_{sample} = R_T - R_0 \tag{6.2}$$

The resistance R_{sample} can be split into the resistance through each segment of the sample, namely the relatively large 57^o trench leading up to the surface containing the pore, and the thin membrane containing the pore itself. The basic expression for resistance through a medium can be expressed as:

$$R = \rho \frac{l}{A} \tag{6.3}$$

where ρ is resistivity, l is length, and A is cross sectional area. In an END chip, the resistance in the silicon trench is discretized and calculated by summing many consecutively smaller regions to simulate tapering. Resistance in the pore is calculated by assuming a cylindrical shape and constant diameter throughout. The length parameter in equation 6.3 is simply the silicon nitride film thickness. The resistivity of the solution (150 mM KCl at room temperature) is 80 Ω cm.

6.2 Experimental Apparatus and Challenges

Developing and modifying a chamber for conductance measurements was not a trivial undertaking. On a wafer, ENDs were packed as closely as possible for high

throughput. Following dicing, a single nanopore device was obtained in a 2.47 mm square silicon piece. Although we produced nearly 1,000 such devices per wafer, the characterization of an individual device posed unique issues in handling and mounting. The first conductance chamber was designed for easy swapping of devices by employing multiple interchangeable components: the chamber housing, a rubber seal which fit between the two chambers, and multiple END carriers, each of which was notched out to the size of the ENDs and could be slid between the two chambers. This is shown in Figure 6.2 below.

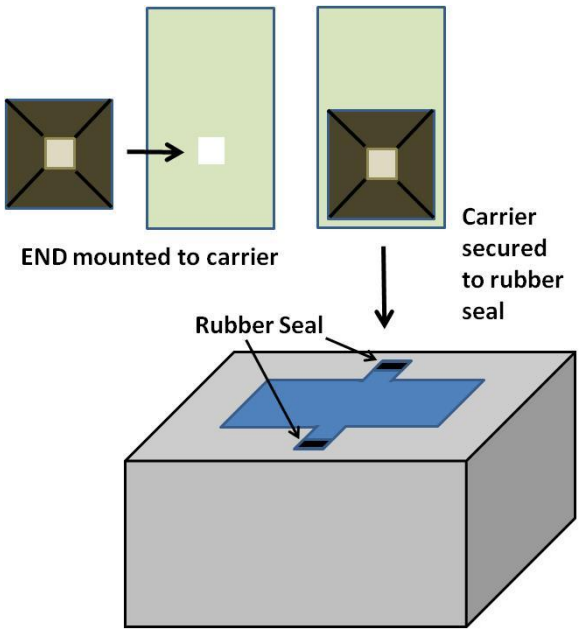

Figure 6.2. Nanopore conductance chamber using carrier and rubber seal configuration.

Unfortunately, measurements in this chamber yielded inconsistent results, due to the presence of leaks which were difficult to pinpoint and seal properly. There were also difficulties arising from the friction between the carrier and the rubber seal. Fine manipulations necessary to handle the delicate devices were not easily achieved. As a result, the devices would often become dislodged, thereby breaking the film or requiring a reassessment of the film's integrity. Due to these issues, a different system was

constructed, that integrated fewer separable components and secured the nanopore devices more effectively. This is shown in Figure 6.3.

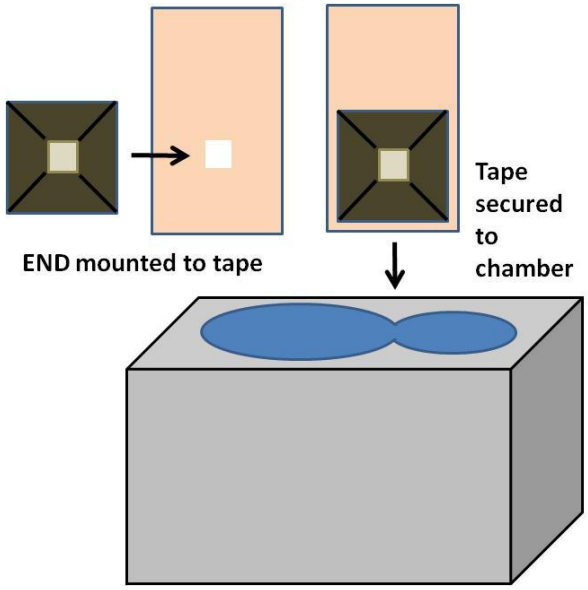

Figure 6.3. Nanopore conductance chamber using waterproof tape and silicon grease.

In this type of conductance chamber, there are two primary changes over the previously considered apparatus. First, the rubber seal between the chamber and the carrier is replaced with a waterproof tape to seal this gap. Second, the tape intrinsically also provides a partial seal to the END upon mounting. As will be demonstrated, this chamber and method of mounting the samples was found to exhibit far more consistent behavior.

6.3 Analysis of a 1-μm Diameter Pore

To initially test the functionality and precision of the system, a 1 μm pore produced by FIB was initially mounted to the conductance apparatus. Increasing voltage steps of 0.05 mV were applied at 0.4 second intervals across the pore and the resulting current response is shown in Figure 6.4.

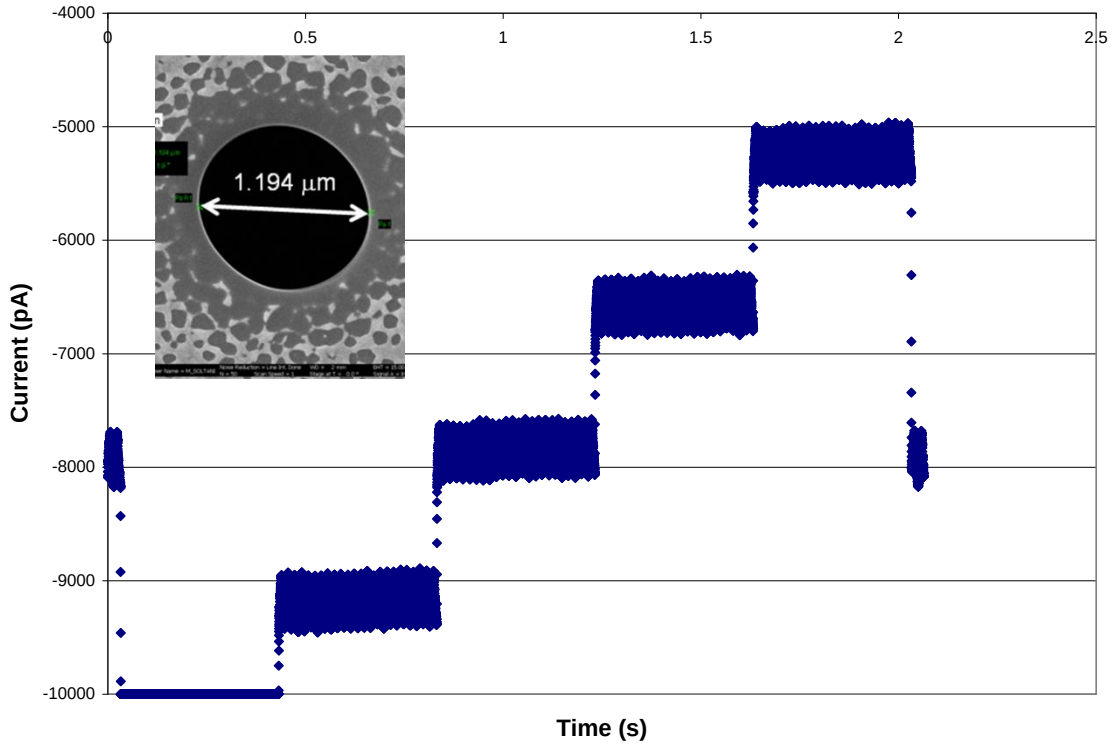

Figure 6.4. Conductance data from a 1.2 micron pore (SEM inset) undergoing 0.05 mV voltage steps.

Furthermore, Figure 6.5 shows that the V-I plot is linear, thereby allowing us to back out the resistance.

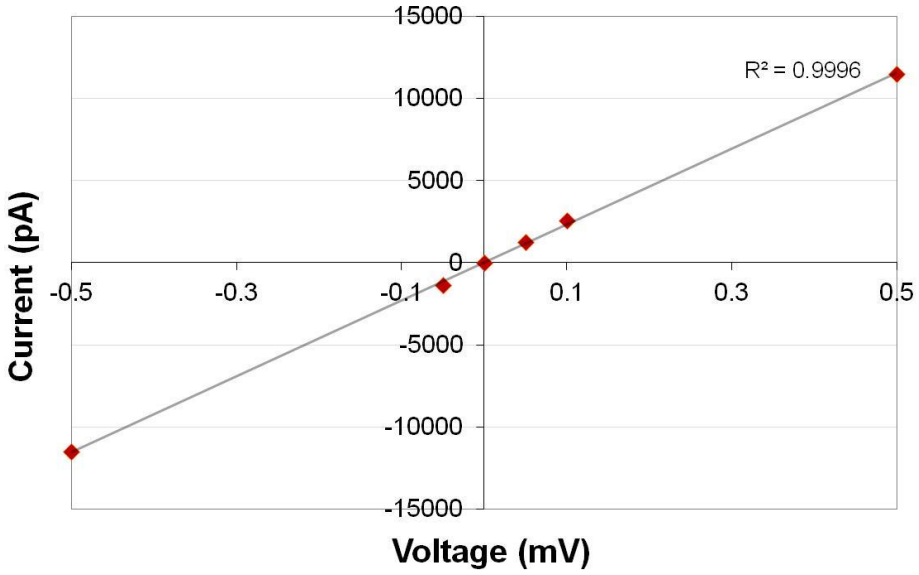

Figure 6.5. V-I Diagram of 1 micron pore at several voltage steps.

The measured resistance of the system was R = 0.05 mV / 1300 pA = 38,462 Ω. This includes the resistances of the chamber, the silicon trench, and the nanopore itself. The resistance of the chamber was experimentally determined by measuring the current and voltage of the chamber with no chip mounted. The measured current was greater than 20,000 pA in response to a step of only 0.01 mV. Thus, the chamber resistance was determined to be less than 500 Ω. This is consistent with similar studies which reported a chamber resistance of ~100 Ω [24]. Because this is two orders of magnitude smaller than the measured resistance, it has a negligible impact. Next, the resistance in the trench was calculated. To do so, the trench was assumed to have a square cross sectional area at every point and to decrease in size at a constant rate from its mouth to the substrate surface. The initial opening of the trench was about 680 μm and the final opening at the surface containing the pore was 90 μm. The trench was broken down into a series of 1 μm long square ducts of continuously decreasing size. This is shown in Figure 6.6.

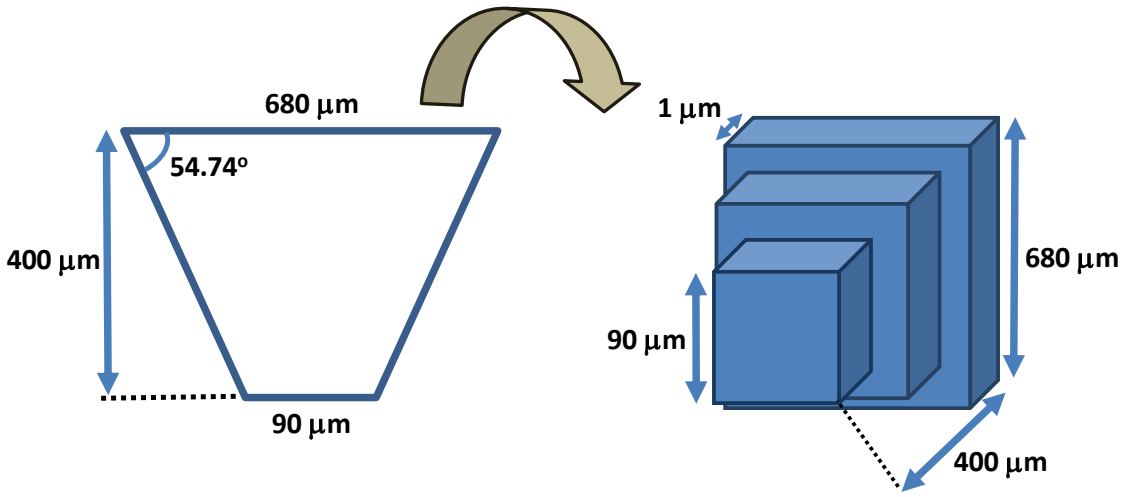

Figure 6.6. Geometric approximation for modeling the ionic current through a silicon trench etched in KOH.

The resistance of each square duct was calculated using equation 6.3 and the total resistance through the chamber was calculated by summing these values. The result was a resistance of 1,749 Ω. This was subtracted from the total resistance of the sample to give the resistance in the pore to be 36,712 Ω. To calculate the pore size, Equation 6.3 was rearranged for the pore diameter:

$$d = 2\sqrt{\frac{l\rho}{\pi R}} \tag{6.4}$$

The channel length (film thickness) l = 80 nm, resistivity ρ = 80 Ω cm, and resistance R = 36,712 Ω. The pore size calculated from Equation 6.4 is 1.49 µm, which is close to, but somewhat larger than, the expected pore size (1.2 µm) from SEM imaging. This is probably due to the FIB sputtering the surface outside of the designated pore pattern. Due to its relative inaccuracy, it is not uncommon for extraneous features to appear well outside of the programmed areas. This is apparent at a qualitative level in the SEM data, but the conductance results indicate an effectively 25% larger pore than intended.

6.4 Conductance Leak Tests

To ensure the validity of the conductance results, one requires a rigorous protocol for development and reproducibility of measurements. The first step was ensuring that the devices could be mounted without exhibiting extraneous conductance readings. There were two areas of contact which were examined: the mounting of the tape to the chamber and the mounting of the END chip to the tape. To determine the integrity of the seal between the tape and the chamber, 5 consecutive experiments were performed with the tape mounted to the chamber without a hole for the END device. These tests revealed a consistent seal between the tape and the chamber. A typical measurement from one of these tests is shown in Figure 6.7.

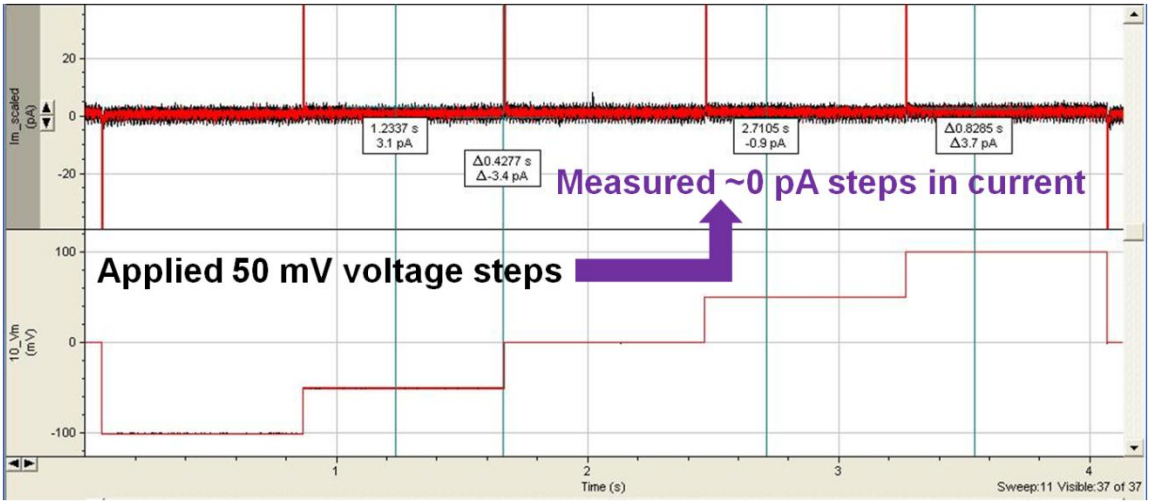

Figure 6.7 Voltage and currrent vs time data, indicating zero current measured after 37 sweeps of testing seal between tape and chamber (the top measurement is the current, and the bottom is applied voltage).

These tests were performed for 30 minute intervals with intermittent tapping of the chamber to assess the robustness of the seal with regard to disturbances. This was necessary because, during END conductance measurements, similar tapping of the chamber was performed to induce wetting of the pore or dissolve air bubbles.

The next set of experiments examined the integrity of the seal between the ENDs and the tape. The devices used did not have pores present. In initial experiments, a wide range of leaks was registered. It was found that the following factors impacted the quality of the seal: It was critical to cut the square hole into the tape with the scalpel without cutting too far in any single direction. Cuts which went even a half millimeter too far would cause leakage. Pushing the chip too hard against the tape would cause lacerations in the tape visible in the microscope and usually resulting in leakage. Finally, silicon grease needed to be applied generously and with a stroke towards the center of the device. This created the appearance of a "mountain-shaped" silicon seal which was heaviest in the contact regions and thinner at a millimeter or more away from the contact points. After implementing this method of mounting, ten consecutive 30-minute trials were performed with tapping in which no leaks were observed in the measurements.

6.5 Conductance Measurement of a Nanopore

After devising an effective mounting technique and ensuring proper seals a series of ENDs were tested in the chamber. In nearly all cases, zero current was measured through the ENDs initially. At that point the chamber would be tapped gently to dislodge air bubbles and promote wetting of the pore. In the first END, a 50 nm pore by SEM, this tapping yielded a current of 30 pA in response to 50 mV voltage steps. This is shown in Figure 6.8 below.

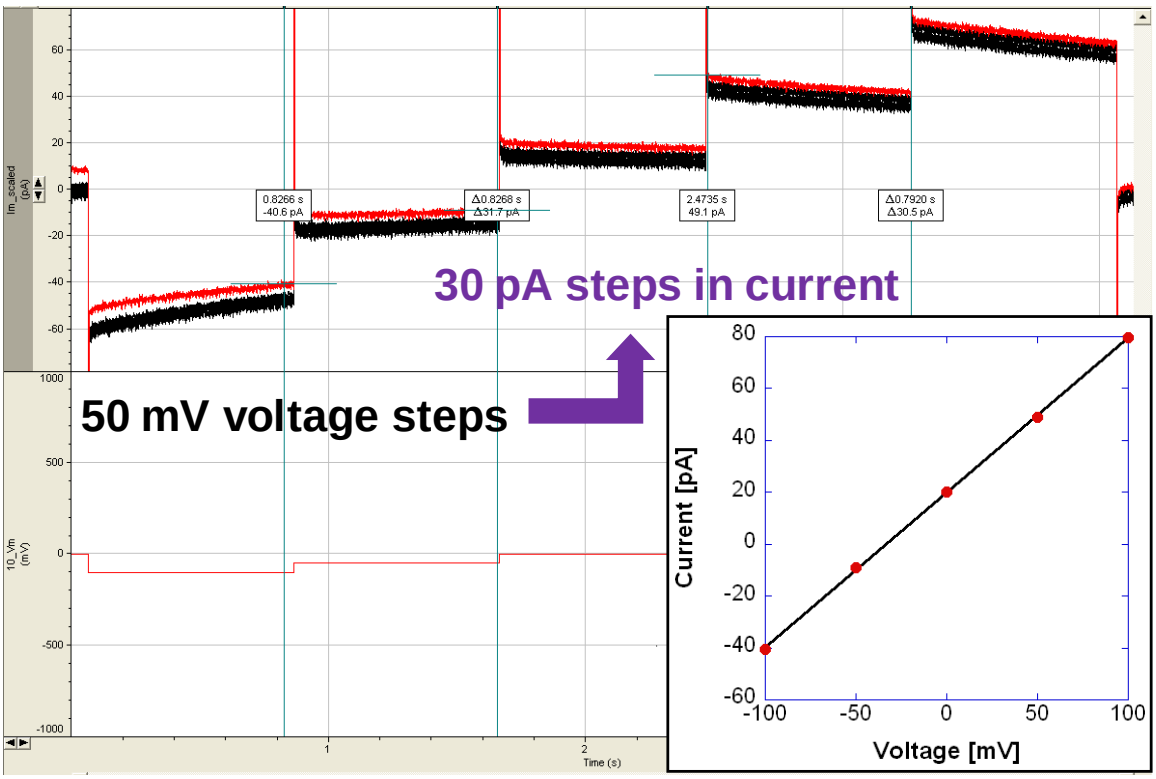

Figure 6.8. Voltage and currrent vs time data demonstrating 30 pA measured steps in current resulting from 50 mV steps in voltage. VI Curve inset.

From Figures 6.7 and 6.8, the noise levels of the apparatus were consistently at an amplitude of ± 2 pA compared to the 30 pA measurements. This is a sample error of ± 7%, which is comparable to demonstrations in the literature [24, 90, 91]. Further tapping caused the current to increase to 55 pA and then to 100 pA. This result is expected to be due to the genuine behavior of current measured through the pore (as opposed to a leak), especially because the devices demonstrated great resilience to the same degree of tapping during seal tests. The resistance of the system was calculated by equation 5.1: $R = V / I = 50 \text{ mV} / 100 \text{ pA} = 5 \times 10^8 \ \Omega$. Comparing this to the resistance of the chamber (order 100 Ω or lower) and the resistance of the trench (order 1000 Ω), it is clear that the transport of ions is controlled by the pore. Therefore, to calculate the effective pore

diameter, Equation 6.4 is used with $\rho = 80\ \Omega$ cm, $l = 50$ nm, and $R = 5 \times 10^8\ \Omega$. The result is compared to the conductance measurements of other researchers in Table 6.1.

*Table 6.1. Pore sizes reported by various groups [24, 90, 91] compared to their apparent diameters calculated from equation (6.4). *Li's group reported a pore length of between 5 and 10 nm which is the reason for the range shown here.*

	Meller (α-hL) [76]	Heng (Si_3N_4 by Ion Beam Sculpting) [24]		Li (Si_3N_4 by TEM Sputtering) [75]	Current Work (FIB)	(EBL)
Apparent Diameter (Conductance)	.59 nm	.86 nm	4.8 nm	2.7 < [nm] < 3.8*	1.5 μm	10 nm
Observed Diameter (SEM/TEM)	1.8 nm	1 nm	2.4 nm	3 nm	1.2 μm	50 nm

From Table 6.1, we can see that equation (6.4) is in reasonable agreement with pore size measured by traditional imaging techniques. In the case of Meller, it is important to recall that the hemolysin pore is far from cylindrical and therefore the apparent diameter represents a 'composite' diameter, which does not account for the complex internal geometry of the pore. Another important consideration of the conductance calculations is that the bulk resistivity of solution is used. At a small enough length scale this assumption will break down, but it appears to be reasonable even for pores down to 1 nm in size [24]. It is surely acceptable for a pore of order 10 nm. The calculated pore size for our pore at 100 pA is 10 nm, whereas the nominal pore size according to the SEM characterization was 50 nm. This suggests several possibilities. First, the mouth of the pore may in fact reduce to an opening of 10 nm. As indicated by the AFM data, the pores exhibit a narrowing behavior in the radial direction. This is

consistent with the fabrication methods used, and also brings us closer to the goal of sub-10 nm pore size. Unfortunately, we cannot rule out other possibilities. The hydrophobic nature of the pore wall may be an impediment to wetting and cause partial blockage of the pore. This would explain the apparent enlargement of the pore over the course of the measurement. Similarly, air bubbles could form which inhibit wetting of the surface. In both cases, it is possible that tapping of the chamber facilitates improved wetting of the pore and dislodgment of air bubbles. Another group has noted that they submersed their pores in IPA to aid in wetting the pore [90], suggesting that this issue is inherent to silicon nitride pores rather than the experimental apparatus.

Ultimately, it is suggested that the smallest constricting diameter of the pore is indeed about 10 nm, because the measured current did not advance beyond 100 pA even with continued tapping. It is very unlikely that the observed phenomenon was merely a leak, because a leak would be expected to yield continuously higher ionic current with the continued disturbance.

6.6 Conclusions and Recommendations

Detailed characterization of pore conductance will be necessary in future research that uses the ENDs fabricated by our process for biomoloecule analysis measurements. We made preliminary progress towards this goal, by successfully embedding a nanopore in a conductance chamber and measuring its conductivity. To better understand pore behavior in solution, it is suggested that further improvements be implemented in the design of the conductance apparatus. The ENDs could be connected directly to tubes with rubber seals and with a mechanism which can apply fine amounts of pressure between the two chambers. The latter will allow us to wet the pore without fracturing the membrane or applying external tapping. Despite the difficulties, the rigorous detail in the seal test experiments indicates that the current measured through the END was a physically

relevant phenomenon which gives us insight into the physical nature of the pore geometry and properties. The theory of a narrower pore mouth can be confirmed by AFM using a carbon nanotube tip or TEM. Hydrophobic effects within the pore can be curbed by ALD of an oxide.

CHAPTER 7

CONCLUSIONS AND RECOMMENDATIONS

A wafer scale process for fabricating large arrays of nanopores in the sub-20 nm range on a wafer has been developed, optimized, and characterized. The process employs a combination of electron beam lithography and atomic layer deposition, both of which are reasonably well characterized and used in industry. This is a necessary step towards scaling up nanopore devices for practical applications in biosensing. The fabrication process described here has been demonstrated to produce hundreds of devices on a wafer with high throughput, tunable pore size, and reproducibility. In a controlled fabrication environment, this process can be scaled up to produce thousands of nanopore devices on a single 12" wafer. Furthermore, the high precision of the ALD step allows continued pore shrinkage to the nanometer range.

Multiple fabrication methods were investigated and optimized to achieve the final process. An unmodified FIB was found to be insufficient in consistently producing high quality pores in the sub-100 nm range. EBL required optimizations of dose, resist thickness, and etching parameters. Electron backscattering was found to be dependent on the film thickness of silicon nitride, with thinner films resulting in larger features. LPCVD deposited silicon nitride was found to consistently yield a high throughput of ENDs. Film thicknesses of 50 nm down to 8.8 nm were achieved. Aspect ratios as high as 10,000 were demonstrated with 88% device survival rates following KOH etch. The thinnest film of good quality was deposited in two consecutive growth steps. Poor quality films of thickness greater than 10 nm were attributed to leaks in the chamber during growth or contamination, in both cases causing oxide contamination. Although films with good uniformity were achievable with PECVD, these films contained defects that caused

them to be etched away in KOH. The best measure of film quality was immersion in KOH, and ellipsometry provided insight into the film stoichiometry.

It was also found that film thickness could be reduced at the end of the process by etching in inductively coupled plasma without compromising the film. This would certainly be an avenue worth investigating to reduce the film thickness to the channel length required for some END applications (1-5 nm). Wet etches such as a very dilute buffered oxide etch may be an alternative as well.

The present process can also be easily modified for different applications. For example, several pores of different sizes can be patterned on a single device. This may be useful for detecting multiple analytes which vary in size or charge in a solution. If silicon dioxide is deposited instead of aluminum oxide, the pores can thereafter be functionalized for different single-molecule sensing applications [92, 93]. Atomic layer deposition of other materials such as titanium oxide [94]or metals [95-97] can also be used to give the nanopores different chemical, mechanical, and electrical properties for a desired application. Future END devices would benefit from integration of electrodes onto the wafer in early processing. Alternatively, the wafers produced by the methods here can be packaged by wafer bonding to contain the chambers and supply the electrodes.

Detailed simulations of the EBL process gave considerable insight into nanopore patterning and formation. The simulation results were found to be in generally good agreement with the experimental pore size in single and multiple shot cases. The pores were found to exhibit significant degrees of tapering which became more prominent at lower dose and blur. This is consistent with the SEM and AFM measurements. The methods described here can be extrapolated to any EBL process given the substrate composition, operating conditions, and etch ratio of resist to substrate. The simulation

parameters can be optimized by performing a limited number of experiments and comparing to SEM data. For rigorous determination of both feature size and internal geometry it is recommended that the point spread function include secondary electron behavior.

Conductance measurements of a nanopore were also performed, although the data collected was limited. In wafer scale parallel processing, it is recommended that the conductance chamber be closed to atmosphere via glass tubing and rubber seals. Pore wetting can be facilitated by finely controlled pressure gradients via flowmeter coupled with moderate levels of injected surfactant such as ethanol.

APPENDIX A

SCELETON X SIMULATIONS OF 100 NM ZEP ON 19 NM SI_3N4 ON SI

Figures A.1-A.6 below demonstrate the simulated pore geometry without secondary electrons at a blur of 5 nm, 9.9 nm, 15 nm, 20 nm, 25 nm, and 30 nm in 100 nm ZEP on 19 nm silicon nitride on silicon. The results are nearly identical to those reported in chapter 4 for 100 nm ZEP on silicon.

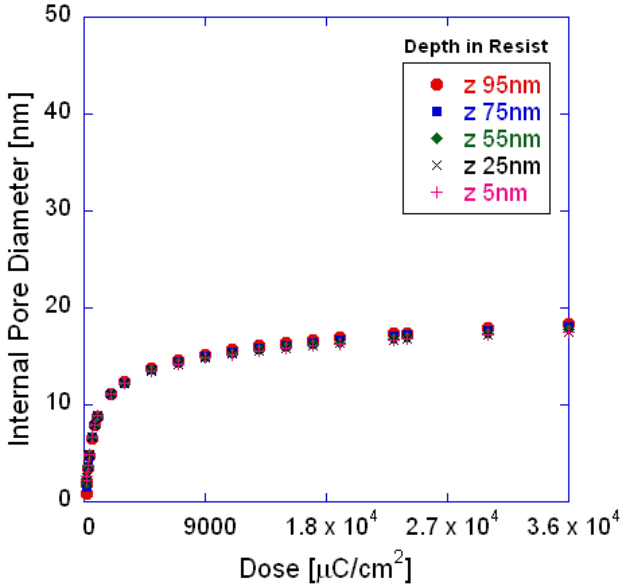

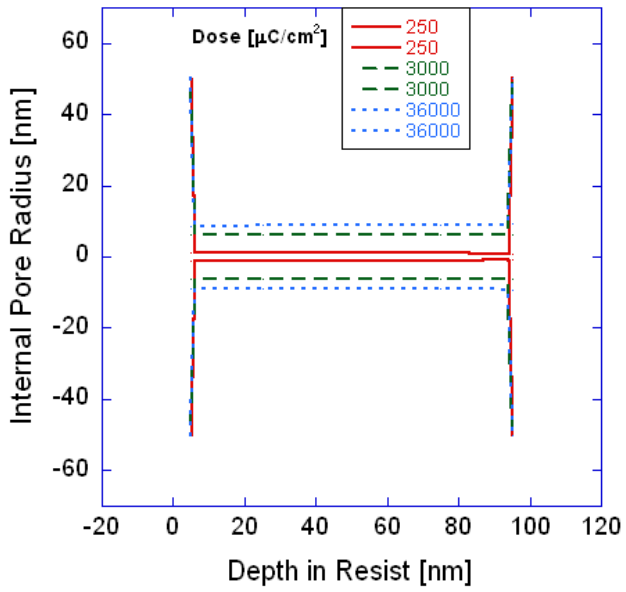

Figure A.1. Internal pore diameter of single shot pores at different doses in 100nm ZEP on 19 nm silicon nitride on Si assuming a beam blur of 5 nm and no secondary electron emission.

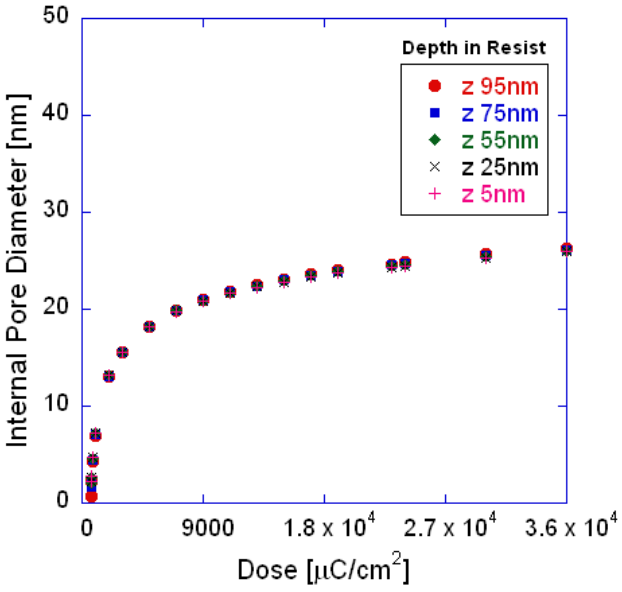

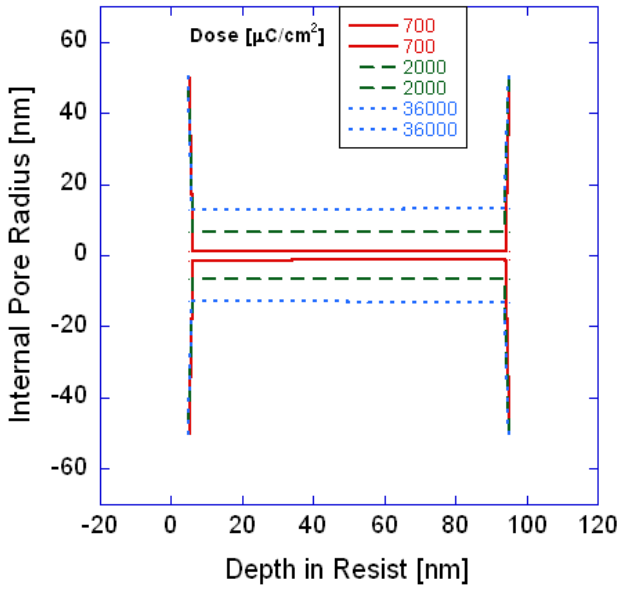

Figure A.2. Internal pore diameter of single shot pores at different doses in 100nm ZEP on 19 nm silicon nitride on Si assuming a beam blur of 9.9 nm and no secondary electron emission.

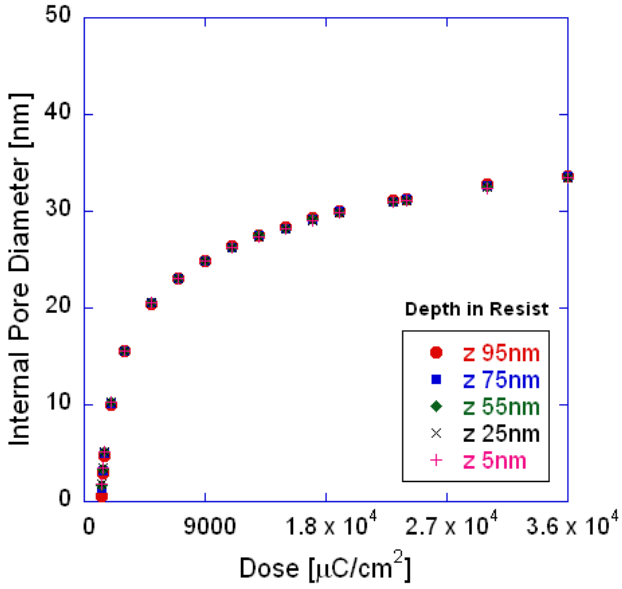

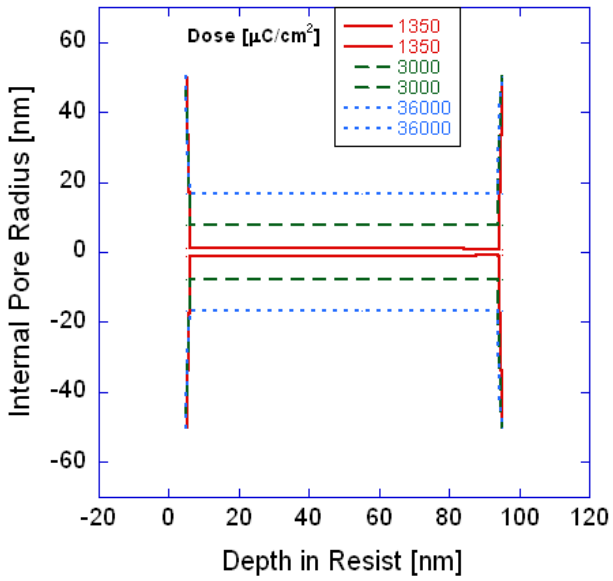

Figure A.3. Internal pore diameter of single shot pores at different doses in 100nm ZEP on 19 nm silicon nitride on Si assuming a beam blur of 15 nm and no secondary electron emission.

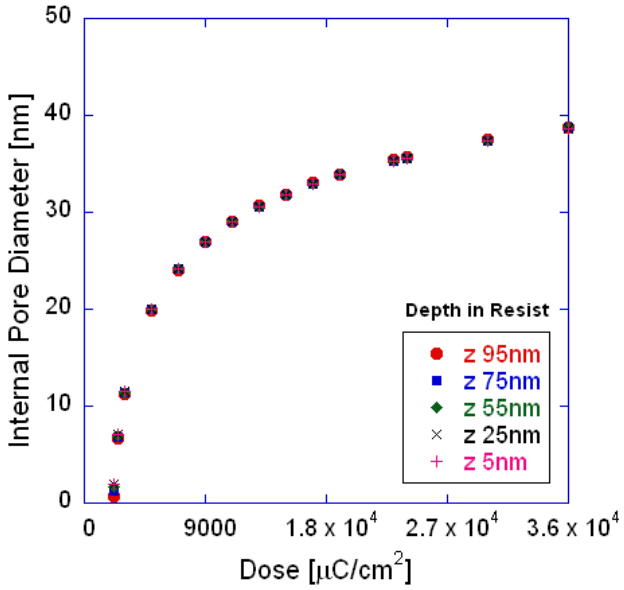

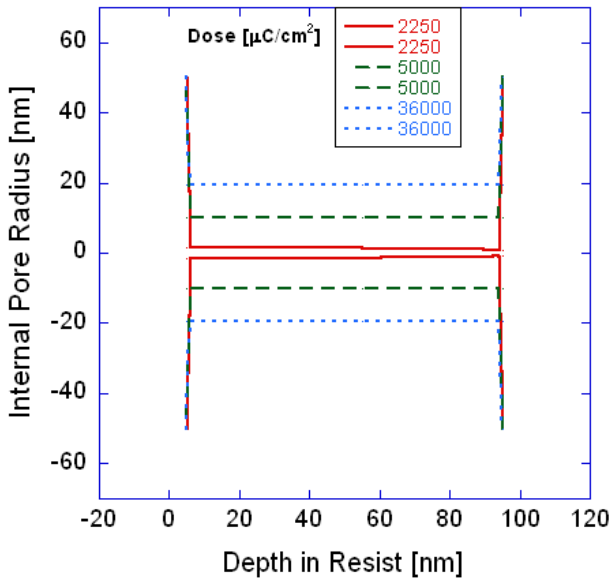

Figure A.4. Internal pore diameter of single shot pores at different doses in 100nm ZEP on 19 nm silicon nitride on Si assuming a beam blur of 20 nm and no secondary electron emission.

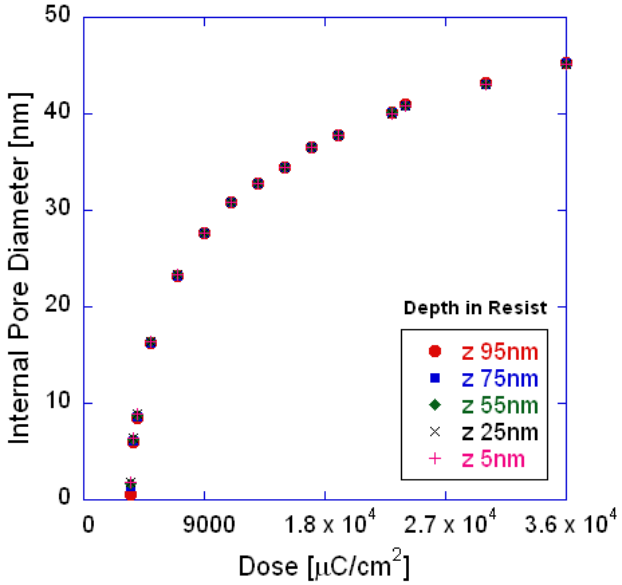

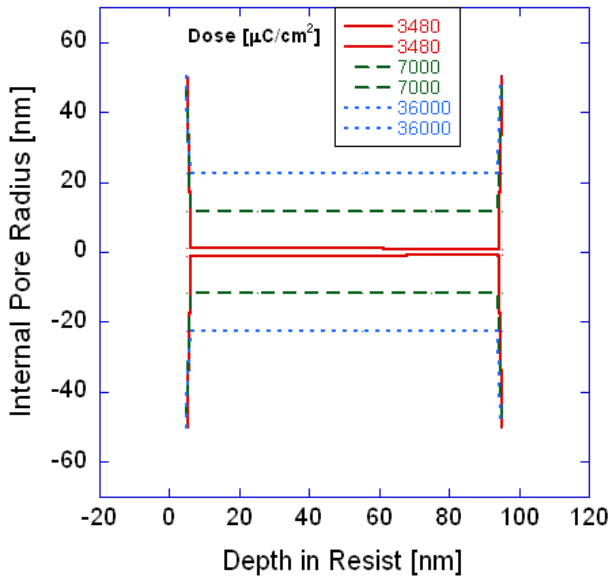

Figure A.5. Internal pore diameter of single shot pores at different doses in 100nm ZEP on 19 nm silicon nitride on Si assuming a beam blur of 25 nm and no secondary electron emission.

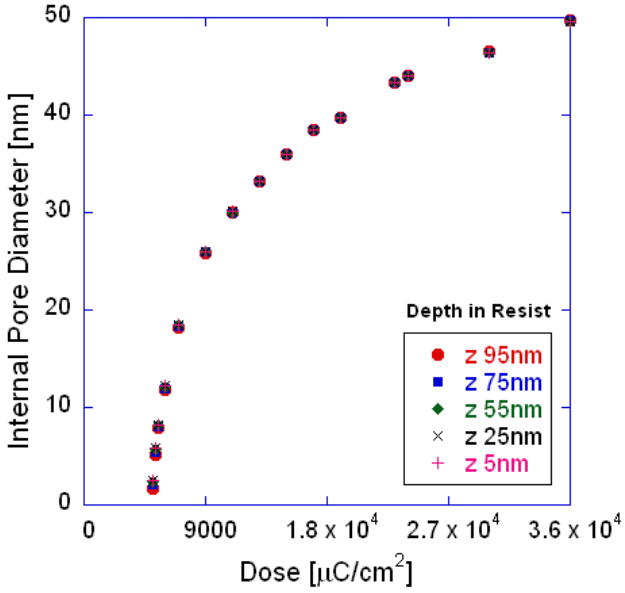

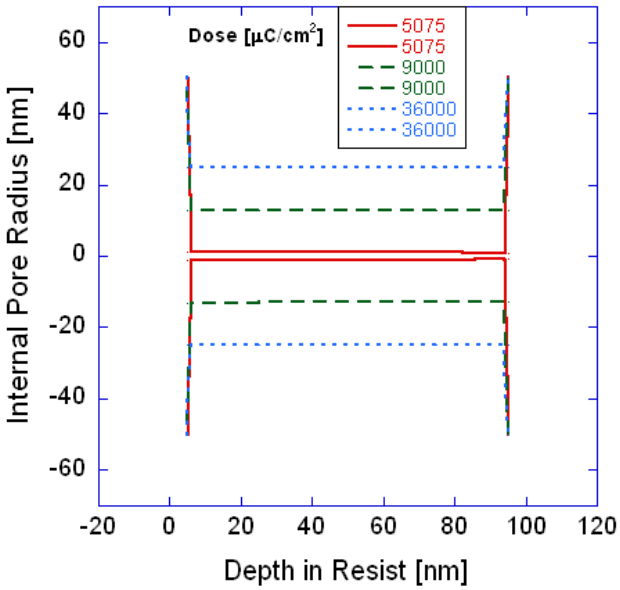

Figure A.6. Internal pore diameter of single shot pores at different doses in 100nm ZEP on 19 nm silicon nitride on Si assuming a beam blur of 30 nm and no secondary electron emission.

REFERENCES

1. Aidley, D.J. and P.R. Stanfield, *Ion Channels: Molecules in Action* 1996: Cambridge University Press.

2. Davis, M.E., *Ordered porous materials for emerging applications.* Nature, 2002. **417**(6891): p. 813-821.

3. Baughman, R.H., A.A. Zakhidov, and W.A. de Heer, *Carbon nanotubes - the route toward applications.* Science, 2002. **297**(5582): p. 787-792.

4. Goldberger, J., R. Fan, and P.D. Yang, *Inorganic nanotubes: A novel platform for nanofluidics.* Accounts Of Chemical Research, 2006. **39**(4): p. 239-248.

5. Kasianowicz, J.J., *Nanometer, scale pores: Potential applications for analyte detection and DNA characterization.* Disease Markers, 2002. **18**(4): p. 185-191.

6. Collins, F.S., et al., *A vision for the future of genomics research.* Nature, 2003. **422**(6934): p. 835-847.

7. Deamer, D.W. and M. Akeson, *Nanopores and nucleic acids: prospects for ultrarapid sequencing.* Trends In Biotechnology, 2000. **18**(4): p. 147-151.

8. Braha, O., et al., *Designed protein pores as components for biosensors.* Chemistry & Biology, 1997. **4**(7): p. 497-505.

9. Guan, X.Y., et al., *Stochastic sensing of TNT with a genetically engineered pore.* Chembiochem, 2005. **6**(10): p. 1875-1881.

10. Butler, T.Z., J.H. Gundlach, and M. Troll, *Translocation of RNA block-copolymers through the alpha hemolysin nanopore.* Biophysical Journal, 2005. **88**(1): p. 347A-347A.

11. Butler, T.Z., J.H. Gundlach, and M.A. Troll, *Determination of RNA orientation during translocation through a biological nanopore.* Biophysical Journal, 2006. **90**(1): p. 190-199.

12. Akeson, M., et al., *Microsecond time-scale discrimination among polycytidylic acid, polyadenylic acid, and polyuridylic acid as homopolymers or as segments within single RNA molecules.* Biophysical Journal, 1999. **77**(6): p. 3227-3233.

13. Meller, A., et al., *Rapid nanopore discrimination between single polynucleotide molecules.* Proceedings Of The National Academy Of Sciences Of The United States Of America, 2000. **97**(3): p. 1079-1084.

14. Vercoutere, W., et al., *Rapid discrimination among individual DNA hairpin molecules at single-nucleotide resolution using an ion channel.* Nature Biotechnology, 2001. **19**(3): p. 248-252.

15. Vercoutere, W.A., et al., *Analysis of hairpin structures within single DNA molecules using a nanopore detector.* Biophysical Journal, 2000. **78**(1): p. 402A-402A.

16. Marziali, A. and M. Akeson, *New DNA sequencing methods.* Annual Review of Biomedical Engineering, 2001. **3**: p. 195-223.

17. Vercoutere, W. and M. Akeson, *Biosensors for DNA sequence detection.* Current Opinion In Chemical Biology, 2002. **6**(6): p. 816-822.

18. Kong, C.Y. and M. Muthukumar, *Modeling of polynucleotide translocation through protein pores and nanotubes.* Electrophoresis, 2002. **23**(16): p. 2697-2703.

19. Li, J., et al., *Ion-beam sculpting at nanometre length scales.* Nature, 2001. **412**(6843): p. 166-169.

20. Li, J.L., et al., *DNA molecules and configurations in a solid-state nanopore microscope.* Nature Materials, 2003. **2**(9): p. 611-615.

21. Krapf, D., et al., *Fabrication and characterization of nanopore-based electrodes with radii down to 2 nm.* Nano Letters, 2006. **6**(1): p. 105-109.

22. Heng, J.B., et al., *Stretching DNA using an artificial nanopore.* Biophysical Journal, 2005. **88**(1): p. 659A-659A.

23. Heng, J.B., et al., *Beyond the gene chip.* Bell Labs Technical Journal, 2005. **10**(3): p. 5-22.

24. Heng, J.B., et al., *Sizing DNA Using a Nanometer-Diameter Pore.* Biophysical Journal, 2004. **87**(4): p. 2905-2911.

25. Keyser, U.F., et al., *Direct force measurements on DNA in a solid-state nanopore.* Nature Physics, 2006. **2**(7): p. 473-477.

26. Mara, A. and Z. Siwy, *An asymetric nanopore for biomolecular sensing.* Biophysical Journal, 2004. **86**(1): p. 603A-603A.

27. Yan, H. and B.Q. Xu, *Towards rapid DNA sequencing: Detecting single-stranded DNA with a solid-state nanopore.* Small, 2006. **2**(3): p. 310-312.

28. Kyser, D.F. and N.S. Viswanathan, *Monte Carlo simulation of spatially distributed beams in electron-beam lithography.* Journal of Vacuum Science and Technology, 1975. **12**(6): p. 1305-1308.

29. Parikh, M. and D. Kyser, *Energy deposition functions in electron resist films on substrates.* Journal of Applied Physics, 1979. **50**(2): p. 1104-11.

30. Halverson, K.M., et al., *Anthrax biosensor, protective antigen ion channel asymmetric blockade.* Journal Of Biological Chemistry, 2005. **280**(40): p. 34056-34062.

31. Bayley, H. and P.S. Cremer, *Stochastic sensors inspired by biology.* Nature, 2001. **413**(6852): p. 226-230.

32. Kasianowicz, J.J., *Nanopores - Flossing with DNA.* Nature Materials, 2004. **3**(6): p. 355-356.

33. Nilsson, J., et al., *Localized functionalization of single nanopores.* Advanced Materials, 2006. **18**(4): p. 427-+.

34. Han, A.P., et al., *Sensing protein molecules using nanofabricated poresn.* Applied Physics Letters, 2006. **88**(9).

35. Harrell, C.C., Z.S. Siwy, and C.R. Martin, *Conical nanopore membranes: Controlling the nanopore shape.* Small, 2006. **2**(2): p. 194-198.

36. Harrison, O., et al., *Probing single polypeptides with a solid state nanopore sensor.* Biophysical Journal, 2004. **86**(1): p. 480A-480A.

37. Lagerqvist, J., M. Zwolak, and M. Di Ventra, *Fast DNA sequencing via transverse electronic transport.* Nano Letters, 2006. **6**(4): p. 779-782.

38. Chan, E.Y., *Advances in sequencing technology.* Mutation Research-Fundamental And Molecular Mechanisms Of Mutagenesis, 2005. **573**(1-2): p. 13-40.

39. Bhattacharya, S., S. Nair, and A. Chatterjee, *An Accurate DNA Sensing and Diagnosis Methodology Using Fabricated Silicon Nanopores.* IEEE Transactions on Circuits & Systems - I : Special Issue on Advances in Life Science Systems (in press), 2006.

40. Bhattacharya, S., et al., *Efficient DNA sensing with fabricated silicon nanopores: diagnosis methodology and algorithms.* Proceedings of the 19th International Conference on VLSI Design, 2006.

41. Li, J.L., et al., *Solid state nanopore as a single DNA molecule detector.* Biophysical Journal, 2003. **84**(2): p. 134A-135A.

42. Chen, L.M., et al., *Fast fabrication of large-area nanopore arrays by FIB.* Acta Physica Sinica, 2005. **54**(2): p. 582-586.

43. Rhee, H., et al., *Comparison of deep silicon etching using SF6/C4F8 and SF6/C4F6 plasmas in the Bosch process*. Vol. 26. 2008: AVS. 576-581.

44. Bhatnagar, Y.K. and A. Nathan, *On pyramidal protrusions in anisotropic etching of <100 > silicon.* Sensors and Actuators A: Physical, 1993. **36**(3): p. 233-240.

45. Choi, W., et al., *Effect of etchant concentration and defects on pyramid formation in TMAH etched silicon.* Bulletin of Materials Science, 1999. **22**(3): p. 615-621.

46. Papet, P., et al., *Pyramidal texturing of silicon solar cell with TMAH chemical anisotropic etching.* Solar Energy Materials and Solar Cells, 2006. **90**(15): p. 2319-2328.

47. Choi, W.K., et al., *Formation of pyramids at surface of TMAH etched silicon.* Applied Surface Science, 1999. **144-145**: p. 472-475.

48. Yan, Z., et al. *Study on diameter of nanopore with focus ion beam*. in *Biomedical Engineering and Informatics (BMEI), 2010 3rd International Conference on*. 2010.

49. Namatsu, H., et al., *10-nm silicon lines fabricated in (110) silicon.* Microelectronic Engineering, 1995. **27**(1-4): p. 71-74.

50. Geschke, O., H. Klank, and P. Telleman, *Microsystem engineering of lab-on-a-chip devices*. 2008: Wiley-VCH.

51. Pelletier, J. and M.J. Cooke, *Anisotropy control in CF4 microwave plasma etching*. Vol. 65. 1989: AIP. 464-467.

52. Rai-Choudhury, P., *Handbook of Microlithography, Micromachining, and Microfabrication: Microlithography*. 1997: SPIE Optical Engineering Press.

53. Chang, T.H.P., *Proximity effect in electron-beam lithography.* Journal of Vacuum Science and Technology, 1975. **12**(6): p. 1271-1275.

54. Umbach, C.P. and A.N. Broers. *Experimental determination of the proximity effect from 25 to 100 keV in electron beam patterned x-ray masks*. 1990: AVS.

55. Nishida, T., et al., *Quantum Wire Fabrication by E-Beam Elithography Using High-Resolution and High-Sensitivity E-Beam Resist ZEP-520.* Japanese Journal of Applied Physics. **31**(Copyright (C) 1992 Publication Board, Japanese Journal of Applied Physics): p. 4508.

56. Wang, H., et al., *Low temperature ZEP-520A development process for enhanced critical dimension realization in reactive ion etch etched polysilicon.* Journal of Vacuum Science and Technology B: Microelectronics and Nanometer Structures, 2007. **25**(1): p. 102-105.

57. Mohammad, M.A., et al., *Study of development processes for ZEP-520 as a high-resolution positive and negative tone electron beam lithography resist.* Japanese Journal of Applied Physics, 2012. **51**(6 PART 2).

58. Salvat, F., et al., *PENELOPE 2001 - A Code System for Monte Carlo Simulation of Electron and Photon Transport*. 2002, Nuclear Energy Agency: Issy-les-Moulineaux. p. 250.

59. Pasciak, A.S. and J.R. Ford, *An accurate approximation for the highly efficient sampling of polar scattering angle of electron elastic single-scattering events.* Scanning, 2006. **28**(6): p. 333-41.

60. Bishop, H.E., *Electron scattering in thick targets.* British Journal of Applied Physics, 1967. **18**(6): p. 703-715.

61. Koshelev, K., et al., *Comparison between ZEP and PMMA resists for nanoscale electron beam lithography experimentally and by numerical modeling.* Journal of Vacuum Science and Technology B: Microelectronics and Nanometer Structures, 2011. **29**(6).

62. Raptis, I., et al. *Electron beam lithography simulation for high resolution and high-density patterns*. in *Sixth International Conference on Electron Beam Technologies (EBT '2000), 4-7 June 2000*. 2001. UK: Elsevier.

63. Le denmat, J.C., et al. *Electron beam lithography simulation based on a single convolution approach: application for sub-45 nm nodes*. in *23rd European Mask and Lithography Conference, 22 Jan. 2007*. 2007. USA: SPIE - The International Society for Optical Engineering.

64. Ivin, V.V., et al. *Efficient and robust algorithms for Monte Carlo and e-beam lithography simulation*. in *26th International Conference on Micro- and Nano-Engineering, 18-21 Sept. 2000*. 2001. Netherlands: Elsevier.

65. Li, L., et al., *Modeling and simulation development of electron beam resist based on cellular automata.* Microelectronics Journal, 2006. **37**(4): p. 317-20.

66. Kim, S.H., et al. *New approach of Monte Carlo simulation for low energy electron beam lithography*. in *Micro- and Nano- Engineering 97. MNE International Conference on Micro- and Nanofabrication, 15-18 Sept. 1997*. 1998. Netherlands: Elsevier.

67. Keil, K., et al. *Resolution and total blur: Correlation and focus dependencies in e-beam lithography*. 2009. 120 Wall Street, 32nd Floor, New York, NY 10005-3993, United States: AVS Science and Technology Society.

68. Slodowski, M., et al. *Coulomb blur advantage of a multi shaped beam lithography approach*. in *Alternative Lithographic Technologies, February 24, 2009 - February 26, 2009*. 2009. San Jose, CA, United states: SPIE.

69. Yu, M.L., A. Sagle, and B. Buller. *Exploring the fundamental limit of CD control: A measurement of shot noise induced CDU in e-beam lithography*. in *EMLC 2005: 21st European Mask and Lithography Conference, January 31, 2005 - Febrary 3, 2005*. 2005. Dresden, Germany: SPIE.

70. Pan, Z.-Y., et al. *Influence of shot noise on CDU with DUV, EUV, and e-beam*. in *Optical Microlithography XXI, Febrary 26, 2008 - Febrary 29, 2008*. 2008. San Jose, CA, United states: SPIE.

71. Yoshizawa, M. and S. Moriya. *Edge roughness evaluation method for quantifying at-size beam blur in electron beam lithography*. in *Emerging Lithographic Technologies IV, Febrary 28, 2000 - March 1, 2000*. 2000. Santa Clara, CA, USA: Society of Photo-Optical Instrumentation Engineers.

72. Van Steenwinckel, D., et al., *Novel method for characterizing resist performance.* Journal of Microlithography, Microfabrication, and Microsystems, 2008. **7**(2): p. 023002 (10 pp.).

73. Shokouhi, B., Z. Jian, and C. Bo, *Very high sensitivity ZEP resist using MEK:MIBK developer.* Micro & Nano Letters, 2011. **6**(12): p. 992-4.

74. Brown, D. (2010) *Comparison of Resist Thickness to Sensitivity*. 1-7.

75. Grant, D.J. and S. Sivoththaman, *Electron-Beam Lithography: From Past to Present.* 2003.

76. Ong, P.L. and et al., *A new fabrication method for low stress PECVD - SiN x layers.* Journal of Physics: Conference Series, 2006. **34**(1): p. 764.

77. Panepucci, R.R., et al., *Silicon nitride deposited by electron cyclotron resonance plasma-enhanced chemical vapor deposititon for micromachining applications*. Vol. 3512. 1998: SPIE. 146-151.

78. Jellison, J.G.E., et al., *Spectroscopic ellipsometry characterization of thin-film silicon nitride.* Thin Solid Films, 1998. **313–314**(0): p. 193-197.

79. D.E, A., *Optical properties of thin films.* Thin Solid Films, 1982. **89**(3): p. 249-262.

80. Dehan, E., et al., *Optical and structural properties of SiOx and SiNx materials.* Thin Solid Films, 1995. **266**(1): p. 14-19.

81. Medernach, J.W. and R.C. Martin, *The optical properties and stoichiometry of evaporated bismuth oxide thin films.* Journal of Vacuum Science and Technology, 1975. **12**(1): p. 63-66.

82. Vamvakas, V.E., N. Vourdas, and S. Gardelis, *Optical characterization of Si-rich silicon nitride films prepared by low pressure chemical vapor deposition.* Microelectronics Reliability, 2007. **47**(4–5): p. 794-797.

83. Gardeniers, J.G.E., H.A.C. Tilmans, and C.C.G. Visser, *LPCVD silicon-rich silicon nitride films for applications in micromechanics, studied with statistical experimental design[sup]*.* Journal of Vacuum Science & Technology A: Vacuum, Surfaces, and Films, 1996. **14**(5): p. 2879-2892.

84. Madou, M.J., *Fundamentals of microfabrication: the science of miniaturization*. 2002: CRC Press.

85. Peev, G., L. Zambov, and Y. Yanakiev, *Kinetics of the chemical reaction between dichlorosilane and ammonia during silicon nitride film deposition.* Thin Solid Films, 1990. **189**(2): p. 275-282.

86. Hines, A.L. and R.N. Maddox, *Mass transfer: fundamentals and applications*. 1985: Prentice-Hall.

87. Yun, S.J., et al. *Characterization of Al2O3 films grown by atomic layer deposition using Al(CH3)3 and H2O*. 1997. San Francisco, CA, USA: MRS.

88. Jakschik, S., et al., *Physical characterization of thin ALD-Al2O3 films.* Applied Surface Science, 2003. **211**(1-4): p. 352-359.

89. Chen, P., et al., *Atomic layer deposition to fine-tune the surface properties and diameters of fabricated nanopores.* Nano Letters, 2004. **4**(7): p. 1333-1337.

90. Li, J., et al., *DNA molecules and configurations in a solid-state nanopore microscope.* Nat Mater, 2003. **2**(9): p. 611-615.

91. Meller, A., L. Nivon, and D. Branton, *Voltage-Driven DNA Translocations through a Nanopore.* Physical Review Letters, 2001. **86**(15): p. 3435-3438.

92. Lund, J., R. Mehta, and B.A. Parviz, *Label-free direct electronic detection of biomolecules with amorphous silicon nanostructures.* Nanomedicine: Nanotechnology, Biology and Medicine, 2006. **2**(4): p. 230-238.

93. Tan, J., H.-F. Wang, and X.-P. Yan, *Discrimination of Saccharides with a Fluorescent Molecular Imprinting Sensor Array Based on Phenylboronic Acid Functionalized Mesoporous Silica.* Analytical Chemistry, 2009. **81**(13): p. 5273-5280.

94. Jogi, I., et al., *Conformity and structure of titanium oxide films grown by atomic layer deposition on silicon substrates.* Thin Solid Films, 2008. **516**(15): p. 4855-62.

95. Zhengwen, L., A. Rahtu, and R.G. Gordon, *Atomic layer deposition of ultrathin copper metal films from a liquid Copper(I) amidinate precursor.* Journal of the Electrochemical Society, 2006. **153**(11): p. 787-94.

96. Kim, H., *The application of atomic layer deposition for metallization of 65 nm and beyond.* Surface & Coatings Technology, 2006. **200**(10): p. 3104-11.

97. Eyck, G.A.T., et al., *Plasma-assisted atomic layer deposition of palladium.* Chemical Vapor Deposition, 2005. **11**(1): p. 60-66.